Principles of Quantum Dot Photophysics and Applications to Luminescent Downshifting

by

Jennifer Marie Scherer

B.S. Chemistry, 2009
The Ohio State University

MASSACHUSETTS INSTITUTE OF TECHNOLOGY
JUN 23 2016
LIBRARIES
ARCHIVES

Submitted to the Department of Chemistry
in Partial Fulfillment of the Requirements for the Degree of

DOCTOR OF PHILOSOPHY IN PHYSICAL CHEMISTRY

at the

MASSACHUSETTS INSTITUTE OF TECHNOLOGY

June 2016

© 2016 Massachusetts Institute of Technology.
All rights reserved

Author..... Signature redacted
Department of Chemistry
May 6, 2016

Certified by..... Signature redacted
Moungi G. Bawendi
Lester Wolfe Professor of Chemistry
Thesis Supervisor

Accepted by..... Signature redacted
Robert W. Field
Haslam and Dewey Professor of Chemistry
Chairman, Departmental Committee on Graduate Students

This doctoral thesis has been examined by a Committee of the Department of Chemistry as follows:

Signature redacted

Professor Keith A. Nelson.....
Haslam and Dewey Professor of Chemistry
Chairperson

Signature redacted

Professor Moungi G. Bawendi.....
Lester Wolfe Professor of Chemistry
Thesis Supervisor

Signature redacted

Professor Jianshu Cao.....
Thesis Committee Member

Principles of Quantum Dot Photophysics and Applications to Luminescent Downshifting

by

Jennifer Marie Scherer

Submitted to the Department of Chemistry
on May 6, 2016, in partial fulfillment of the
requirements for the degree of
Doctor of Philosophy

Abstract

Colloidal quantum dots (QDs) exhibit remarkable size-tunable optical properties including broad absorbance and bright, narrow emission. This thesis presents efforts to utilize, manipulate, and expand these properties. Despite the wide range of applications that benefit from multiband spectral information, traditional p-n junction photodetectors suffer from a fundamentally limited range of sensitivity due to a trade-off between light absorption and charge extraction. In order to expand the utility of a photodetector, its region of sensitivity can be enhanced via spectrum shifting. Here the optical properties of QDs are utilized to shift high energy photons to lower energy photons that lie within the detector's sensitive region through a process called luminescent downshifting. Chapters 2-5 will explore the application of luminescent downshifting from the near-ultraviolet to the short-wavelength infrared, the far-ultraviolet to the visible, and the ultraviolet to the mid-wavelength infrared. Unique challenges are addressed for each wavelength region to achieve increases of 10-55% absolute in the external quantum efficiency. The technology has been translated from single-element detectors to imaging arrays which is demonstrated in various environments. In pursuit of a deeper understanding of the surface-related effects on the photophysical properties of infrared quantum dots, the feasibility of shell growth and the effect of stoichiometric modification of lead chalcogenide quantum dots are presented in Appendix A. The resulting impact on emission wavelength, quantum yield, photoluminescent lifetime, and carrier mobility are explored.

Thesis Supervisor: Moungi G. Bawendi
Title: Lester Wolfe Professor of Chemistry

Acknowledgements

The past few years have been an amazing opportunity for me to grow as a scientist and as a person, and I am incredibly grateful for the many amazing friends and mentors who have supported me throughout my PhD studies. An essential part of this support network was the Bawendi lab. I am so thankful to have been able to work with the members of this group and to have grown under Moungi's advice and guidance. Moungi has the incredible ability to simultaneously promote independent exploration while still remaining available for discussions and guidance. For me, this environment has been crucial for developing both confidence as a scientist as well as increased comfort with new challenges.

In addition to being a wonderful advisor, Moungi has fostered a lab environment full of kind, hardworking, curious, and enthusiastic people. I entered the lab with Dan Harris, Jose Cordero, He Wei, Russ Jensen and Q1 Hwang, and it has been a wonderful experience to develop as a scientist alongside them. I fondly recall the time the six of us spent crammed into the sardine-can-sized first-year office. The device subgroup, including Darcy Grinolds, Whitney Hess, Scott Geyer, Q1 Hwang, Chia-Hao Chuang, and Liang-Yi Chang, has been a source of stimulating discussions, ideas synthesis, support, and glovebox company. Making and testing devices certainly would not have been as fun without their companionship. I was also fortunate to have many amazing mentors in the group, including Scott Geyer, Dave Strasfeld, Lisa Marshall and Zoran Popovic. In addition to patiently imparting some of their wisdom and knowledge upon me, all of these people exhibited a graceful and calm determination with perpetual kindness.

The Bawendi lab has facilitated the development of many lasting friendships. Whether it was spending time at the Muddy, running stadiums, having random discussions in the kitchen, or blaring music while testing devices, I truly value the time I have been able to spend with this group. Of particular note is Darcy Grinolds. Regardless of my mood, it was absolutely impossible to leave our conversations without a smile. Liberal with hugs, Darcy has been a tremendous friend and source of support. Raoul Correa and Jian Cui have been important support figures as well, always willing to discuss science or to drag me out of the lab to explore Boston. It has always been a pleasure to see the happy faces of Whitney Hess and Jessica Carr in lab, and I am going to miss our yoga classes together. There have been many others in lab who have been a constant source of laughs, pep talks, and advice, and I hope you all know how much you are appreciated.

Outside of the Bawendi lab, I am extremely thankful for the friends I've made in Boston. It is remarkable that one could encounter so many hilarious, amazing, generous, thoughtful, and caring people. Game nights, dinner table conversations, nights out, barbeques, and occasional travels across the US with

these folks have been defining moments of the past several years. Steph Teo, Ben Ofori-Okai, Kara Manke, Harold Hwang, Patrick Wen, Sharmini Radakrishnan, Kit Werley, Dylan Arias, Elizabeth Lemon, Colby Steiner, Prasahnt Sivarajah, Gill Teo, Eric Johlin, Patrick Brown, Joel Jean, you are all incredible people, and I am fortunate to have you all in my life.

I have my dear friend Jessica Flynn to thank, as well. Although we have been miles and miles apart since college, we are somehow perpetually on the same wavelength. Maybe the separated-at-birth theory is right after all. The challenges of life and graduate school would have seemed far more substantial without the best cheerleader a girl could hope for, and I am incredibly grateful for our friendship.

Harold Hwang has been a constant pillar of support throughout this time, as well. Through the most stressful of times, Harold has always attempted to impart a calmer view of life. One of these days it will actually rub off on me. Truly generous at heart and generous with laughs, I am extremely fortunate to call him a friend.

I would also like to thank the numerous teachers who have patiently and relentlessly worked to provide me with this education. Of particular importance to me were the efforts of Mrs. Carolyn Bast and Mr. Aaron Weltlin, my grade school science teachers. They truly inspired and cultivated my passion for science and learning. In college Dr. Patrick Woodward and Dr. Chris Callam generously allowed me to perform research in their labs, which were transformative experiences that led me to graduate school.

A number of MIT staff members have provided immense support. The lab simply would not function without the work of Li Miao, who magically fixes any of the administrative problems we get ourselves into. The chemistry education office has always been a wonderful resource, as well. Of particular note are Susan Brighton, Mary Turner, and Jennifer Weisman who have been extremely caring and generous with their time.

MIT has afforded me the opportunity to work with a wide range of wonderful collaborators. These include but are not limited to Anu Agarwal, Pao Tai Lin, Jianwei Mu, Dan Congreve, Nick Thompson, Phil Reusswig, Neil Patel, Veda Bharath, Frank Jaworski, Michael Jack, Nirat Ray, and Eric Johlin. I am very fortunate to have been able to work so closely with so many amazing minds.

Finally and most importantly, I have my family to thank. My brothers, Kevin and Michael, have been constant drivers for growth and sources of support. My grandpa, Robert Scherer, stressed the importance of education through words and by example. Most of all, my parents, Robbin and Kathy Scherer, raised my brothers and me with endless amounts love and fostered an environment where curiosity could blossom.

Jennifer Marie Scherer
May 6, 2016

For Mom and Dad

Contents

1 Introduction to Colloidal Quantum Dots 19

1.1 Introduction to QDs. 19

1.2 Synthetic fundamentals 23

1.3 The importance of surfaces 24

1.4 Device applications of QDs 26

1.5 References 27

2 Introduction to Luminescent Downshifting and Methods of Characterization 31

2.1 Introduction 31

2.2 Fundamental limitations of photodetectors 32

2.3 Luminescent downshifting 34

2.4 Downconversion versus downshifting. 34

2.5 Requirements of an efficient LDS material and modeling considerations . 36

2.6 Comparison of downshifting materials: Dyes vs QDs 38

2.7 The challenge of parasitic energy transfer 40

2.8 Relationship between QD lifetime and detector bandwidth 42

2.9 Measurement methods 44

2.9.1 Quantum yield 45

2.9.2 External quantum efficiency. 48

2.9.3 Photoluminescent lifetime. 50

2.10 Chapter-specific acknowledgments 51

2.11 References. 51

3 Near-UV-to-SWIR Broadband Detection and Imaging via Luminescent Downshifting 55

3.1 Introduction 55

3.1.1 Applications of near-UV-to-SWIR detection 56

3.1.2 Remote sensing 56

3.1.3 Chemical and biomedical analysis. 57

3.1.4 Multifunctionality 57

3.2 Results and discussion 58

3.2.1 Film design 59

3.2.1.1 Material choice . . . 59
3.2.1.2 FRET prevention . . . 60
3.2.2 External quantum efficiency measurements . . . 64
3.2.2.1 Room temperature performance . . . 64
3.2.2.2 Low temperature performance . . . 66
3.2.3 Filter design for isolated UV sensitivity of LDS detector . . . 69
3.2.4 Imaging demonstration . . . 71
3.2.5 Bandwidth determination . . . 75
3.3 Conclusions and future scope . . . 77
3.4 Experimental details . . . 78
3.4.1 PbS synthesis . . . 78
3.4.2 Cation exchange shell growth . . . 79
3.4.3 Film deposition . . . 79
3.4.4 Materials characterization . . . 80
3.5 Chapter-specific acknowledgements . . . 80
3.6 References . . . 80

4 Far- and Mid-UV Detector Sensitization for UV and Broadband Detection and Imaging via Luminescent Downshifting **85**
4.1 Introduction . . . 85
4.1.1 Definitions of UV spectral regions . . . 86
4.1.2 Applications of UV and UV-visible detectors . . . 87
4.1.2.1 Forensics and biomedical imaging . . . 87
4.1.2.2 Cosmic spectroscopy . . . 88
4.1.2.3 Defense and military applications . . . 88
4.1.3 Current UV technologies and limitations . . . 89
4.1.4 Previous approaches to visible downshifting . . . 90
4.2 Results and discussion . . . 92
4.2.1 Choice of downshifting material . . . 92
4.2.2 Considerations of ligand absorption in UV . . . 93
4.2.3 Minimization of FRET-induced quantum yield reduction . . . 95
4.2.4 LDS demonstration with neat CdSe/CdS core/thick-shell film . . . 100
4.2.4.1 Film absorbance and emission . . . 100
4.2.4.2 Measuring and modeling film scatter . . . 102
4.2.4.3 Resulting EQE of neat-film CdSe/CdS LDS detector . . . 104
4.2.5 LDS demonstration with a QD-hydrocarbon polymer film . . . 108
4.2.6 Low pressure and temperature QD-film behavior . . . 110

4.2.7 Imaging with QD-based LDS camera . . . 112
4.2.8 Bandwidth approximation. . . . 116
4.3 Conclusions and future scope. . . . 118
4.4 Experimental details . . . 118
4.4.1 QD synthesis and characterization. . . . 118
4.4.2 QD purification . . . 119
4.4.3 Film deposition . . . 119
4.4.4 Device characterization. . . . 120
4.5 Chapter-specific acknowledgements . . . 120
4.6 References . . . 121

5 Prospects for the Extension of Luminescent Downshifting into the MWIR 127
5.1 Introduction . . . 127
5.2 Considerations of MWIR downshifting challenges. . . . 128
5.2.1 FRET reduction. . . . 128
5.2.2 Wavelength dependence of QY and low temperature improvement. 131
5.3 Predicted efficiency improvement of QD-based UV-MWIR detectors 133
5.4 Conclusions and future scope . . . 135
5.5 Experimental details . . . 135
5.5.1 QD preparation. . . . 135
5.5.2 Ligand exchange and polymer incorporation . . . 136
5.5.3 Low temperature measurements . . . 137
5.6 Chapter-specific acknowledgements . . . 137
5.7 References . . . 138

A Considerations of Lead Chalcogenide Surface Modification: Challenges of Shell Growth and Effects of Stoichiometry 139
A.1 Introduction . . . 139
A.2 Cation exchange route to thick-shelled PbSe/PbS and PbSe/PbS QDs. . . 141
A.2.1 Cation exchange via intermediate. . . . 141
A.2.2 Direct cation exchange. . . . 143
A.3 Exploration of epitaxial growth for shell growth . . . 144
A.3.1 Challenge of PbS thermal stability . . . 144
A.3.2 Shell material considerations . . . 146
A.3.3 Precursor considerations . . . 149
A.3.4 Attempted shell growth . . . 150
A.3.5 Impact of stoichiometry. . . . 159

A.4 Conclusions and future scope 160
A.5 Experimental 160
A.5.1 Synthesis. 160
A.5.2 Materials characterization 161
A.6 Chapter-specific acknowledgements 161
A.7 References 161

List of Figures

1.1 Illustration of a 1-D particle-in-a-box 21
1.2 Size dependent optical properties of QDs 22

2.1 Fundamental limitations of photodetector spectral range 33
2.2 Illustration of a LDS-sensitized detector 35
2.3 Illustration of parameters of a LDS film used for EQE modeling 37
2.4 Comparison of potential LDS fluorophores 39
2.5 Impact of energy transfer on in-film QY 41
2.6 Illustration of integrating sphere measurements of QY 47
2.7 Measurements of QY via integrating sphere 49

3.1 Schematic of UV-to-SWIR downshifting 58
3.2 Absorption, emission and EQE of bare detector used in downshifting 60
3.3 Evaluation of QD-polymer composite QY in various polymers 61
3.4 QY stability of QD-polymer films 63
3.5 Experimental and calculated EQE curves of bare and enhanced InGaAs 65
3.6 Temperature dependent PL characteristics of PbS QD-polymer films 67
3.7 Calculated low temperature enhancement of QD LDS InGaAs detectors 67
3.8 Measured low temperature enhancement of QD LDS Ge detectors 68
3.9 UV transmissive filter design 69
3.10 Resulting EQE with UV-filter 70
3.11 Downshifting schemes for camera integration 72
3.12 Examples of imaging with different LDS schemes 73
3.13 Chromatic aberration 74
3.14 Bandwidth measurement of LDS detector 76
3.15 Measured PL lifetime of a PbS-PMMA film 77

4.1 UV spectral region designations 86
4.2 Line-of-sight vs. non-line-of-sight communication 89
4.3 Influence of oleic acid ligands on parasitic UV absorbance 94
4.4 Comparison of polymer transmission 97
4.5 Benefits of thick-shelled CdSe/CdS for in-film FRET reduction 99
4.6 Emission change of QDs in-film and in-solution 101

4.7 Absorbance and emission of thick-shelled CdSe/CdS 101
4.8 Measured and modeled scatter of neat CdSe/CdS film 103
4.9 EQE enhancement of a silicon detector via a QD-neat film 105
4.10 QY stability of a neat film of thick-shelled CdSe/CdS 107
4.11 EQE enhancement of a silicon detector via a QD-polymer film 109
4.12 Low temperature PL stability of a CdSe/CdS neat film 111
4.13 LDS imaging array scheme 113
4.14 Downshifted imaging examples 113
4.15 Passive solar UV illumination 115
4.16 Relay detection with 222 nm light 117
4.17 Photoluminescent lifetime of thick-shelled CdSe/CdS neat film 117

5.1 Transmission spectra of PMMA compared to the fluorinated polymer CYTOP 130
5.2 Low temperature PL characteristics of PbSe/CdS-CYTOP films 132
5.3 Estimated EQE of a QD-based MWIR LDS detector 134

A.1 Illustration of core-shell energetic heterostructures 140
A.2 Change in PL of CdSe/CdS after lead cation exchange 143
A.3 TEM of QDs pre- and post- cation exchange 144
A.4 PbS temperature stability 145
A.5 TB-LMTO DOS calculations for SnS and PbS in the *Fm-3m* structure 148
A.6 Change in PL spectra with attempted shell growth 151
A.7 TEM of aliquots taken during attempted shell growth 152
A.8 PL and QY changes with individual additions of sulfur or tin 152
A.9 Changes in optical properties of PbS with concurrent addition of tin and sulfur 154
A.10 PL lifetime change with tin and sulfur addition 155
A.11 Change in PL lifetime with only sulfur addition 155
A.12 Hole and electron mobility modificaiton 158
A.13 Hole and electron mobility modification experimental control 158

Portions of the data represented in this text have been previously published in the following texts:

S. M. Geyer, J. M. Scherer, F. B. Jaworski, M. G. Bawendi. "Multispectral Imaging via Luminescent Downshifting with Colloidal Quantum Dots." *Optical Materials Express.* **3**, 1167-1175 (2013).

S. M. Geyer, J. M. Scherer, M. D. Jack, M. G. Bawendi, F. B. Jaworski. "Dual-Band Ultraviolet-Short-Wavelength Infrared Imaging via Luminescent Downshifting with Colloidal Quantum Dots." *Journal of Nanophotonics.* **7**, 073083 (2013).

S. M. Geyer, J. M. Scherer, N. Moloto, F. B. Jaworski, M. G. Bawendi. "Efficient Luminescent Down-Shifting Detectors Based on Colloidal Quantum Dots for Dual-Band Detection Applications." *ACS Nano.* **5**, 5566-5571 (2011).

Chapter 1

Introduction to Colloidal Quantum Dots

1.1. Introduction to QDs

Since the invention of the transistor, the now $350 billion dollar semiconductor industry has grown to permeate many central aspects of modern daily life [1, 2]. Of significant importance to the industry's development is fundamental research on semiconductor electronic structure, which dictates much of a material's optical and electronic properties. As a consequence, generations of scientists have sought to understand, utilize, and modify these energy levels, and with a great deal of effort, the material set continues to expand. It is with an acknowledgment of this arduous development that nanocrystaline semiconductor crystals, known as quantum dots, exhibit one of their most remarkable attributes: an electronic structure that can be tuned by changing the particle size.

In a bulk semiconductor a bound electron-hole pair, an exciton, exhibits an ideal separation distance where the kinetic energy and coulombic potential

are balanced. This most probable distance is known as the exciton Bohr radius, a_B, and is dictated by a material's dielectric constant, ε, and the effective masses of the electron, m_e^*, and hole, m_h^* (equation 1.1).

$$a_B = \frac{4\pi\hbar^2\varepsilon}{e^2}\left(\frac{1}{m_h^*} + \frac{1}{m_e^*}\right) \tag{1.1}$$

In a quantum dot, the physical size of the crystal is on the order of or smaller than the exciton Bohr radius, resulting in an additional confinement energy, $E_{confinement}$ [3, 4]. This confinement energy is directly analogous to the quantum mechanical particle-in-a-sphere model, where R represents the QD radius and the mass has been replaced by the electron and hole reduced masses. The resulting energy is shown in equations 1.2-4 and a one dimensional demonstration is illustrated in figure 1.1. An additional coulombic term, $E_{exciton}$, emerges to account for the increased coulombic interaction of the exciton[1].

$$E_g^{QD} = E_g^{bulk} + E_{confinement} + E_{coulombic} \tag{1.2}$$

$$E_{confinement} = \frac{\hbar^2\pi^2}{2R^2}\left(\frac{1}{m_h^*} + \frac{1}{m_e^*}\right) \tag{1.3}$$

$$E_{exciton} = -\frac{1.8e^2}{\varepsilon R} \tag{1.4}$$

This confinement results in a discretization of the bulk electronic structure, which manifests itself in the absorbance spectra where atomic-like transitions overlay a bulk-like continuum. Due to the increased wavefunction overlap of the electron and hole compared to a bulk, QDs also exhibit bright emission. As the confinement energy is a directly dependent on the

[1] While simplified, this model allows for an intuitive description of the size dependent behavior of QDs. More rigorous explorations can be found elsewhere.

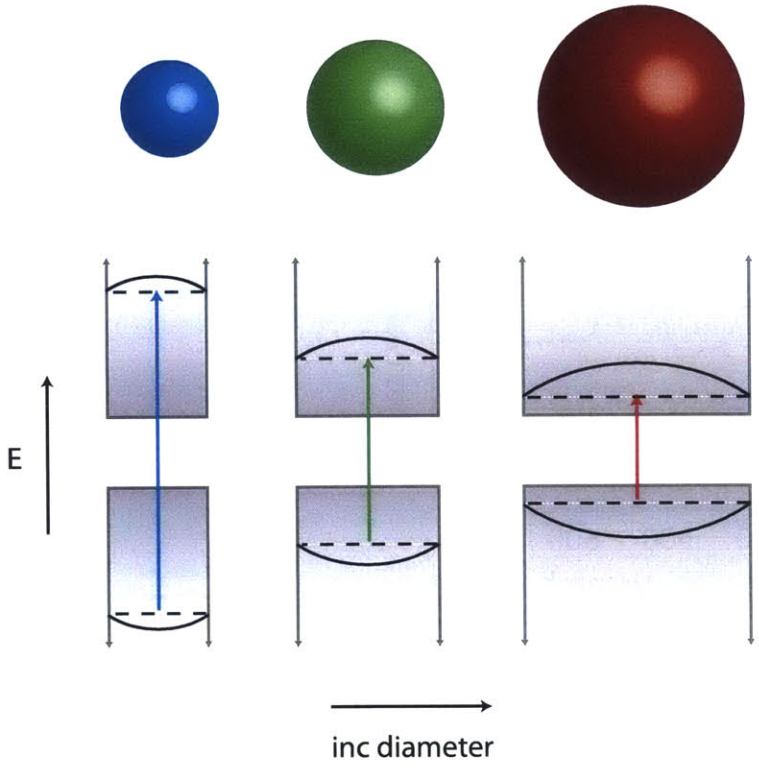

Figure 1.1 Illustration of a 1-D particle-in-a box. The energy levels are dependent on the length of the box, with increasing energy states resulting from small boxes. QD energy levels are directly analogous. Here quantization of both the electron and hole states are considered such that smaller QDs result in larger HOMO-LUMO transition energies than larger boxes.

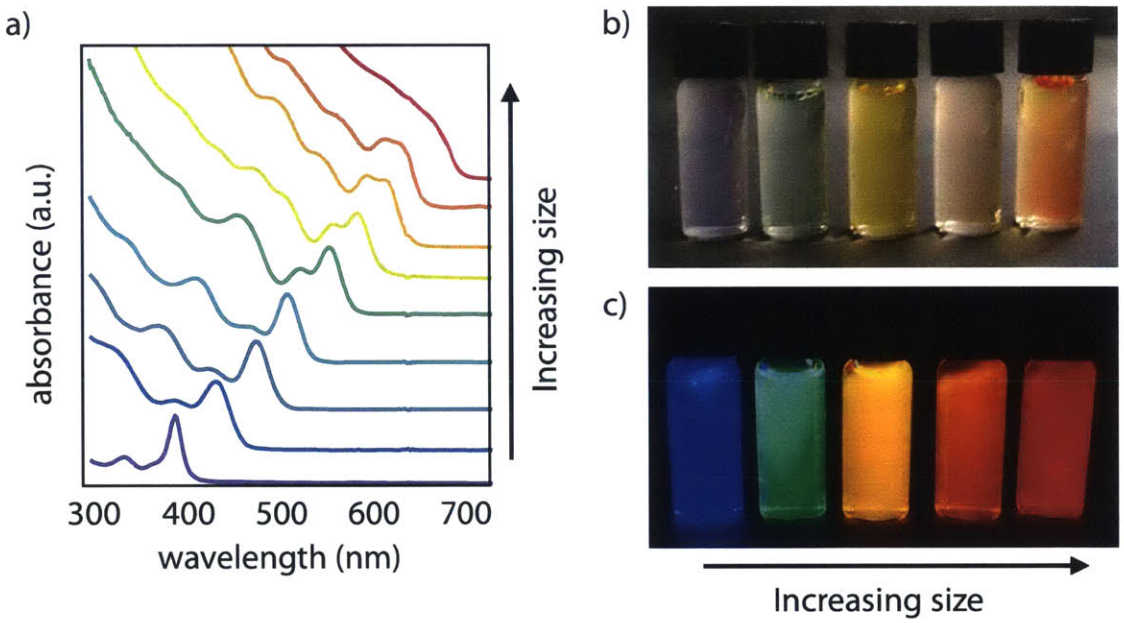

Figure 1.2 Size dependent optical properties of QDs. a) The absorbance spectra of a size series of CdSe QDs (Christopher Murray, MIT thesis 1995)[5]. Distinct transitions are apparent near the absorption onset resulting from discrete states. As the particles increase in size, the first absorption feature shifts to higher wavelengths/lower energies. This is visibly apparent in the photos of a size series of CdSe QDs shown in (b) and (c). The photo in (b) is taken with room lighting and the photo in (c) captures the bright QD emission while being excited with UV light.

particle's radius, simply changing the size of the QD allows for tuning of the absorption and emission properties. Figure 1.2 shows a size series of a CdSe QDs.

While the tunability of a QD is limited by the bulk band gap, a wider range of wavelengths can be accessed by modifying the parent material. For instance, the small band gap lead chalcogenides (PbX, X=S, Se, Te) allow for extension into the short and mid-wavelength infrared (SWIR and MWIR) and the wide band gap zinc chalcogenides (ZnX, X=S, Se, Te) reach into the ultraviolet (UV).

1.2 Synthetic fundamentals

A notable feature of colloidal quantum dots is their synthetic ease and versatility. While various synthetic routes have been explored, the most broadly employed technique was developed by in 1993 by Murray *et al.* [6]. This pivotal paper introduced the hot injection method, allowing for the rapid creation of a large quantity of particles, drastically improving the size dispersity, and opening the doors to the exploration of new material sets. Exploiting theories of particle nucleation developed in the 1950s [7], the hot-injection synthesis relies on the supersaturation of QD precursors to initiate particle formation. Consider the synthesis of CdSe QDs. At a high temperature, a solution of Se-precursors is quickly injected to a flask of rapidly stirring high boiling point solvents and Cd-precursors. This fast addition of Se-precursors results in a sufficiently high local concentration to overcome the nucleation threshold of the system. The reaction quickly transitions out of nucleation into a growth period. This transition is mediated by the partial cooling resulting from the room temperature injection,

the rapid precursor consumption, and the equilibration of precursor concentration density. The synthetic pot generally includes an appropriate ligand to facilitate nucleation and stabilize the resulting particles during growth and post-synthetic processing. The particle size can be tuned by a number of simple means including modifying the injection temperature or volume, tuning the post-injection growth period, or by changing the quantity of coordinating solvent.

Extensive efforts have sought to tune precursor type, reactivity and solvent properties allowing for the synthesis of more monodispersed, higher quality particles [8-11]. For the class of CdSe QDs, synthetic advances have resulted in extremely monodispersed particles [12]. A wide range of other less mature quantum dots have been produced via this method, and the quality of these materials continue to improve.

1.3 The importance of surfaces

Due to their high surface-to-volume ratio, QD surfaces influence much of their electrical and optical behavior [13]. As a truncated crystal, the surface atoms have unfulfilled valences. While valences can be partially fulfilled by surface ligands, any remaining under-bonded atoms can potentially contribute to in-gap states. In-gap states degrade numerous QD attributes by introducing decay pathways for exciton and carrier recombination, resulting in lower emissive quantum yields (QY), and reduced carrier extraction and/or open circuit voltages when utilized in photoconductive and photovoltaic devices.

One of the most important strategies to address these trap states has been the addition of a shell [14]. An epitaxial shell of a larger-gapped inorganic

semiconductor can minimize the exciton or carrier's wavefunction interaction with the surface localized decay pathways, reducing the probability of recombination. For example, the utilization of CdS shells on CdSe QDs has been incredibly successful at improving the particles' emissive properties, boosting their QYs from typical core-only values ranging from 5-30% to near unity for high quality core-shell materials[12]. Shell development has been explored for many of the other classes of QDs leading to the expansion of material sets and electronic structure modifications.

A second promising method to address non-radiative decay is stoichiometric modification. Most QDs contain unequal amounts of cations and anions, and the field has begun to attribute some types of non-radiative pathways to this mismatch [15-17]. Recently, Gao *et al.* demonstrated a means to stoichiometrically engineer CdSe core-only particles to exhibit unity QYs and highly monoexponential lifetimes, which indicates a single recombination species rather than trap state recombination [18]. Stoichiometry engineering has introduced an exciting new avenue to create high quality particles suitable for a range of applications.

While the surface modification of visible materials has led to significant advances in particle quality, the important yet more juvenile material set of lead chalcogenides has only recently seen steps toward improvements. Appendix A discusses the challenges and attempts to overcome shell growth on PbS and PbSe and the photophysical effects of stoichiometric modification.

1.4 Device applications of QDs

The unique properties of QDs lend themselves to an expansive body of device physics research [19-21]. Briefly, these applications can be grouped into QDs adopting the role as an as active conductor or a passive emitter or absorber. Primarily as a result of their easily tunable band gaps and solution processability, QDs have emerged as an active material candidate for low cost solar cells, photodetectors, and LEDs where carriers are shuttled through the QDs. However, their discrete nature results in a hopping conduction mechanism which leads to low carrier motilities compared to bulk counterparts [22, 23]. As this mobility can be related to the tunneling probability between QDs, significant efforts in the field of QD device physics has focused on the modification of the interstitial material's energetic barrier height and spatial width without negatively impacting the QD surface.

Alternatively, QDs have been passively employed in device constructs. For instance, an extremely compact QD-based spectrometer was developed which utilizes the tunable absorptive properties of QDs to create an array of slightly shifted filters [24]. Additionally, one of the first commercially available QD products originated from QD Vision. Here, brightly emitting QDs were utilized to shift the spectrum of highly efficient but unpalatably-colored LEDs to a more pleasing sun-like spectrum. The technology was eventually transitioned by the same company to produce vivid color-pure LCD televisions [25]. In a similar vein, Chapters 2-5 will discuss the use of QDs to passively extend the sensitive range of a photodetector by downshifting. The method will be explored for a variety of QDs and wavelengths with unique considerations of challenges for each system.

1.5 References

[1] Q4 2015 semiconductor market figures. https://www.wsts.org/PRESS/Recent-News-Release. (accessed on 4/22/2016).

[2] K. Zheng, K. Žídek, M. Abdellah, N. Zhu, P. Chábera, N. Lenngren, Q. Chi and T. Pullerits. "Directed Energy Transfer in Films of CdSe Quantum Dots: Beyond the Point Dipole Approximation." *Journal of the American Chemical Society*, **136**, 6259 (2014).

[3] L. Brus. "Electronic wave functions in semiconductor clusters: experiment and theory." *The Journal of Physical Chemistry*, **90**, 2555 (1986).

[4] M. G. Bawendi, M. L. Steigerwald and L. E. Brus. "The quantum mechanics of larger semiconductor clusters ('quantum dots')." *Annual Review of Physical Chemistry*, **41**, 477 (1990).

[5] A. W. Wills, M. S. Kang, A. Khare, W. L. Gladfelter and D. J. Norris. "Thermally Degradable Ligands for Nanocrystals." *ACS Nano*, **4**, 4523 (2010).

[6] C. B. Murray, D. J. Norris and M. G. Bawendi. "Synthesis and characterization of nearly monodisperse CdE (E = sulfur, selenium, tellurium) semiconductor nanocrystallites." *Journal of the American Chemical Society*, **115**, 8706 (1993).

[7] V. K. LaMer and R. H. Dinegar. "Theory, Production and Mechanism of Formation of Monodispersed Hydrosols." *Journal of the American Chemical Society*, **72**, 4847 (1950).

[8] F. C. J. M. van Veggel. "Near-Infrared Quantum Dots and Their Delicate Synthesis, Challenging Characterization, and Exciting Potential Applications." *Chemistry of Materials*, **26**, 111 (2014).

[9] S. Liu and X. Su. "The synthesis and application of I-III-VI type quantum dots." *RSC Advances*, **4**, 43415 (2014).

[10] M. P. Hendricks, M. P. Campos, G. T. Cleveland, I. Jen-La Plante and J. S. Owen. "A tunable library of substituted thiourea precursors to metal sulfide nanocrystals." *Science*, **348**, 1226 (2015).

[11] D. K. Harris and M. G. Bawendi. "Improved Precursor Chemistry for the Synthesis of III–V Quantum Dots." *Journal of the American Chemical Society*, **134**, 20211 (2012).

[12] O. Chen, J. Zhao, V. P. Chauhan, J. Cui, C. Wong, D. K. Harris, H. Wei, H.-S. Han, D. Fukumura, R. K. Jain and M. G. Bawendi. "Compact high-quality CdSe–CdS core–shell nanocrystals with narrow emission linewidths and suppressed blinking." *Nat Mater*, **12**, 445 (2013).

[13] M. A. Boles, D. Ling, T. Hyeon and D. V. Talapin. "The surface science of nanocrystals." *Nat Mater*, **15**, 141 (2016).

[14] P. Reiss, M. Protière and L. Li. "Core/Shell Semiconductor Nanocrystals." *Small*, **5**, 154 (2009).

[15] D. Kim, D.-H. Kim, J.-H. Lee and J. C. Grossman. "Impact of Stoichiometry on the Electronic Structure of PbS Quantum Dots." *Physical Review Letters*, **110**, 196802 (2013).

[16] D. Zherebetskyy, Y. Zhang, M. Salmeron and L.-W. Wang. "Tolerance of Intrinsic Defects in PbS Quantum Dots." *The Journal of Physical Chemistry Letters*, **6**, 4711 (2015).

[17] N. C. Anderson, M. P. Hendricks, J. J. Choi and J. S. Owen. "Ligand Exchange and the Stoichiometry of Metal Chalcogenide Nanocrystals: Spectroscopic Observation of Facile Metal-Carboxylate Displacement and Binding." *Journal of the American Chemical Society*, **135**, 18536 (2013).

[18] Y. Gao and X. Peng. "Photogenerated Excitons in Plain Core CdSe Nanocrystals with Unity Radiative Decay in Single Channel: The Effects of Surface and Ligands." *Journal of the American Chemical Society*, **137**, 4230 (2015).

[19] D. V. Talapin and J. Steckel. "Quantum dot light-emitting devices." *MRS Bulletin*, **38**, 685 (2013).

[20] J. Jean, P. R. Brown, R. L. Jaffe, T. Buonassisi and V. Bulovic. "Pathways for solar photovoltaics." *Energy & Environmental Science*, **8**, 1200 (2015).

[21] D. V. Talapin, J.-S. Lee, M. V. Kovalenko and E. V. Shevchenko. "Prospects of Colloidal Nanocrystals for Electronic and Optoelectronic Applications." *Chemical Reviews*, **110**, 389 (2010).

[22] D. Vanmaekelbergh and P. Liljeroth. "Electron-conducting quantum dot solids: novel materials based on colloidal semiconductor nanocrystals." *Chemical Society Reviews*, **34**, 299 (2005).

[23] H. Liu, A. Pourret and P. Guyot-Sionnest. "Mott and Efros-Shklovskii Variable Range Hopping in CdSe Quantum Dots Films." *ACS Nano*, **4**, 5211 (2010).

[24] J. Bao and M. G. Bawendi. "A colloidal quantum dot spectrometer." *Nature*, **523**, 67 (2015).

[25] T.-H. Kim, S. Jun, K.-S. Cho, B. L. Choi and E. Jang. "Bright and stable quantum dots and their applications in full-color displays." *MRS Bulletin*, **38**, 712 (2013).

Chapter 2

Introduction to Luminescent Downshifting and Methods of Characterization

2.1. Introduction

Although the capability to detect a broad spectral range finds use in a number of applications, the spectral range of sensitivity for photodetectors is fundamentally constrained by device physics [1-5]. For many broadband applications, this necessitates the use of multiple detectors, significantly increasing size, weight, power and cost requirements. Alternatively, a detector's active region can be modified to expand its spectral reach. However, commonly utilized methods often reduce the native efficiency and require increased production complexity and cost [6, 7]. This chapter will introduce luminescent downshifting (LDS) as an alternative means to expand the spectral range of a photodetector with minimal reduction of its efficiency.

2.2 Fundamental limitations of photodetectors

An idealized photodetector or solar cell is capable of efficiently harvesting all light, however fundamental limitations restrict their spectral range of sensitivity. The basic challenge in the pursuit of highly efficient thin film optoelectronics is creating a device which maximizes both absorption and carrier extraction. For a typical semiconductor, the probability of absorbing a photon with energy much greater than the band gap is larger than absorbing a photon at or near the band gap due to the increased number of possible higher energy transitions. This can be illustrated by considering the free electron gas model of density of states (DOS), where $DOS \propto \sqrt{E}$ (figure 2.1a). As a consequence, higher energy photons are superficially absorbed whereas photons on the order of the band gap are absorbed at a greater depth.

As a result, in the context of a p-n junction photodetector, carriers created near the surface from the absorption of high energy photons fail to be extracted due to insufficient carrier diffusion length or increased recombination due to surface defects. Conversely, lower energy photons are absorbed within the diffusion length of the detector's depletion region, creating carriers that can be extracted as an electrical signal (figure 2.2b). In order to increase the sensitivity of a detector to higher energy light, the active area can be thinned (figure 2.2c); however, this reduces the absorption of lower energy light and results in a decreased efficiency at those wavelengths. Commercially alternative means to extend the spectral range of photodetectors have included thinning and

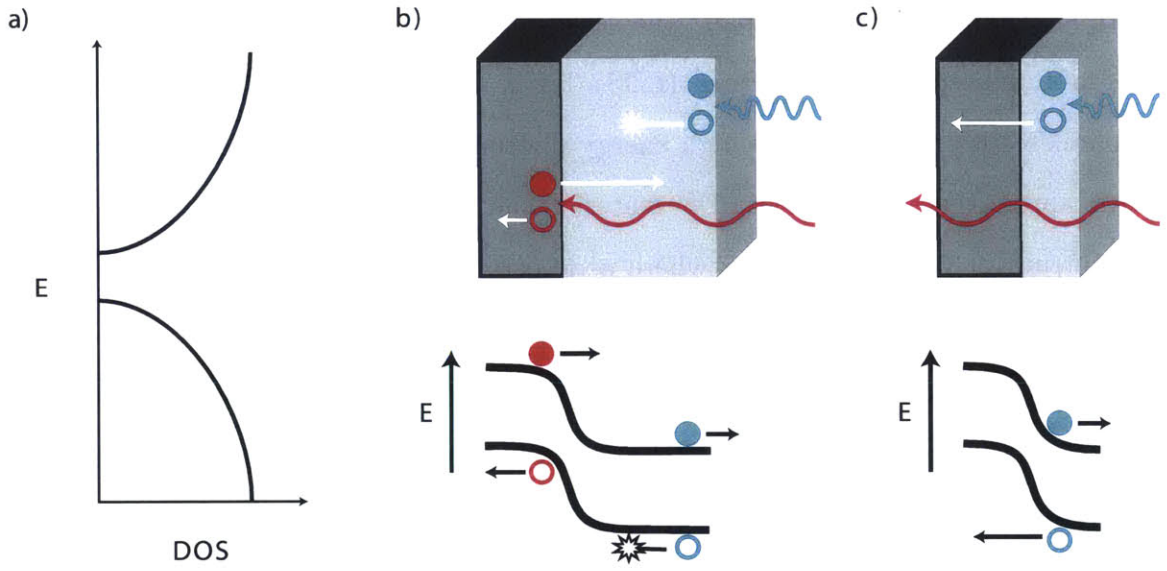

Figure 2.1 Fundamental limitations of photodetector spectral range a) The increased absorbance probability of higher energy transitions in a semiconductor can be partially understood by considering the free electron gas density of states (DOS) approximation. Here, due to the square root of energy dependence of DOS, the avaliable transitions are more numerous at higher energies than they are near the band gap. b) A p-n junction device demonstrates this effect. Although lower energy (red) photons are absorbed near the depletion region where the resulting carriers can be extracted as current, higher energy (blue) photons are absorbed superficially and the resulting carriers recombine before they can be extracted. c) The response to higher energy photons can be increased by thinning the device, however this reduces the lower energy photon absorption.

delta-doping, however these methods increase production complexity and cost [7, 8].

2.3 Luminescent downshifting

An alternative means to expand the sensitive range of a photodetector is the use of a luminescent downshifting (LDS) layer. LDS is the process by which a luminescent species absorbs high energy photons and re-emits at a lower energy. An appropriately designed LDS material can be utilized to shift the incident spectrum of light to a region where a detector can sense, effectively sensitizing the device to those higher energies (figure 2.2).

Although downshifting for photovoltaic spectral enhancement was first proposed in the 1970s [9], an absence of suitable materials have stymied it's development. Previous strategies to improve optoelectronic devices via LDS have employed fluorescent dyes and low quantum yield (QY) QDs as the downshifting medium [10, 11]. However, these attempts have failed to notably bolster quantum efficiencies due to inefficient downshifting. QDs have only recently emerged as a well-suited downshifting material dye due to recent developments in QD synthesis and design. This will be further discussed and demonstrated in Chapters 3-5.

2.4 Downconversion versus downshifting

An important distinction should be made between downshifting and downconversion. In this text, downshifting is considered the process by which a material absorbs incident light, undergoes vibrational relaxation to the LUMO or

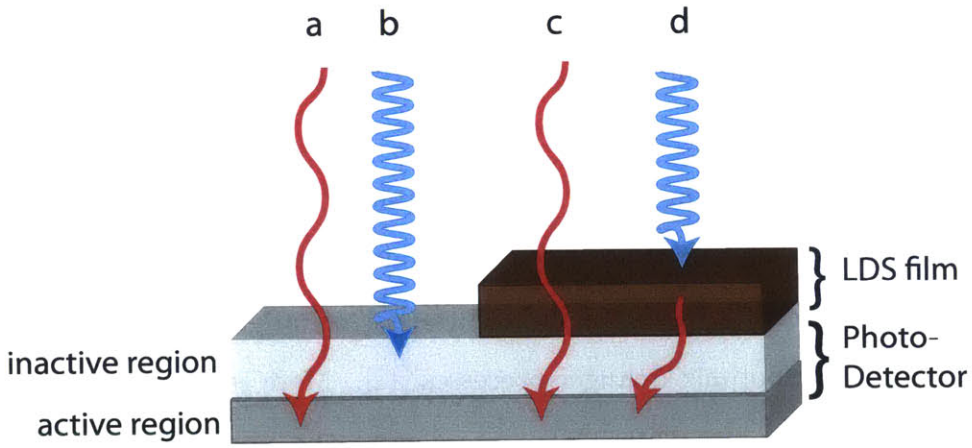

Figure 2.2. Illustration of a LDS-sensitized detector (a) Lower energy light is collected in the active region of the bare detector and resulting carriers are extracted as current. (b) Higher energy light is absorbed near the surface and carriers are collected at a low efficiency. (c-d) The LDS layer's absorbance is chosen such that it strongly absorbs the high energy light but allows the lower energy light to pass unobstructed. The LDS absorbs high energy light and re-emits lower energy light in the detector's sensitive region where it may be collected in the active region of the detector.

band edge, and re-emits at a lower energy. Consequently, while the photon number can be conserved, emissive energy is lost in the process. Alternatively, specific materials can absorb light, split this energy into multiple lower energy photons, and then re-emit, allowing for the possibility of conserving the total emissive energy. For the purposes of this text, this process will be referred to as downconversion.

Downconversion is an important process that has experienced a wealth of research, but its added complexity generally results in low efficiencies. The most common downconverting strategies include the use of rare-earth ions and doped bulk materials with optimized Auger processes [12]. More recently, the coupling of singlet fission organics with QDs has allowed the normally non-radiative triplet state energy to be transferred to emissive QDs, enabling the harvesting of both photons [13]. Despite these promising efforts, downconversion materials typically enable the collection of only a narrow wavelength range and efficiencies are currently poor.

2.5 Requirements of an efficient LDS material and modeling considerations

An ideal LDS material is capable of absorbing all incident light and transferring this energy to a desired spectral region. In order to achieve a highly efficient downshifting detector system, the chosen LDS material should meet several criteria, including a high absorption coefficient, broad spectral range, emission that overlaps with the most efficient spectral region of the detector, high in-film QY, long term stability, and minimal loses due to scatter and reflection.

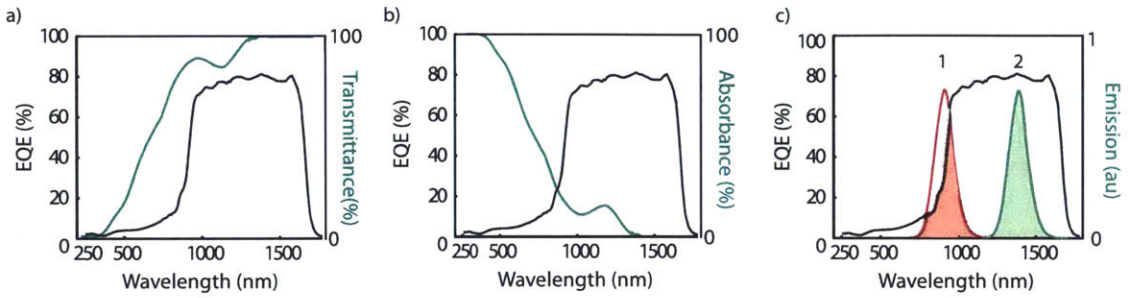

Figure 2.3. Illustration of parameters of a LDS film used for EQE modeling compared to the EQE of the bare detector (black) a) Percent transmission (green) b) Percent absorption (green) is approximately 1-T if scattering and reflection are low c) Emission-detector overlap. The green emission (2) is well aligned with the highest efficiency region of the bare detector but the red emission (1) is poorly aligned.

Considering these requirements, a simple model can be constructed to predict the performance of various LDS candidates. The overall external quantum efficiency (EQE) can be expressed as the summation of detected efficiencies of light transmitted (η_T) and absorbed (η_A) by the LDS film as illustrated by figure 2.3 and equations 2.1-4.

$$EQE_{LDS} = \eta_T(\lambda) + \eta_A(\lambda) \tag{2.1}$$

$$\eta_T(\lambda) = T(\lambda) \times EQE_{Bare}(\lambda) \tag{2.2}$$

$$\eta_A(\lambda) = A(\lambda) \times QY \times CE \times \eta_{Em} \tag{2.3}$$

The efficiency of the transmitted light is simply the product of the fraction of transmitted light, T, and the bare detector's efficiency at that wavelength, $EQE_{Bare}(\lambda)$. To determine the efficiency contribution of the absorbed light, multiple efficiencies are collected, including the fractional absorbance, A, the quantum yield, QY, the collection efficiency, CE, and the emission-overlap efficiency, η_{Em}. The emission-overlap efficiency accounts for the

overlap between the LDS emission and the detector's EQE spectrum and can be further expressed as equation 2.4 where P_{EM} is the LDS emission profile with a peak value normalized to 1.

$$\eta_{Em} = EQE_{Bare}(\lambda)\frac{\int P_{EM}(\lambda)\times\frac{EQE_{Bare}(\lambda)}{\max(EQE_{Bare})}}{\int P_{EM}(\lambda)} \tag{2.4}$$

The collection efficiency accounts for losses due to light emitted away from the detector and reabsorption. As the collection efficiency is difficult to accurately model, a number of simplifying approximations are made including negligible reabsorption, isotropic emission, and non-scattering surfaces. Assuming these approximations, the collection efficiency can be estimated with Fresnel equations. For a polymer matrix with an index of refraction of 1.49, the ideal collection efficiency is 87% [14]. Using this model, the efficiencies of potential downshifting media can be compared.

2.6 Comparison of downshifting materials: Dyes vs. QDs

For demonstrative purposes, consider enhancing the UV and visible regions of a short-wavelength IR (SWIR) InGaAs detector. Figure 2.4 compares the absorbance (black) and emission (gray) profiles of two of the highest QY IR emitting dyes, (a) indocyanine green (ICG) and (c) Q-Switch 5, with that of (e) lead sulfide QDs. The spectra are overlaid with the EQE of a bare InGaAs detector (black dashed). Although ICG exhibits a relatively high IR dye QY of 13%, its overlap integral with the InGaAs detector is low. Q- Switch 5

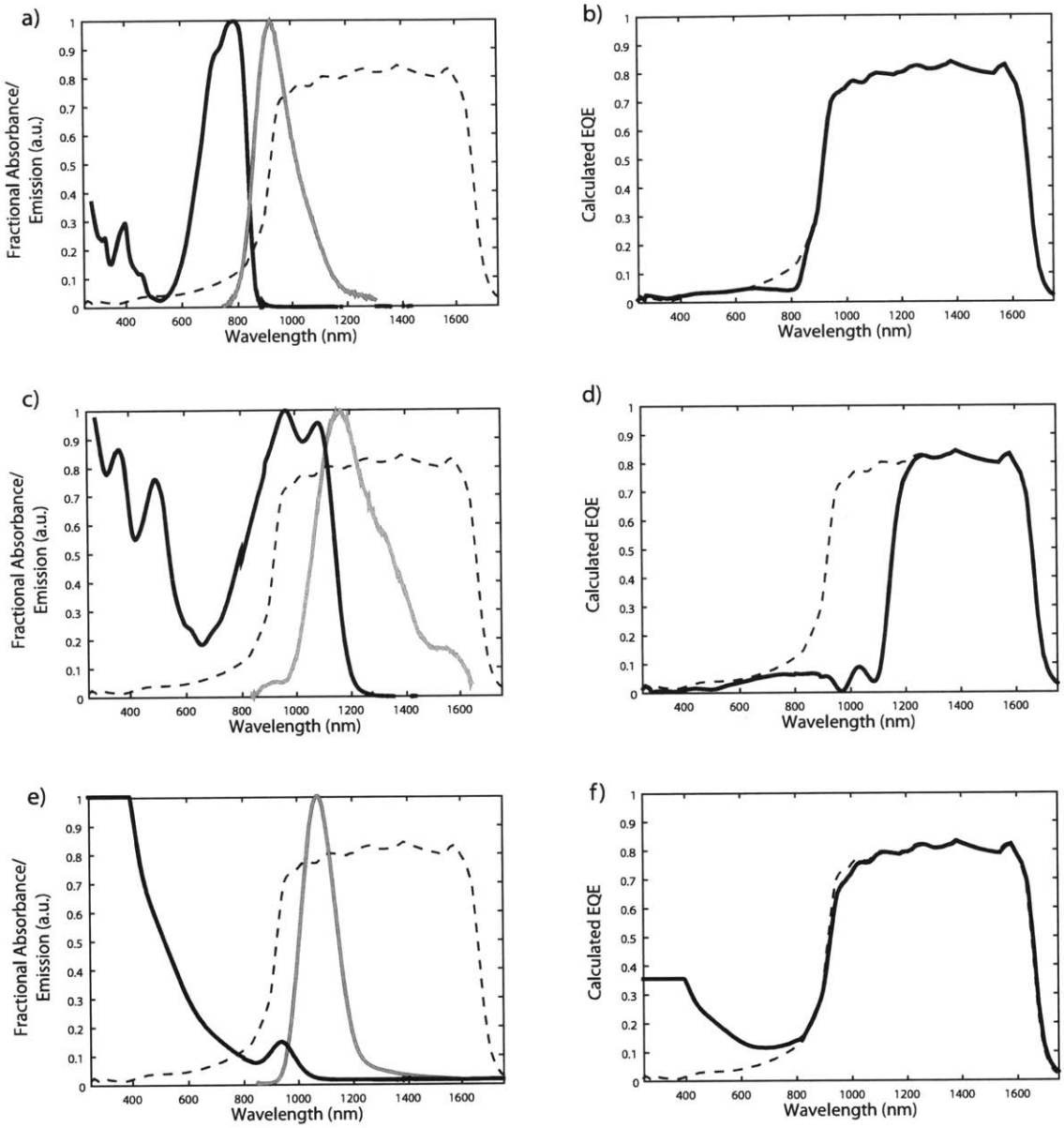

Figure 2.4. Comparison of potential LDS fluorophores. Absorbance (black) and emission (grey) are compared with a bare InGaAs detector EQE (black dashed) and the expected EQE change for these materials is shown in the figure to the right for ICG (a-b), Q-Switch 5 (c-d), and PbS QDs (e-f)

exhibits an improved overlap integral, but has a poor QY of 0.5%. In contrast, QD QYs can be greater than 50% in film at this emission wavelength and the emission can be tuned to optimize the emission-detector overlap.

The expected EQEs are shown in figure 2.4b,d,f for ICG, Q-Switch 5, and PbS QDs respectively. The collection efficiency was taken as unity, and each absorbance was normalized to its maximum value. Due to their poor QYs, the dyes actually lead to a reduction in EQE as the films effectively act as optical filters. Even with further increased absorbance, the maximum theoretical value of ICG is only 4% absolute in the UV and visible EQE. The high QY and broad absorbance of the QD example allows for significantly greater potential increases in the EQE, up to ~35% provided a physically reasonable QY of 50%.

It is clear from this demonstration that dyes are unsuitable for broadband downshifting in the IR. Although visible dyes can exhibit QYs of up to unity, their downshifting capability is still limited by their relatively narrow molecular absorption. To overcome the narrow absorbance of dyes, some have utilized multiple layers of dyes with varied absorbance and relied on reabsorption/emission or energy transfer to collect energy from a broader wavelength range [15, 16]. However, this adds additional complexity and often at a reduced efficiency.

2.7 The challenge of parasitic energy transfer

In order to achieve a functional LDS system, the downshifting material should be cast in a film. However, when emissive species are in close proximity, energy transfer can occur. Energy transfer becomes parasitic when light that is initially absorbed by an emissive QD transfers to a particle with accessible non-radiative

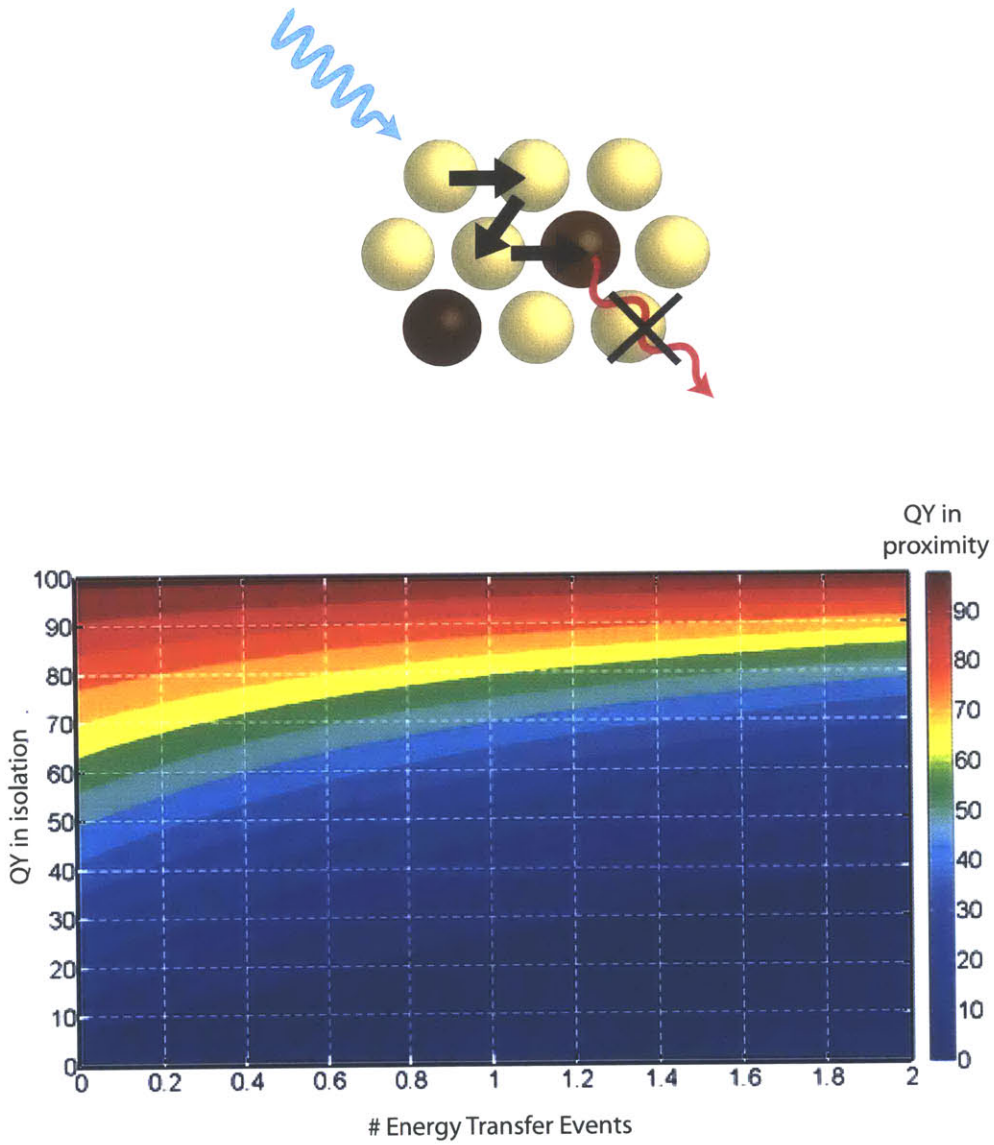

Figure 2.5. Impact of energy transfer on film QY (top) Illustration of reduction of in-film QY via energy transfer. (bottom) Estimated in-film QY given a native QY and a number of energy transfer events.

decay pathways and the energy is non-radiatively quenched (figure 2.5). As QY is a crucial factor in the ultimate performance of an LDS device, minimization of this energy transfer is imperative.

To demonstrate the significance of energy transfer on the QY of a film, consider a sample of QDs where the QY is taken as the probability at which each particle can emit. With each energy transfer event, there is an additional chance that the exciton can decay non-radiatively, reducing the QY with the number of transfer events. While this approximation is simplified, it demonstrates the significant potential reduction in QY films.

The most relevant form of non-radiative energy transfer for the scope of this text is Forster resonance energy transfer (FRET). The number of transfer events is dictated by the FRET efficiency. FRET efficiency is strongly dependent on distance ($1/r^6$) and the overlap integral of the donor's emission and acceptor's absorption.[1] Throughout this text, various wavelength-specific strategies to reduce FRET-induced quenching will be discussed which rely on tuning these parameters.

2.8 Relationship between QD lifetime and detector bandwidth

A detector's bandwidth is the maximum frequency at which signal can be discerned and conseqeutnly, dictates the maximum data transfer rate. Due to their long photoluminescent lifetime, the delay between QD absorbance and

[1] There is a further consideration to FRET efficiency regarding the donor-acceptor transition dipole alignment. For the case of spherical QDs, a simple estimation is a point-dipole approximation, however more complete treatments can be found elsewhere [21].

emission has the potential to further decrease the bandwidth when employed as an LDS layer.

Here, the relationship between PL lifetime and bandwidth are derived. The electrical bandwidth is the point at which the power falls by three decibels, or one half, of the initial value. This derivation will first consider the frequency dependence of the LDS-originated current. The current-squared proportionality to power can then be used to express the relationship between PL lifetime of a LDS film and bandwidth.

First, consider a rate equation for the generation and recombination of excitons in a LDS film which is proportional to the change in current measured by the detector:

$$\frac{dN}{dt} = IA - \frac{N}{\tau} \tag{2.5}$$

Where I is the photon flux, A is the fractional absorbance, N is the number of excitons, and τ is the measured PL lifetime. If one considers the oscillatory excitation function shown in equation 2.6 where I_o is the oscillation amplitude

$$I(t) = I_o \exp(-i\omega t) \tag{2.6}$$

$$\omega = 2\pi f \tag{2.7}$$

the differential equation can be solved such that

$$N(t) = \frac{\tau I_o A}{1+i\omega\tau} \exp(i\omega t) \tag{2.8}$$

Fourier transform of this expression provides

$$N(\omega) = \frac{\tau I_o A}{1+i\omega\tau} \tag{2.9}$$

Normalization results in the following expression:

$$\frac{N(\omega)}{N(0)} = \frac{1}{1+i\omega\tau} \tag{2.10}$$

The frequency response of the resulting current from a LDS layer is provided by the magnitude of expression 2.10:

$$\left|\frac{N(\omega)}{N(0)}\right| = \frac{1}{\sqrt{1+(\omega\tau)^2}} \tag{2.11}$$

The electrical bandwidth can now be determined. The electrical bandwidth is the point at which the power falls by three decibels or one half from its initial value. Our current expression is the frequency dependent current change measured by the LDS detector. As current squared is proportional to power, squaring equation 2.11, setting it equal to one half to reflect a decrease of three decibels, and solving for frequency will complete the derivation.

$$\left|\frac{N(\omega_{-3dB})}{N(0)}\right|^2 = \frac{1}{1+(\omega_{-3dB}\tau)^2} = \frac{1}{1+(2\pi f_{-3dB}\tau)^2} = \frac{1}{2} \tag{2.12}$$

$$f_{-3dB} = \frac{1}{2\pi\tau} \tag{2.13}$$

The resulting expression shown in equation 2.13 will be employed to estimate the effect of a LDS film on the bandwidth of a detector in regions where LDS is enhancing the response.

2.9 Measurement Methods

Chapters 3-5 will utilize many of the same measurements. To avoid redundancy, the details of frequently utilized home-built setups will be discussed here. Project-specific alterations to these measurements will be detailed in the appropriate chapter.

2.9.1 Quantum yield

A central figure-of-merit for a LDS film is the QY, which is the efficiency at which absorbed photons are re-emited. Two primary means exist to measure this parameter, each best suited to different scenarios: the dye comparison method and the use of an integrating sphere.

The dye comparison method is most commonly employed for visibly emitting solutions. Briefly, a dye with a known QY and overlapping absorbance spectra with the known sample is chosen [17, 18]. Solutions of each are prepared and concentrations adjusted such that their absorbance is equal at the chosen excitation wavelength. As each sample now absorbs the same number of photons, the integrated PLs can be compared to extract the QY using equation 2.14 which also takes into account the solvents' refractive indices.

$$\frac{QY}{QY_{ref}} = \frac{I}{I_{ref}} \frac{F_{ref}}{F} \frac{\eta^2}{\eta_{ref}^2} \tag{2.14}$$

Here, the subscript "ref" refers to the reference samples values whereas other parameters are those of the unknown sample. The unknown QY is solved by taking ratios of the reference and unknown's integrated PL, I, fractional absorption, F ($F=1-10^{-Absorbance}$), and the solvent's index of refraction, η. Ideally, a calibration curve is created where concentration is varied for each solution.

While this method benefits from simplicity, it suffers from a number of sources of error and care must be taken to obtain accurate values. As a comparison method, it is important for high accuracy that the QY of the standardized dye is comparable to the sample measured, has low variance, and is accurate; however discrepancies exist in the reported QYs of some commonly utilized dyes [17]. An additional source of error originates from the reabsorption

of emitted light. The re-emission probability is the QY, and consequently the process artificially reduces the QY of the sample. Minimizing absorbance to 0.08-0.1 is generally sufficient to mitigate this effect while still providing enough signal for measurements; however, a concentration dependent calibration curve is ideal.

If proper care is taken, the dye comparison method is an accurate means to evaluate the QY of a solution. This method is generally only suitable for visibly emitting solutions as there are few available stable dyes with accurately known QYs in the UV and IR. The dye comparison method is typically unsuitable for films owing to the difficulty of measuring the scatter and anisotropic emission of films. For these scenarios, utilization of an integrating sphere is more appropriate.

An integrating sphere is a hollow sphere whose interior is coated with a close-to-ideal Lambertian diffuse reflector, such as barium sulfate for the visible through short-wave infrared (SWIR) (~250 - 2500 nm) or textured gold for the near IR through the long wavelength IR (~0.8 nm - 20 μm). Consequently, the majority of light interacting with the inside of the sphere will be perpetually reflected until collected at a port by a detector. This allows for the collection of scattered and anisotopically emitted light. Some losses are incurred due to less-than-ideal reflection and escaped light at ports; however, considerations are taken to correct for these deviations.

While there are multiple QY measurement techniques which employ integrating spheres [19-21] only the method used to interrogate samples in this text will be detailed here. The measurement orientation is detailed in figure 2.6. A film or solution sample is loaded into an integrating sphere and a mechanically chopped, continuous wavelength laser diode excitation is directed through an entrance port. The laser's initial site of contact is the sphere's wall rather than the sample directly as to avoid direct reflection to an exit port. The sample is excited by the diffusely scattered excitation and the emission and remaining excitation is collected and measured by a calibrated photodetector via a lock-in preamplifier. To further minimize losses due to direct scatter or reflection of light to the detector, a baffle is situated between the sample and the detector.

The measurement of QY via this method requires the determination of

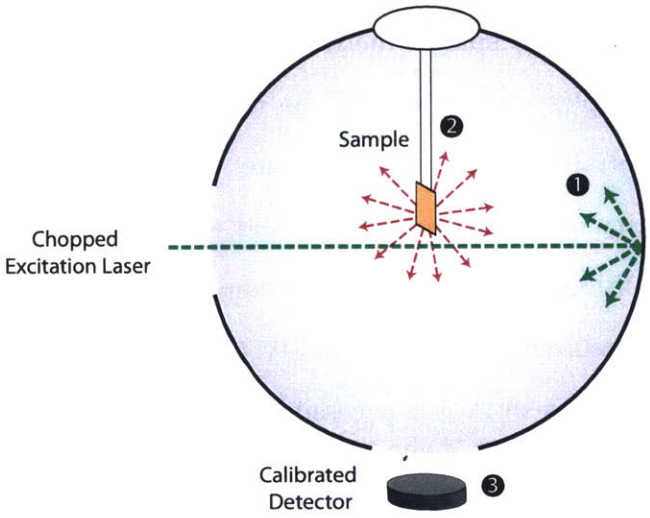

Figure 2.6: Illustration of integrating sphere measurements of quantum yield. A excitation laser is diffusely reflected off of the integrating sphere wall (1) which indirectly excites the sample (2). With an integrating sphere isotropic emission and scattered light can still be collected by a detector (3).

the number of photons absorbed and emitted by the sample. To this end, four consecutive measurements are performed on a suitable blank and the sample each with and without a long pass (LP) filter to block incident excitation. These four measurements are listed as follows and illustrated in figure 2.7: blank, no LP filter (BNF); blank with filter (BF); sample, no LP filter (SNF); sample, filter (SF).

As illustrated in figure 2.7, the number of photons emitted and absorbed can be calculated by solving these equations and accounting for the responsivity of the detector at appropriate wavelengths. The resulting QY can be approximated by equation 2.15 where λ_{PL} is the emission peak and λ_{exc} is the excitation laser wavelength.

$$QY = \frac{(SF-BF)/EQE(\lambda_{PL})}{\{(BNF-SNF)+(BF-SF)\}/EQE(\lambda_{exc})} \tag{2.15}$$

While the integrating sphere method allows for the measurement of a broader variety of samples, care must still be taken to achieve accurate values. Among many potential sources of error are reabsorption, laser intensity instability, nonlinearity of the photodetector, and a poor quality long pass filter. With the rational utilization of the dye comparison or integrating sphere techniques of QY measurement, the capability to measure the wide variety of samples encountered in this work was accessible.

2.9.2 External quantum efficiency

A photodetector's external quantum efficiency (EQE) is the percentage of incident photons that result in electrical current (equation 2.16).

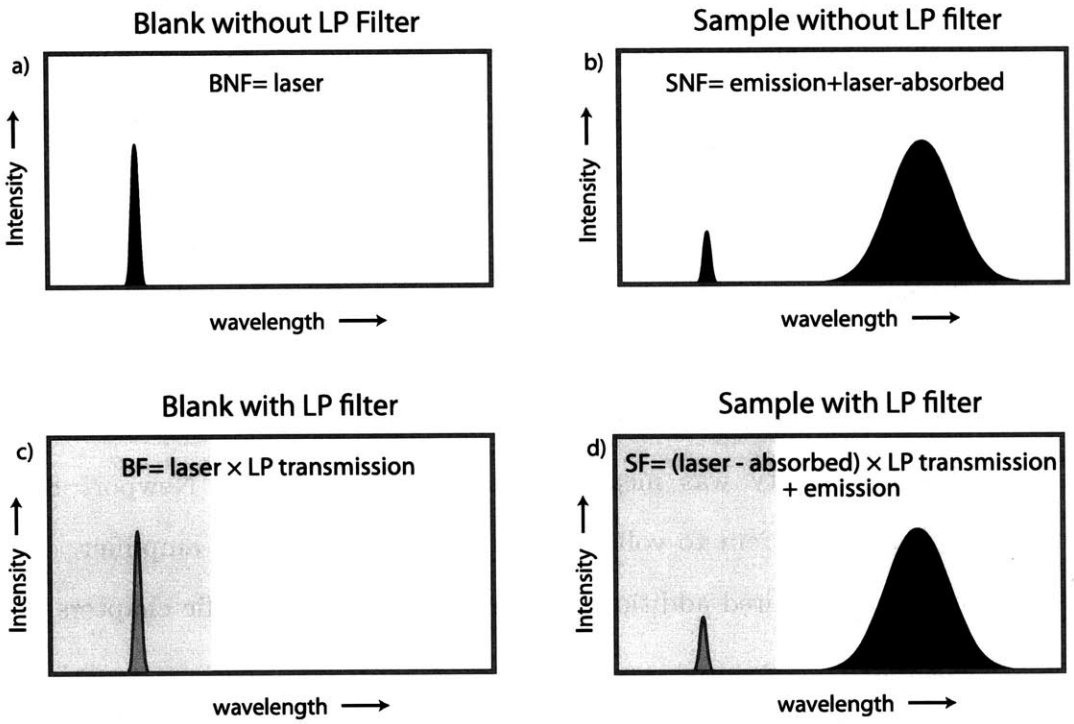

Figure 2.7 Measurements of QY via integrating sphere in this work were performed as outlined here. Four measurements were sequentially taken: the light intensity of a suitable blank and a sample with and without a long pass filter chosen to block excitation but pass emission. With consideration of the responsivity of the detector at the excitation and emission wavelengths and some algebra, the number of photons absorbed and emitted can be calculated.

$$EQE = \frac{\#\ incident\ photons}{\#\ electrons\ extracted} \tag{2.16}$$

In the work presented in chapters 3-5, a primary goal is to quantify the increase in EQE via downshifting.

An EQE measurement is performed by monitoring the extracted current from a photodetector as the incident wavelength is scanned. Provided that the light source is calibrated, the number of incident photons and extracted electrons can be determined.

For the wavelengths ranging from 290-1800 nm, a broad band white light source (xenon arc or tungsten black body) was chopped and dispersed by a monochromator. Parabolic mirrors were utilized to minimize chromatic aberration. Light intensity was measured with NIST calibrated Newport 818 detectors coupled to a current-to-voltage preamplifier and a lock-in amplifier. At times, measurements required additional means as detailed in specific chapters.

2.9.3 Photoluminescent lifetime

The photoluminescent (PL) lifetime, the average time between absorption and emission events, plays an important role in dictating the maximum measurement frequency, or bandwidth, at which a QD-enhanced detector may function, as was derived earlier in section 2.7.

The PL lifetimes presented in this text were measured by one of two ways. For dynamics greater than ~100 ns, the sample was excited with a 5 ns pulse-width 532 nm Nd:YAG laser and emission was recorded by a 10 ns rise-time biased silicon or InGaAs detector coupled to an oscilloscope. When shorter time dynamics were required or low emission intensity encountered, a time-correlated single photon counting (TCSPC) setup was used. Samples were

excited via either 532 nm or 785 nm pulses at a repetition rate of 100 kHz. Infrared and visible emission was measured via InGaAs/InP or silicon avalanche photodiodes.

2.10 Chapter-specific acknowledgements

Scott Geyer assisted in the construction of early versions of the EQE and integrating sphere setups and Igor Coropceanu contributed meaningful alterations to the integrating sphere setup. Mark Wilson and Lea Neinhaus constructed and maintained the TCSPC PL lifetime setup.

2.11 References

[1] E. Klampaftis, D. Ross, K. R. McIntosh and B. S. Richards. "Enhancing the performance of solar cells via luminescent down-shifting of the incident spectrum: A review." *Solar Energy Materials and Solar Cells*, **93**, 1182 (2009).

[2] G. Ariyawansa, M. B. M. Rinzan, M. Alevli, M. Strassburg, N. Dietz, A. G. U. Perera, S. G. Matsik, A. Asghar, I. T. Ferguson, H. Luo, A. Bezinger and H. C. Liu. "GaN/AlGaN ultraviolet/infrared dual-band detector." *Applied Physics Letters*, **89**, 091113 (2006).

[3] G. Ariyawansa, P. V. V. Jayaweera, A. G. U. Perera, S. G. Matsik, M. Buchanan, Z. R. Wasilewski and H. C. Liu. "Normal incidence detection of ultraviolet, visible, and mid-infrared radiation in a single GaAs/AlGaAs device." *Opt. Lett.*, **34**, 2036 (2009).

[4] D. Starikov, C. Boney, R. Pillai and A. Bensaoula. "Dual-band UV/IR optical sensors for fire and flame detection and target recognition." *in Sensors for Industry Conference, 2004. Proceedings the ISA/IEEE*,(2004).

[5] R. C. Jayasinghe, G. Ariyawansa, N. Dietz, A. G. U. Perera, S. G. Matsik, H. B. Yu, I. T. Ferguson, A. Bezinger, S. R. Laframboise, M. Buchanan and H. C. Liu. "Simultaneous detection of ultraviolet and infrared radiation in a single GaN/GaAlN heterojunction." *Opt. Lett.*, **33**, 2422 (2008).

[6] M. E. Hoenk, T. J. Jones, M. R. Dickie, F. Greer, T. J. Cunningham, E. R. Blazejewski and S. Nikzad. "Delta-doped back-illuminated CMOS imaging arrays: progress and prospects." *Proc. SPIE 7419, Infrared Systems and Photoelectronic Technology IV* (2009).

[7] H.-J Gossman and E.F. Schubert. "Delta doping in silicon." *Critical Reviews in Solid State and Materials Sciences,* 18:1,1-67 (2006).

[8] P. Jerram, D. Burt, N. Guyatt, V. Hibon, J. Vaillant and Y. Henrion. "Back-thinned CMOS sensor optimization." *Proc. SPIE 7598, Optical Components and Materials VII*, 759813 (2010).

[9] W. H. Weber and J. Lambe. "Luminescent greenhouse collector for solar radiation." *Appl. Opt.*, **15**, 2299 (1976).

[10] Z. Cheng, F. Su, L. Pan, M. Cao and Z. Sun. "CdS quantum dot-embedded silica film as luminescent down-shifting layer for crystalline Si solar cells." *Journal of Alloys and Compounds*, **494**, L7 (2010).

[11] K. R. McIntosh, G. Lau, J. N. Cotsell, K. Hanton, D. L. Bätzner, F. Bettiol and B. S. Richards. "Increase in external quantum efficiency of encapsulated silicon solar cells from a luminescent down-shifting layer." *Progress in Photovoltaics: Research and Applications*, **17**, (2009).

[12] B. S. Richards. "Luminescent layers for enhanced silicon solar cell performance: Down-conversion." *Solar Energy Materials and Solar Cells*, **90**, 1189 (2006).

[13] N. J. Thompson, M. W. B. Wilson, D. N. Congreve, P. R. Brown, J. M. Scherer, Thomas S. Bischof, M. Wu, N. Geva, M. Welborn, T. V. Voorhis, V. Bulović, M. G. Bawendi and Marc A. Baldo. "Energy harvesting of non-emissive triplet excitons in tetracene by emissive PbS nanocrystals." *Nat Mater*, **13**, 1039 (2014).

[14] S. M. Geyer, J. M. Scherer, N. Moloto, F. B. Jaworski and M. G. Bawendi. "Efficient Luminescent Down-Shifting Detectors Based on Colloidal Quantum Dots for Dual-Band Detection Applications." *ACS Nano*, **5**, 5566 (2011).

[15] V. Dryza, T. A. Smith and E. J. Bieske. "Blue to near-IR energy transfer cascade within a dye-doped polymer matrix, mediated by a photochromic molecular switch." *Phys Chem Chem Phys,* **18** 5095 (2016).

[16] M. Berggren, A. Dodabalapur, R. E. Slusher and Z. Bao. "Light amplification in organic thin films using cascade energy transfer." *Nature*, **389**, 466 (1997).

[17] A. M. Brouwer. "Standards for photoluminescence quantum yield measurements in solution (IUPAC Technical Report)." *Pure and Applied Chemistry*, **83**, (2011).

[18] A. T. R. Williams, S. A. Winfield and J. N. Miller. "Relative fluorescence quantum yields using a computer-controlled luminescence spectrometer." *Analyst*, **108**, 1067 (1983).

[19] K. Suzuki, A. Kobayashi, S. Kaneko, K. Takehira, T. Yoshihara, H. Ishida, Y. Shiina, S. Oishi and S. Tobita. "Reevaluation of absolute luminescence quantum yields of standard solutions using a spectrometer with an integrating sphere and a back-thinned CCD detector." *Physical Chemistry Chemical Physics*, **11**, 9850 (2009).

[20] A. K. Gaigalas and L. Wang. "Measurement of the fluorescence quantum yield using a spectrometer with an integrating sphere detector." *Journal of Research of the National Institute of Standards and Technology*, **113**, 17 (2008).

[21] J. C. de Mello, H. F. Wittmann and R. H. Friend. "An improved experimental determination of external photoluminescence quantum efficiency." *Advanced Materials*, **9**, 230 (1997).

Chapter 3

Near-UV-to-SWIR Broadband Detection and Imaging via Luminescent Downshifting

3.1 Introduction

Wide- or dual-band detectors spanning the ultraviolet (UV) to the short-wavelength infrared (SWIR) regions facilitates enhanced capabilities in application spaces as diverse as firefighting, communication, forensics, and remote sensing [1, 2]. However, acquiring data for such a wide wavelength range often requires the use of multiple and/or expensive detectors. In this chapter, the near-UV/visible sensitization of short-wavelength infrared (SWIR) detectors is explored via QD-based luminescent downshifting (LDS). The passive sensitization of both single-element detectors and imaging arrays is demonstrated.

3.1.1 Applications of near-UV-to-SWIR detection

UV-through-SWIR spectral information can be beneficial to a variety of applications by exploiting the unique light-matter interactions of each of these regions. For instance, UV light exhibits high scattering efficiency, allowing for short-range optical communication without the threat of long range interception [3]. In contrast, the high transmission of IR light provides long range imaging capability with little interference from atmospheric particulates or fog [4]. Additionally, for chemical identification purposes, a broad wavelength range provides a more complete fingerprint as UV, visible and SWIR light each access different types of optical transitions unique to a material [5]. Some of the most promising applications will be discussed below in further detail.

3.1.2 Remote sensing

Optical remote sensing is a broadly employed technique where light-matter interactions are measured to gain information about an object [6]. Variations in scatter, absorption, reflection, transmission and emission over a broad wavelength range are used for long-range identification and measurement. For instance, information about cloud coverage can be deduced by comparing the highly scattering UV to the transmissive IR, or active forest fires can be monitored via their IR radiation [7, 8]. Since many remote sensing applications require an aerial vantage, light-weight and compact systems are highly desired for deployment on satellites and aerial vehicles. Consequently, using multiple heavy and bulky detectors to acquire the desired spectra is not ideal.

Techniques in art history and restoration employ similar methods, as the layers of paint, varnish and pencil can be individually interrogated due to unique optical signatures [9]. For example using broadband imaging, art historians determined that the enigmatic Mona Lisa was not always eyebrow-less, but instead her eyebrows were likely accidentally removed during restorative cleaning [10, 11].

3.1.3 Chemical and biomedical analysis

The unique spectroscopic fingerprint that chemicals exhibit can be used to reveal the identity of a given substance. This technique has gained considerable interest in security applications as a means to identify explosives or other hazardous substances [12-14]. While multiple spectral regions have been utilized for material identification, broadband detection facilitates the measurement of a wider range of materials with higher accuracy.

Similarly, UV and SWIR imaging has found useful applications in biomedical spaces. As an example, light bruising can be more easily detected in the UV and IR than the visible due to the strong absorbance of bilirubin and water, respectively. Information in both of these regions allows forensic scientists to more accurately date bruises and other injuries including bite marks and burns [15].

3.1.4 Multifunctionality

In addition to opening avenues for novel and improved applications, a broadband detector offers increased multifunctionality. Payload-conscious applications, such as on-person or satellite deployments, are particularly restricted by size and

weight. By utilizing a broadband detector equipped with appropriate filters or dispersive optics, a single device can enable applications in various spectral ranges. For example, a broadband detector can allow a solider to engage in short-range UV communication and long-range SWIR tracking without adding substantial pack weight.

3.2 Results and discussion

In order to create a broadband near-UV-SWIR detector, infrared emitting PbS QDs were deposited on an InGaAs SWIR detector. This LDS layer absorbs the light at wavelengths shorter than the spectral range of the detector and reemits in the region of spectral sensitivity, as depicted in figure 3.1. The following sections will detail LDS film design, resulting efficiency improvements, and applications to imaging.

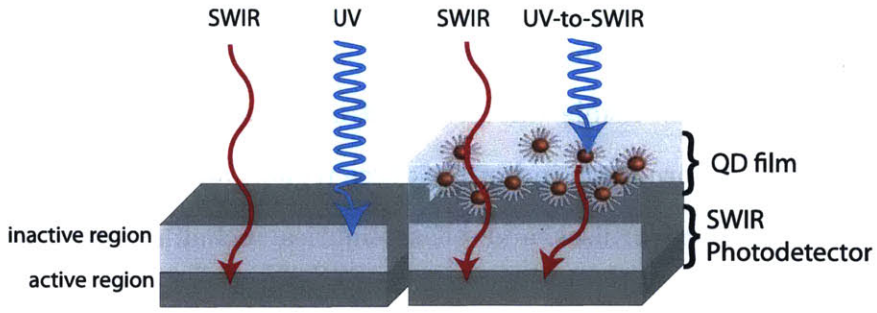

Figure 3.1 Schematic of UV-to-SWIR downshifting. Left: Although SWIR photons are absorbed in a region where the photocarriers can be extracted as current, higher energy photons are superficially absorbed and the resulting carriers are unable to be extracted. Right: A QD-coated downshifting layer absorbs high energy light and re-emits where the detector is sensitive while allowing the SWIR light to pass unaffected.

3.2.1 Film design

3.2.1.1 Material choice

In order to achieve an efficient LDS detector, the downshifting material must be bright and have suitable absorption and emission spectra such that the desired photons are shifted to the wavelength region in which the detector has spectral sensitivity. QDs are particularly well suited to this task due to their broad absorption, high QY, and tunable emission; however it is important to consider the feasibility of alternatives.

For this demonstration, an InGaAs SWIR detector will be used that exhibits a high detection efficiency from 900-1800 nm, and consequently, suitable downshifting candidates must emit in this region. Potential SWIR emissive LDS candidates include QDs and molecule dyes. Section 2.6 compared the downshifting capabilities of QDs with some of the highest quality commercial IR dyes. Unfortunately, the availability of long-wavelength emitting dyes is limited. Of these few options, the best molecular dyes have low QYs (<15%) and narrow absorption features, making them unsuitable for efficient broadband downshifting.

The drawbacks exhibited by IR dyes highlight the unique benefits of QDs as an IR downshifting medium. Figure 3.2 shows the absorbance and emission of PbS QDs whose size has been tuned to overlap with the InGaAs efficiency band. The broad absorption enables a wide potential for wavelength extension. The high QY (>50%) and tunable emission yields an efficient downshifting layer.

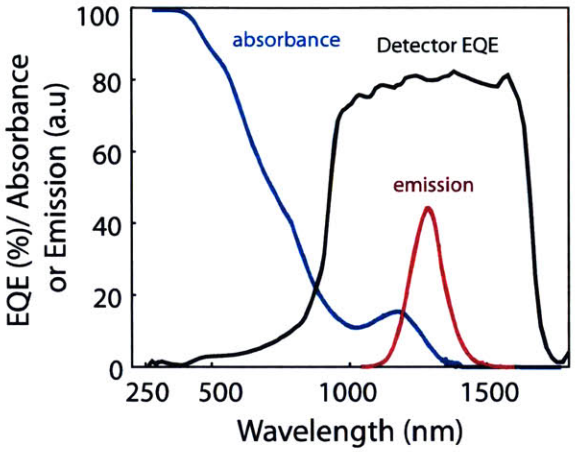

Figure 3.2 Absorption (red) and emission (blue) of a sample of QDs tuned to overlap with the EQE of a bare InGaAs detector (black).

3.2.1.2 FRET prevention

For employment of QDs as a LDS material, they must be cast in a solid film; however one consequence of this is parasitic energy transfer. When QDs are in close proximity, dot-to-dot energy transfer occurs via Forster resonance energy transfer (FRET), which is mediated by close-range dipole-dipole interactions and results in a decreased in-film QY (see section 2.6). In order to avoid such compromises in QY, the QD interparticle distances were increased by dispersing the QDs in a hydrocarbon polymer. Even a small increase in interparticle distance, *r,* can strongly inhibit FRET since FRET efficiency scales as $1/r^6$ [16].

Several considerations were made when optimizing the QD-polymer film. An ideal polymer is transparent from the near-UV through the SWIR and will effectively disperse the QDs. In the near-UV to SWIR wavelength range, there are many polymer options that exhibit high transmission; however, the task of preventing QD-polymer phase separation in a film is more challenging.

In order to find a suitable system, a number of polymers were evaluated. Promising choices included polymers with similar functional groups to the oleic acid ligands passivating the QDs. Such polymers are expected to provide the best dissolution. Of the polymers explored, the following five were found to be soluble in QD-compatible solvents and produce visibly low scattering films: poly(methyl methacrylate) (PMMA), poly(vinyl butyral) (PVB), poly(vinyl stearate) (PVS), poly(butyl methacrylate) (PBM) and poly(vinyl butyral-co-vinyl alcohol-co-vinyl acetate) (PVBcoPVAcoPVAc). The QYs of these films were evaluated as an indirect measure of FRET reduction. The QY was found to be highest for QDs in PVBcoPVAcoPVAc and PMMA matrices (figure 3.3). These two polymers were chosen for further exploration. It should be noted that the QDs used for this study exhibited much lower QYs than those used for the

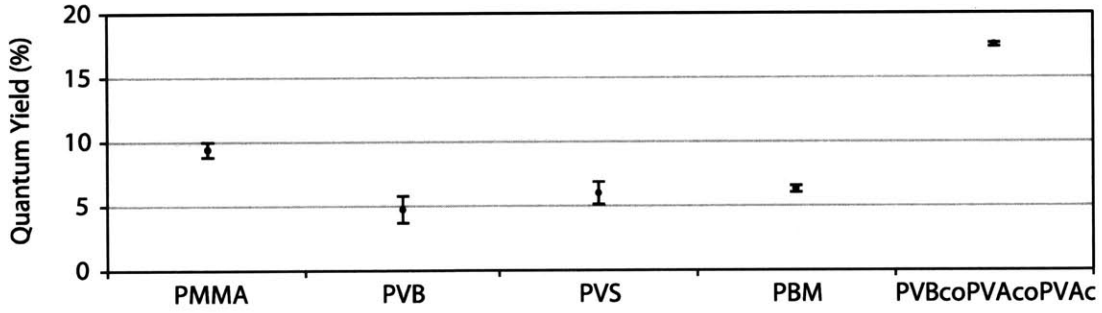

Figure 3.3 Evaluation of QD-polymer composite QY in a variety of hydrocarbon polymers. Error bars represent standard deviation of multiple measurements.

eventual LDS experiments.

In addition to a high in-film QY, long term QY stability is important for considerations of commercialization and robustness. Since PbS particles are known to exhibit reductions of QY in air [17], the QD-polymer films were monitored to determine the extent of degradation. The in-air QY stability of QD-polymer films deposited from PMMA (1.5% and 3% w/w in chlorobenzene) and PVBcoPVAcoPVAc (1.5% and 3% w/w in chlorobenzene) solutions compared to a neat film is shown in figure 3.4a. Although the QY in the neat film reduced by almost half, the QD-polymer films suffered a less significant loss of approximately 25% before stabilizing. It is apparent that the polymer provides some degree of air stability; however, this appears to be independent of the polymer or weight percentages used in this study.

The air-induced degradation can be mitigated through air-free packaging. Figure 3.4b compares the QY decrease in packaged versus unpackaged QD-PMMA films that have been stored in air. Although the packaged sample still exhibits a reduction in QY, potentially as a result of insufficient packaging or quenching due to interaction with the epoxy employed for packaging, the reduction is less than that of the unpackaged sample. As commercial detectors often require packaging, air-free integration of PbS onto a detector is not expected to further complicate detector fabrication.

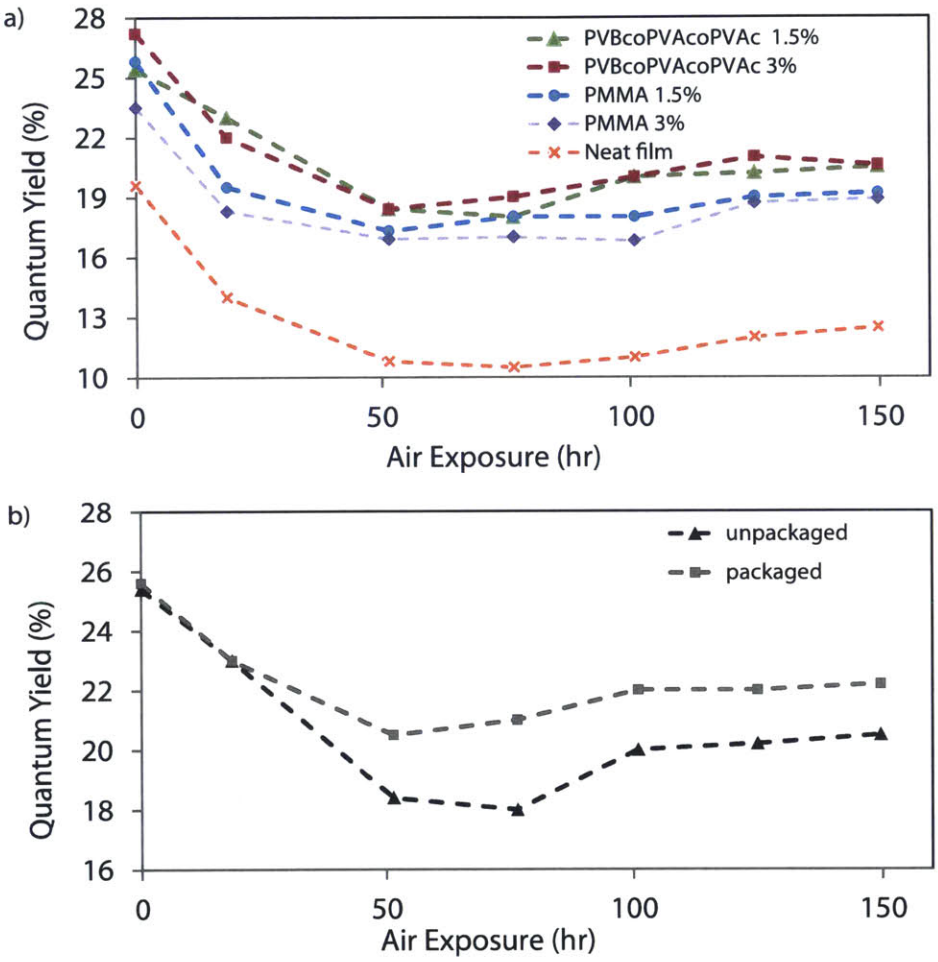

Figure 3.4 QY stability of QD-polymer films a) The long-term QY stability of various QD-polymer composites was measured and compared to a neat film. While the performance of the QD-polymer film was superior to that of the neat film, neither the weight percentage nor the identity of the polymer appeared to matter for this sample size. b) To demonstrate the origin of the QY reduction and to determine whether it could be mitigated, one film of 1.5% PVBcoPVAcoPVAc was packaged between two quartz slides while the other was left unmodified. Although the packaged sample still experienced a QY decrease, it was to a lesser extent than the unpackaged sample.

3.2.2. External quantum efficiency measurements

3.2.2.1 Room temperature performance

A 1.2 μm thick film of PbS QDs in PVBcoPVAcoPVAc was dropcast directly on the face of an InGaAs single-element detector. The measured room temperature external quantum efficiency (EQE) before and after QD deposition is shown in figure 3.5. An average 12-fold enhancement was obtained in the near-UV. These data fit well to the model constructed in section 2.4 provided a quantum yield of 45%, a collection efficiency of 62% and a fractional absorbance scaled to 1 at 490 nm. It should be noted that the discrepancy of the efficiency in the vicinity of 250 nm is a result of polymer absorption which is not accounted by the model.

This model can also be used to predict the EQE as the film's QY is improved. Here, an ideal collection efficiency was assumed, which can be approximated with Fresnel equations [18]. With Maxwell-Garnett effective medium theory, the refractive index is dominated by the polymer film at this QD inclusion concentration. Consequently, assuming the polymer-QD film index of refraction to be 1.49, the ideal collection efficiency is found to be 87%. The fractional absorbance is scaled such that all light is absorbed at wavelengths lower than 500 nm, the expected QD-enhanced EQEs with varying wavelengths are shown in figure 3.5b. From these estimations it is evident that with an optimized LDS layer, UV efficiencies of up to 75% can be achieved given this bare detector. Through use of a higher efficiency bare detector, further improvements can be gained.

This theoretical limit can also be increased provided improved refractive index matching between the LDS film and the detector's surface to minimize

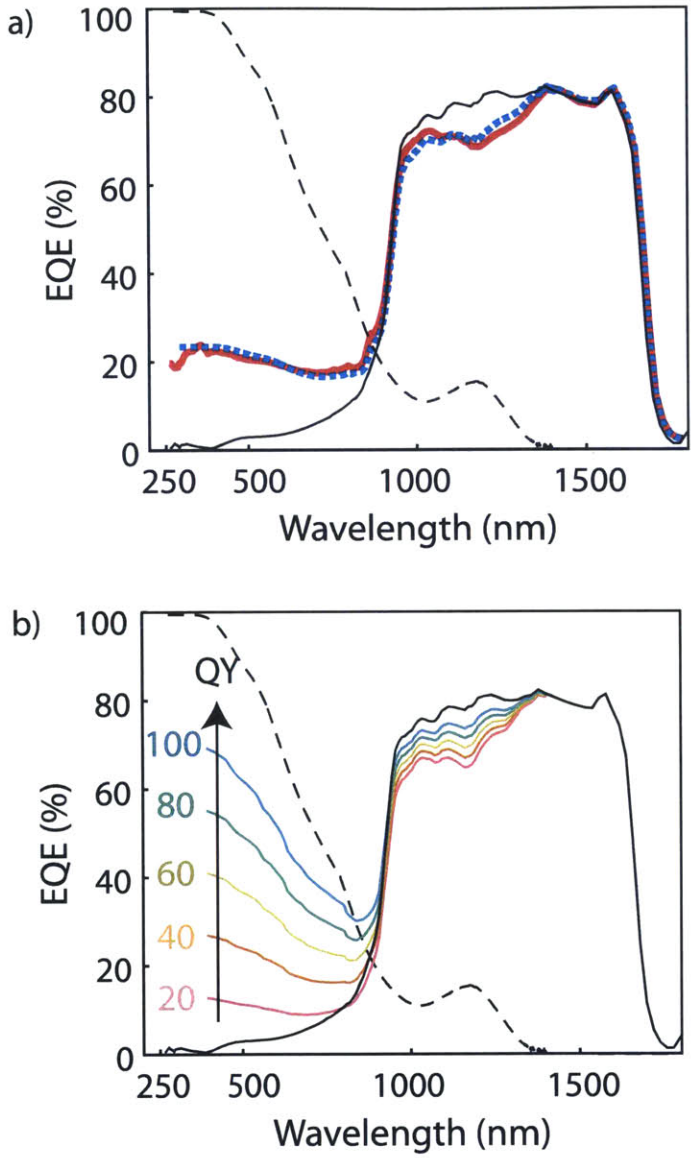

Figure 3.5 Experimental and calculated EQE curves of bare and QD-enhanced InGaAs detectors a)The UV and visible EQE of a bare InGaAs single pixel detector (black solid line) is enhanced by application of a PbS-polymer LDS film with the absorbance shown by the black dashed line. The resulting measured EQE is shown in red which fits well to a modeled efficiency provided a QY of 45% and CE of 62%. No reduction in EQE is apparent in regions beyond the absorbance of the LDS film. b)The expected EQE for detectors enhanced with higher QY LDS films can be estimated. Predicted EQE are shown as a function of increasing QY with an assumed ideal CE of 87%. The reduction in efficiency observed from 800-1400 nm is a result of LDS layer absorption and downshifting at a non-unity efficiency.

interfacial reflection. Addressing these options is challenging in the present day given the absence of suitable high index matrices. Instead, the field has initiatives to increase IR QD QYs by improving the current materials and exploring novel materials sets [18-20].

3.2.2.2 Low temperature performance

Although significant developments are needed to improve the intrinsic room temperature QY of IR QDs, a currently accessible method to increase luminescence is cooling. Figure 3.6 shows the PL increase of a PbS-PVBcoPVAcoPVAc QD-polymer film as the temperature is reduced from room temperature to 80 K. A 2.5-fold increase in the integrated PL in addition to a red-shift and peak narrowing are observed. These effects have been attributed to freezing out phonon-mediated non-radiative recombination pathways [21, 22].

Applying this increase in QY to the EQE model, an UV efficiency of up to 57% can be obtained at 80 K (figure 3.7). As many infrared detectors require cooling to reach peak performance, the LDS layer cooling is an unobtrusive means to bolster downshifting efficiency. As the InGaAs detector used in the previous LDS demonstrations was not rated for low temperature performance, a proof-of-principle was demonstrated on a germanium detector[1].

Figure 3.8a shows the measured bare room temperature Ge and 80 K Ge EQEs in addition to the absorption and emission spectra of the dots employed. The LDS detector EQEs are shown in figure 3.8b. Due to the lower bare detector efficiencies of the Ge detector at the wavelength of QD emission, the

[1] It should be noted that many InGaAs detectors are produced to function at low temperature, but the single-element detectors used in this study were fabricated on substrates that contract at reduced temperatures resulting in broken electrical connections. Experiments were attempted at low temperatures, but as expected, the InGaAs devices failed.

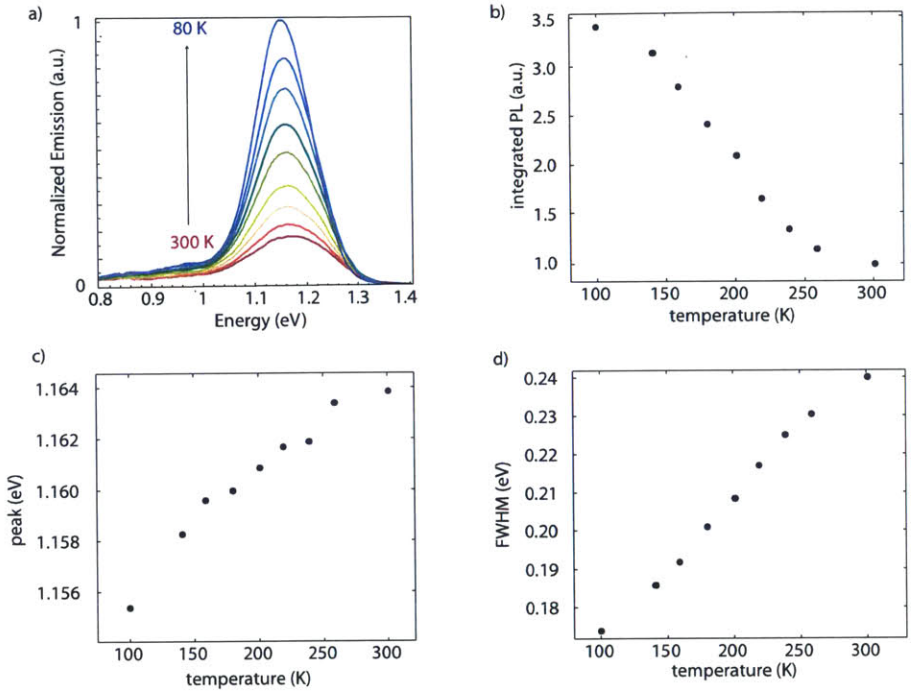

Figure 3.6 Temperature dependent PL characteristics of PbS QD-polymer films a) The temperature dependent PL spectra of a PbS-polymer film, showing a 2.5-fold increase in integrated PL (b) in addition to a subtle red-shift (c) and peak narrowing (d).

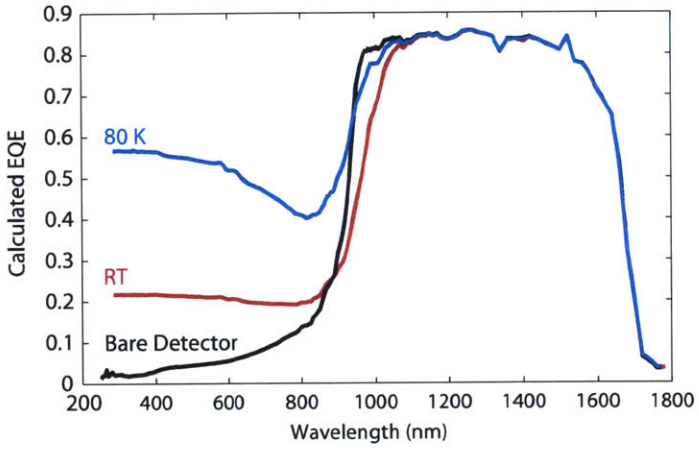

Figure 3.7 Calculated low temperature enhancement of QD LDS InGaAs detectors. The calculated improvement in LDS detector efficiency at room temperature (red) and 80 K (blue) is compared to the measured bare detector EQE (black). The bare detector is expected to experience a blue-shift upon cooling but this effect was negated for simplicity. A nearly three-fold increase in EQE is anticipated at liquid nitrogen temperatures.

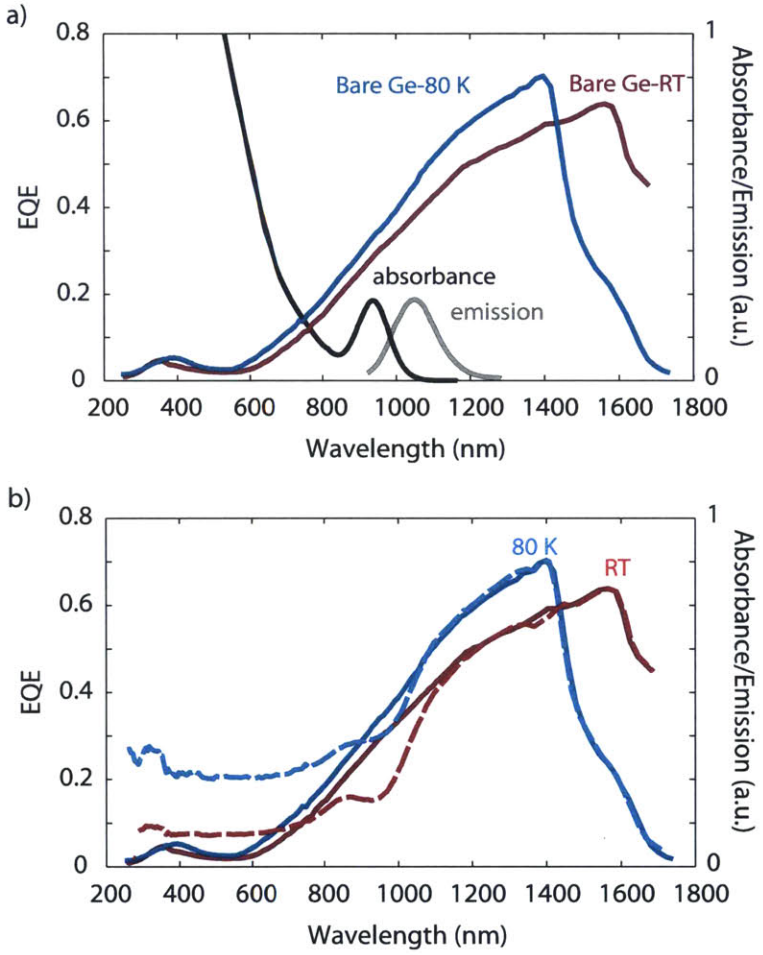

Figure 3.8 Measured low temperature enhancement of QD LDS Ge detectors a) The room temperature (red) and low temperature (blue) EQE of a Ge detector are compared to the absorbance (black) and emission (grey) of a QD LDS layer. b) The measured RT (blue) and low temperature (red) EQEs are shown of both bare (solid line) detectors and their LDS enhanced counterparts (dashed)

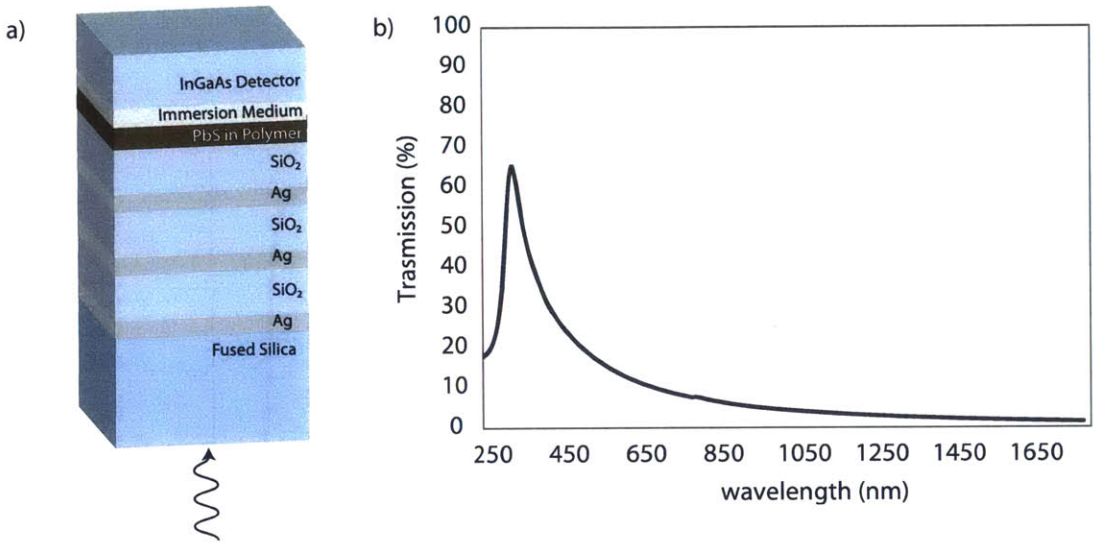

Figure 3.9 UV transmissive filter design a) A dielectric-metal stack band pass filter was designed to efficiently transmit UV and reflect IR light. The resulting transmission spectra is shown in b).

overall enhancement was less than what would be expected for the higher performance InGaAs detector. Although the room temperature QD-enhanced detector exhibits an efficiency of less than 10% in the UV, cooling increases this value to over 20%. Fits to these data suggest an 2.5-fold increase in QY from RT to 80 K, which is consistent with the low temperature increase in integrated PL.

3.2.3 Filter design for isolated UV sensitivity of LDS detector

Many applications that utilize a broad spectral region require the ability to select specific wavelength ranges with dispersive optics or filters. It is particularly challenging to create high quality band pass filters in the UV. In collaboration with the Kimerling group at MIT, a metal-dielectric based UV band pass filter was designed to be coupled to the UV-SWIR downshifting detector [23]. The filter, which consisted of alternating layers of silicon dioxide and silver, is

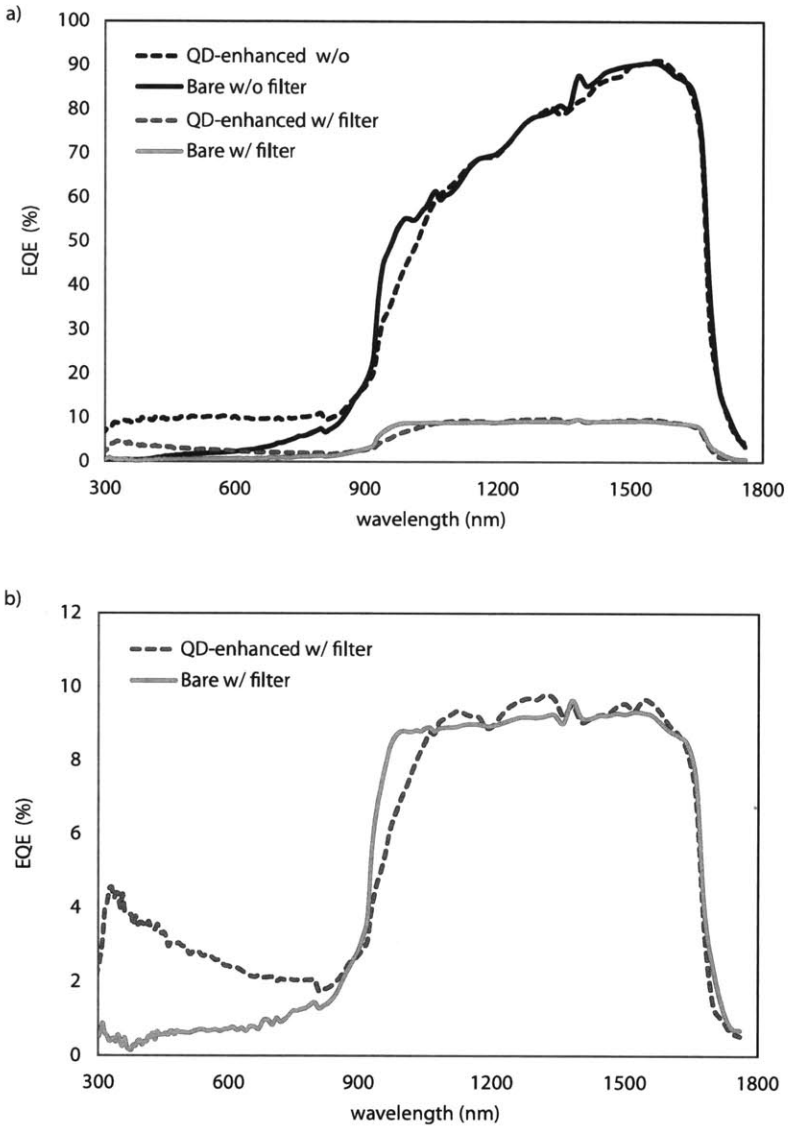

Figure 3.10 Resulting EQE with UV-filter a) The EQE of a bare InGaAs (solid) and LDS enhanced InGaAs (dashed) are shown with (black) and without (gray) a UV band pass filter. The filtered spectra are expanded in b) to better show detail.

illustrated in figure 3.9a and its transmission shown in b. This filter was designed to transmit primarily UV light and efficiently reflect IR light. Ideally this would help improve the film's collection efficiency by preventing the escape of QD emission away from the detector.

The feasibility of integrating this filter with the near-UV-SWIR LDS detector was explored. The response of an InGaAs detector was measured with and without the filter, followed by the same measurements with PbS-polymer LDS layers (figure 3.10). Immersion oil was used in order to facilitate optical coupling between the filter and detector.

Although the filter substantially reduced the detector's SWIR responsivity, it was not sufficient to enable the UV sensitivity to dominate the signal. However, differential detection, where the filtered bare detector signal is subtracted from the filtered QD-enhanced detector, can aid in distinguishing UV signal from SWIR.

3.2.4 Imaging demonstration

Luminescent downshifting can be implemented on a focal plane array (FPA) for broadband imaging. In collaboration with Raytheon Vision Systems, two methods of implementation were demonstrated with passive and active UV illumination. Similar to the single-element LDS detectors previously discussed, QDs can be directly deposited onto a FPA. Alternatively, a scene can be imaged onto a QD LDS film and the resulting emission can be relay imaged to a camera (figure 3.11).

Each implementation suffers from strengths and weaknesses. While direct deposition benefits from maximized downshifted light collection, it requires a

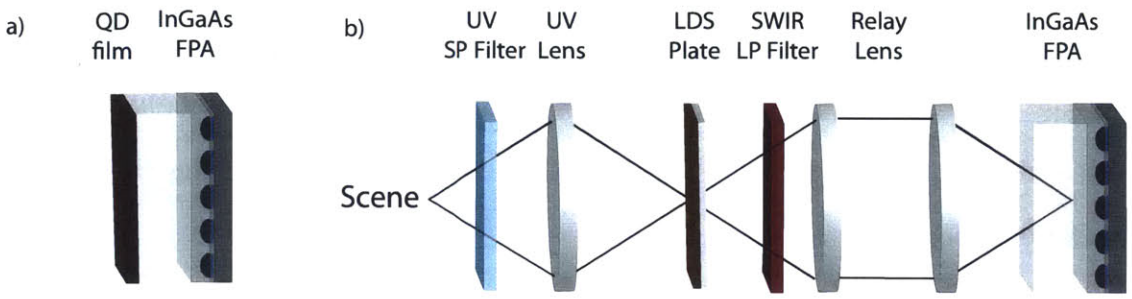

Figure 3.11 Downshifting schemes for camera integration. Scheme (a) shows the direct deposition of QDs on the FPA and scheme (b) depicts a multiple lens relay system. While design (a) suffers from fewer Fresnel loses than (b), it requires a permanent modification of the detector whereas (b) allows for modularity.

semi-permanent modification to the detector. Alternatively, imaging through a QD film allows for greater modularity, but it also results in a loss of efficiency due to multiple index-mismatched interfaces and scatter losses due to the finite aperture of the relay imaging system.

To demonstrate the range of possible applications, images were taken using both of these designs in a variety of environments. For instance, applications can require active or passive illumination. Figure 3.12a shows the lower half of a face that has been actively illuminated by a UV flood light as imaged by a QD-LDS InGaAs FPA. The camera was equipped with a short pass filter to isolate UV light from background signal. In this example, the QD-LDS layer was deposited directly on to the InGaAs FPA. Given the fragility of the gold bonds to the FPA, drop casting was the most prudent method of integration; however, the resulting film inhomogeneity is manifested as artifacts in the image.

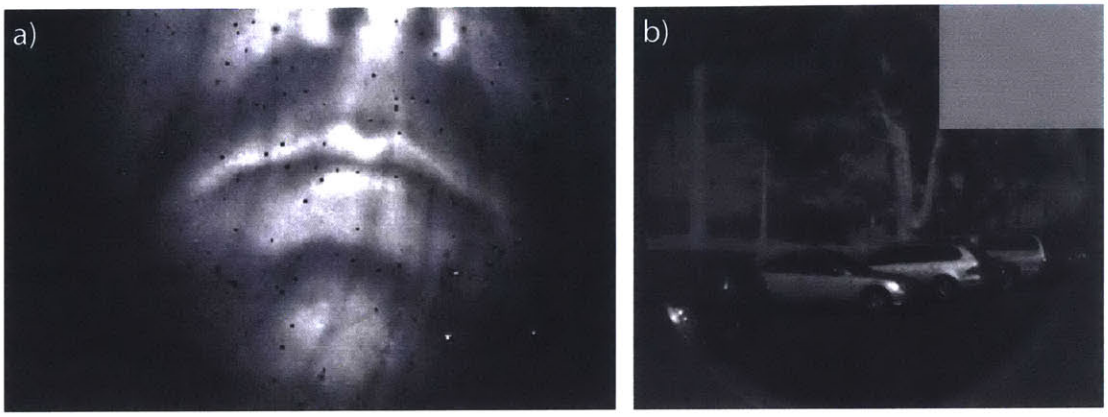

Figure 3.12 Examples of imaging with different LDS schemes a) Active illumination of the lower half of a subject's face as detected by a LDS InGaAs detector. The PbS-polymer film was directly casted onto the FPA. b) Passive solar UV illumination as imaged onto a LDS film and relayed to an InGaAs detector. The imaging array was equipped with a short pass filter to block infrared light.

Figure 3.12b illustrates an example of passive solar UV illumination as imaged through a LDS plate. Again, the imaging array was equipped with a short-pass filter to ensure only UV light was imaged. The image shows remarkable contrast and detail.

While the previous two imaging demonstrations blocked the IR light, simultaneous acquisition of UV and IR scenes is possible provided chromatic aberration is addressed. Chromatic aberration is the process by which an optic's wavelength dependent refractive index results in misaligned focal lengths for different wavelengths (figure 3.13a-b). While generally not a significant issue for narrow wavelength ranges, chromatic aberrations prevent the simultaneous focusing of a broadband image. For example, figure 3.13c shows an IR-illuminated scene which also contains an UV lamp. When the IR light is in

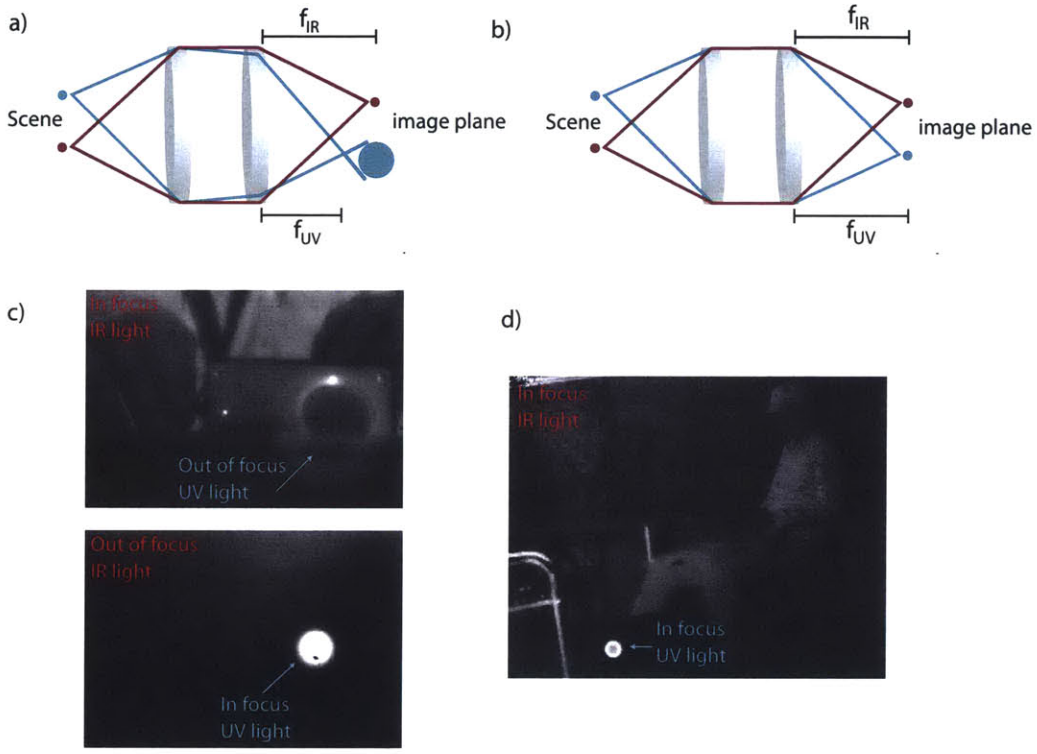

Figure 3.13 a) Chromatic aberration of SWIR optics prevents the simultaneous focusing of SWIR and UV light. b) Special optics can be used to minimize aberrations for the desired wavelength region. c) A image illuminated by SWIR light also depicts a UV light. While the IR illuminated scene is in focus, the UV light is not (top). The UV light can be brought into focus at the expense of defocusing the SWIR scene (bottom). d) With a special objective, both the SWIR and the UV can be simultaneously nearly in-focus.

focus, the UV lamp appears significantly larger than its actual size, and when the UV light in focus, the IR scene is obscured.

Special achromats are designed to mitigate chromatic aberrations. Figure 3.13d shows an image taken through an achromatic objective. Here again the scene is illuminated with IR light and also contains a small UV diode. Now both scenes can simultaneously achieve reasonable focus.

Rather than using achromats, the focus can be shifted between IR and UV and the resulting images convolved. While for some applications this approach is overly cumbersome it provides the added benefit of identifying the approximate wavelength range based on the ability to focus. Additionally, reflective optics can be utilized for achromatic light management, though these typically result in bulkier systems and further consideration of spatial aberrations is required.

3.2.5 Bandwidth determination

The maximum data transfer rate of a detector is given by its frequency bandwidth, generally defined as the point at which the frequency response falls by -3 dB (or 1/2) of its initial value. While SWIR photons are transmitted through a downshifting film and measured at the bare detector's bandwidth, the delay between photon absorption and emission in the QD film can result in a reduced UV-visible bandwidth.

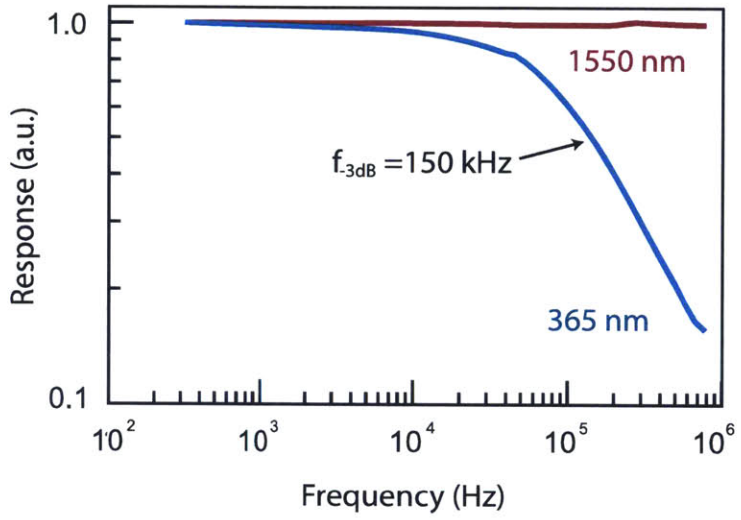

Figure 3.14 Bandwidth measurement of LDS detector. The frequency response of a QD-enhanced SWIR detector is shown at a downshifting UV wavelength (365 nm) and unaffected SWIR (1550 nm) wavelength. The downshifted UV portion exhibits a -3 dB bandwidth of 150 kHz. The SWIR response continues above the frequency limitations of the experimental setup, which is consistent with the expected response of the bare detector rated at 35 MHz bandwidth.

By modulating the frequency of a 1550 nm and a 365 nm light source and measuring the QD-enhanced detector's response, the bandwidth of the LDS-detector resulting from transmitted and downshifted light can be measured. Figure 3.14 shows the resulting response versus frequency. The UV data shows a roll-off at a bandwidth of 150 kHz. Although the bandwidth of the instrumentation utilized was too low to measure the bandwidth of the SWIR response, it is expected to match the underlying InGaAs detector rated at 35 MHz.

As the delay between QD absorption and emission dictates the bandwidth, the measured bandwidth can be corroborated by PL lifetime measurements as was derived in section 2.7. The PL lifetime for a PbS-PMMA film is shown in figure 3.15 and has been fit to a monoexponential lifetime of 1.1 μs. From the relationship between the characteristic monoexponential lifetime of a system and its bandwidth is given by equation 2.13, the bandwidth is calculated to be 144 kHz. This is in good agreement with the measured 150 kHz UV value.

3.3 Conclusions and future scope

The development of a broadband near-UV-to-SWIR detector has been thoroughly characterized and utilized for imaging. Near-UV efficiencies up to 21% have been demonstrated at room temperature and are expected to increase

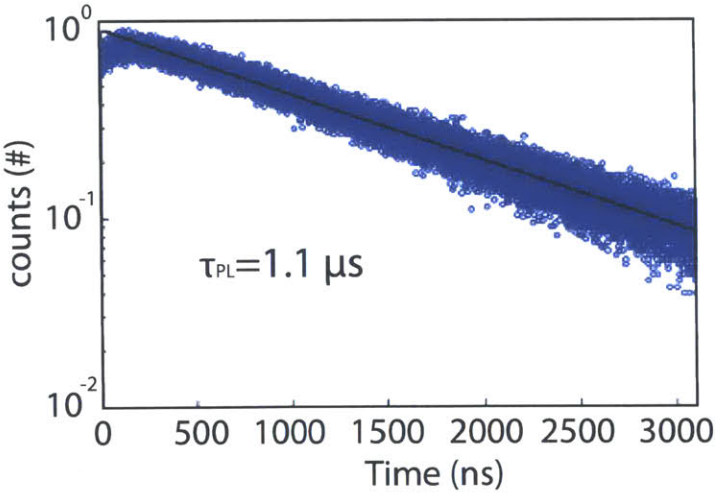

Figure 3.15 The measured PL lifetime of a PbS-PMMA film. A monoexponential fit provides a 1.1 μs lifetime which can be used to calculate an expected bandwidth of 144 kHz.

to up to 58% when cooled to liquid nitrogen temperatures. The relatively nascent field of infrared emitting QDs continues to develop, providing the promise for even higher QYs and consequently higher efficiency downshifting devices. Alternative matrices, which will be discussed in further detail in Chapters 4 and 5, are also being explored, allowing for the potential to extend downshifting capabilities into the mid- and far-UV. Other classes of QDs, such as InAs, which exhibit shorter lifetimes on the order of nanoseconds could be utilized to increase detector bandwidths and increase the versatility of resulting devices.

3.4 Experimental details

Detailed here are experimental techniques unique to this chapter. Please note that experimental information regarding quantum yield, external quantum efficiency, and bandwidth considerations can be found in Chapter 2.

3.4.1. PbS synthesis

PbS cores were prepared via a modified large scale version of the Hines method [24]. An example synthesis is described here. To a three-neck bottom round bottom flask, lead acetate trihydrate (11.38 g, 30 mmol), octadecene (125 ml, 390 mmol), and oleic acid (175 ml, 554 mmol) were added and degassed under vacuum for 12 hours at 100 °C. The solution is placed under nitrogen and the temperature increased to 150 °C at which point a solution of hexamethyldisilathiane in ODE (15 mM, 100 ml) is rapidly injected with a pneumatic gun to promote particle nucleation while the solution is vigorously stirred. The heat source is removed and the solution is allowed to cool to 60 °C

at which point it is cannula transferred to an evacuated flask and pumped into a nitrogen glovebox for purification. The particles are crashed three times with butanol and redispersed in chlorobenzene before use. The synthesis of other sizes was achieved by tuning the octadecene:oleic acid ratio, the injection temperature, and/or the growth time.

3.4.2. Cation exchange shell growth

Cadmium sulfide (CdS) shell growth via cation exchange is performed using a modified Pietryga preparation [25]. In a dry nitrogen glovebox, previously prepared cadmium oleate (0.1 ml, 0.2 M in oleic acid) is added to a solution of PbS in toluene (1 ml, 25-50 mg/ml). The solution is stirred vigorously and heated to 50-80 °C. Cation exchange between cadmium and lead atoms occurs resulting in a thin CdS shell.

3.4.3. Film deposition

The desired polymer is dissolved in chlorobenzene or tetrahydrofuran at a 6-8% by weight percentage via sonication. Equal parts of a 100-150 mg/ml QD sample in the same solvent and the polymer solution are mixed prior to film deposition. When applicable, spin coating at 1000-2500 rpm was utilized to improve film uniformity. As this was unfeasibly on detector surfaces, drop casting was performed. An approximate 6% loading fraction of QDs, was calculated for detector examples [26]. The loading fraction was optimized such that the highest absorbance was obtained without compromising film QY. The films were not packaged to allow for reusability of the photodetector. The initial

QY of PbS solution in chlorobenzene was found to be 55%, which dropped to 45% in film.

3.4.4. Materials characterization

Absorbance spectra were measured with a Cary 5000 and emission spectra were measured with a home-built spectrometer equipped with a Roper Instruments InGaAs array detector and an 532 nm diode excitation source.

3.5 Chapter-specific acknowledgements

Portions of the data presented here were collected in collaboration with Scott Geyer. Frank Jaworski of Raytheon Vision Systems was central to the imaging demonstrations. Michael Jack was involved in fruitful discussions. Raoul Correa provided assistance with photoluminescent lifetime measurements. Anu Agarwal, Jianwei Mu and Pao-Tai Lin developed the UV band pass filter and thoughtfully contributed to discussions.

3.6 References

[1] G. Ariyawansa, P. V. V. Jayaweera, A. G. U. Perera, S. G. Matsik, M. Buchanan, Z. R. Wasilewski and H. C. Liu. "Normal incidence detection of ultraviolet, visible, and mid-infrared radiation in a single GaAs/AlGaAs device." *Opt. Lett.*, **34**, 2036 (2009).

[2] G. Ariyawansa, M. B. M. Rinzan, M. Alevli, M. Strassburg, N. Dietz, A. G. U. Perera, S. G. Matsik, A. Asghar, I. T. Ferguson, H. Luo, A. Bezinger and H. C. Liu. "GaN/AlGaN ultraviolet/infrared dual-band detector." *Applied Physics Letters*, **89**, 091113 (2006).

[3] Q. He, Z. Xu and B. M. Sadler. "Performance of short-range non-line-of-sight LED-based ultraviolet communication receivers." *Opt. Express*, **18**, 12226 (2010).

[4] M. P. Hansen and D. S. Malchow. "Overview of SWIR detectors, cameras, and applications." *Proc. SPIE 6939, Thermosense XXX, 69390I* (2008).

[5] C. Elachi, J. J. van Zyl. **Introduction to the Physics and Techniques of Remote Sensing.** Wiley (2006).

[6] C. Fischer and I. Kakoulli. "Multispectral and hyperspectral imaging technologies in conservation: current research and potential applications." *Studies in Conservation*, **51**, 3 (2006).

[7] M. D. King, Y. J. Kaufman, W. P. Menzel and D. Tanre. "Remote sensing of cloud, aerosol, and water vapor properties from the moderate resolution imaging spectrometer (MODIS)." *IEEE Transactions on Geoscience and Remote Sensing*, **30**, 2 (1992).

[8] C. O. Justice, J. D. Kendall, P. R. Dowty and R. J. Scholes. "Satellite remote sensing of fires during the SAFARI campaign using NOAA Advanced Very High Resolution Radiometer data." *Journal of Geophysical Research: Atmospheres*, **101**, 23851 (1996).

[9] J. K. Delaney, M. Thoury, J. G. Zeibel, P. Ricciardi, K. M. Morales and K. A. Dooley. "Visible and infrared imaging spectroscopy of paintings and improved reflectography." *Heritage Science*, **4**, 1 (2016).

[10] M. Elias and P. Cotte. "Multispectral camera and radiative transfer equation used to depict Leonardo's sfumato in Mona Lisa." *Appl. Opt.*, **47**, 2146 (2008).

[11] L. J. Hoenig. "Dermatology in the artwork of leonardo da vinci." *JAMA Dermatology*, **149**, 73 (2013).

[12] T. Slonecker, G. B. Fisher, D. P. Aiello and B. Haack. "Visible and Infrared Remote Imaging of Hazardous Waste: A Review." *Remote Sensing*, **2**, 2474 (2010).

[13] S. Singh. "Sensors—An effective approach for the detection of explosives." *Journal of Hazardous Materials*, **144**, 15 (2007).

[14] T. Dubroca, G. Brown and R. E. Hummel. "Detection of explosives by differential hyperspectral imaging." *OPTICE*, **53**, 021112 (2014).

[15] C. Adams, R. Carabott and S. Evans. **Forensic Odontology: An Essential Guide**. Wiley (2013).

[16] I. Medintz and N. Hildebrandt. **FRET - Förster Resonance Energy Transfer: From Theory to Applications**. Wiley (2013).

[17] R. Ihly, J. Tolentino, Y. Liu, M. Gibbs and M. Law. "The Photothermal Stability of PbS Quantum Dot Solids." *ACS Nano*, **5**, 8175 (2011).

[18] S.-W. Kim, J. P. Zimmer, S. Ohnishi, J. B. Tracy, J. V. Frangioni and M. G. Bawendi. "Engineering InAsxP1-x/InP/ZnSe III−V Alloyed Core/Shell Quantum Dots for the Near-Infrared." *Journal of the American Chemical Society*, **127**, 10526 (2005).

[19] D. K. Harris, P. M. Allen, H.-S. Han, B. J. Walker, J. Lee and M. G. Bawendi. "Synthesis of Cadmium Arsenide Quantum Dots Luminescent in the Infrared." *Journal of the American Chemical Society*, **133**, 4676 (2011).

[20] Y. Gao and X. Peng. "Photogenerated Excitons in Plain Core CdSe Nanocrystals with Unity Radiative Decay in Single Channel: The Effects of Surface and Ligands." *Journal of the American Chemical Society*, **137**, 4230 (2015).

[21] M. S. Gaponenko, A. A. Lutich, N. A. Tolstik, A. A. Onushchenko, A. M. Malyarevich, E. P. Petrov and K. V. Yumashev. "Temperature-dependent photoluminescence of PbS quantum dots in glass: Evidence of exciton state splitting and carrier trapping." *Physical Review B*, **82**, 125320 (2010).

[22] M. S. Gaponenko, N. A. Tolstik, A. A. Lutich, A. A. Onushchenko and K. V. Yumashev. "Temperature-dependent photoluminescence Stokes shift in PbS quantum dots." *Physica E: Low-dimensional Systems and Nanostructures*, **53**, 63 (2013).

[23] J. Mu, P.-T. Lin, L. Zhang, J. Michel, L. C. Kimerling, F. Jaworski and A. Agarwal. "Design and fabrication of a high transmissivity metal-dielectric ultraviolet band-pass filter." *Applied Physics Letters*, **102**, 213105 (2013).

[24] M. A. Hines and G. D. Scholes. "Colloidal PbS Nanocrystals with Size-Tunable Near-Infrared Emission: Observation of Post-Synthesis Self-

Narrowing of the Particle Size Distribution." *Advanced Materials.* **15** 1844 (2003).

[25] J. M. Pietryga, D. J. Werder, D. J. Williams, J. L. Casson, R. D. Schaller, V. I. Klimov and J. A. Hollingsworth. "Utilizing the Lability of Lead Selenide to Produce Heterostructured Nanocrystals with Bright, Stable Infrared Emission." *Journal of the American Chemical Society*, **130**, 4879 (2008).

[26] S. M. Geyer, J. M. Scherer, N. Moloto, F. B. Jaworski and M. G. Bawendi. "Efficient Luminescent Down-Shifting Detectors Based on Colloidal Quantum Dots for Dual-Band Detection Applications." *ACS Nano*, **5**, 5566 (2011).

Chapter 4

Far- and Mid-UV Detector Sensitization for UV and Broadband Detection and Imaging via Luminescent Downshifting

4.1 Introduction

Despite a growing field of applications currently supported by UV and UV-visible broadband detection (including cosmic spectroscopy and imaging, short-range communications, and forensic analysis) UV and UV-visible detectors are far less advanced than their visible counterparts [1-6]. This chapter will discuss a means to extend the sensitive region of a visible detector to shorter wavelengths via luminescent downshifting (LDS). Thick-shelled cadmium selenide/cadmium sulfide (CdSe/CdS) QDs are particularly well suited for this wavelength region. They allow for passive, robust, and reversible extension of the

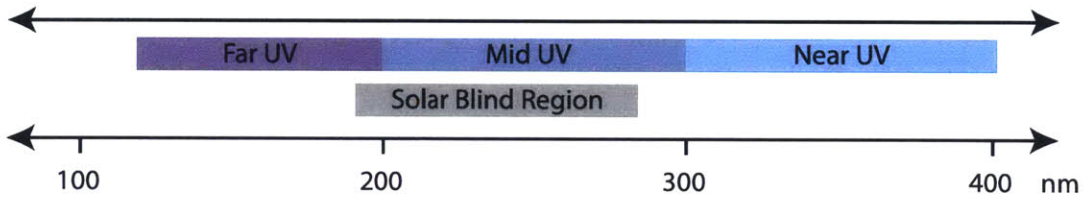

Figure 4.1 UV spectral region designations for this text include the following: near-UV (300-400 nm), mid-UV (200-300 nm), far-UV (122-200 nm) and the solar blind region (190-280 nm).

quantum efficiency of visible detectors into the mid- and far-UV. The LDS resulting detectors can be utilized for broadband UV-visible applications or UV detection when equipped with suitable optical filters.

4.1.1 Definitions of UV spectral regions

The International Organization for Standardization has provided multiple designations for the various spectral regions of UV. This text will utilize the near- (300-400 nm), mid- (200-300 nm) and far-UV (122-200 nm) nomenclature as shown in figure 4.1. In addition, the solar blind UV region (SBUV, 190-280 nm) is of interest due to specific applications where atmospheric filtering of the solar spectrum can be exploited. For terrestrial measurements, the solar blind region is void of light from the sun due to the strong ozone absorption starting at 280 nm [7]. The high energy bound at ~190 nm is dictated by the onset of a strong oxygen absorbance band. Because this unique range provides a low natural background, it can be inferred that detected light in this region has originated from a manmade source.

A number of applications exploit the unique characteristics of these UV regions. UV light exhibits high scattering efficiency and distinct material signatures can be found in the UV spectral range [2, 3, 8]. In this chapter a few of the most common and relevant UV detection and imaging applications will be discussed.

4.1.2 Applications of UV and UV-visible detectors

4.1.2.1 Forensics and biomedical imaging

One of the earliest commercial implementations of UV imaging has been in the field of forensics analysis. Some forensic techniques take advantage of a material's unique UV reflective, absorptive and emissive properties for identification and location. For instance, most biomolecules strongly absorb UV light whereas inorganic materials like stone or some types of paint are more reflective in the UV, providing a means for imaging contrast [2]. UV-imaging has been used for a variety of applications including the analysis and identification of latent bruises, bite marks, fingerprints, shoe prints, trace explosives identification and surface textural changes [3].

Despite the wealth of information provided by UV imaging, forensic departments are not always equipped with suitable devices due to budget constraints. The LDS scheme presented below would allow for the creation of a UV camera through a simple, unobtrusive, low-cost modification to an existing visible camera. As will be demonstrated, even a smart phone camera can be modified to sense the UV with a compact attachment.

4.1.2.2 Cosmic spectroscopy

A primary driving force for the development of high-quality UV detectors and cameras has been space-based astronomy, owing to UV light's high scattering efficiency and the thermal signature of high-temperature blackbody radiators. From this information a celestial body's development and demise can be monitored [9]. The improvement of UV detector quality is consequently a continued research endeavor for space agencies.

The former Hubble Space Telescope camera, the Wide Field and Planetary Camera 2 (WFPC2), was equipped with a LDS-based UV-visible detector [6]. While the degraded WFPC2 was retired in 2009, it showcases the potential benefit of a downshifting detector for extreme environments and highlights the promise of utilizing QDs as a LDS medium, which are likely more stable than other LDS materials.

4.1.2.3 Defense and military applications

Numerous defense applications utilize UV and IR detection capability. One particular application of note is SBUV short-range optical communication [4, 5]. Traditionally, infrared light has been widely utilized for long-range optical communication due to its high atmospheric transmission. While the efficient scattering of UV light prevents long-range communication, its rapid atmospheric attenuation and high scattering efficiency is exploited for short-range non-line-of-sight communications (NLOS). Unlike IR communication, which requires the transmitter and receiver be in the same line-of-sight (LOS), the efficient scattering of UV light allows for an offset between the two devices (figure 4.2).

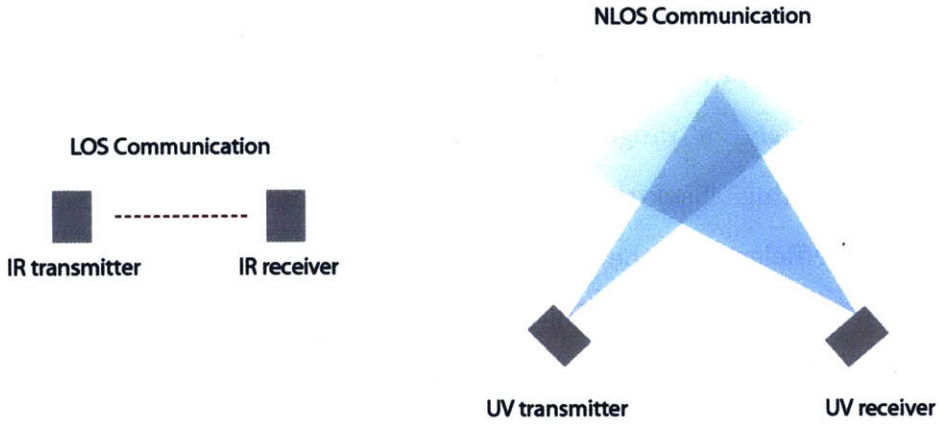

Figure 4.2. Line-of-sight (LOS) vs non-line-of-sight (NLOS) communication. While the low atmospheric transmission of IR light allows for long-range optical LOS communication, the highly efficient UV atmospheric scattering allows for NLOS communication which can be collected at an angle from the transmitted signal.

Obstructing objects, such as buildings or vehicles that can prevent transmission of LOS signals, pose less of a challenge for NLOS schemes, making them particularly well suited for urban implementation. Similarly, while the single path of LOS communications can be jammed, it is far more challenging to block the cone of light created with NLOS communication. Additionally, the use of the SBUV region requires lower transmitter signal intensity to differentiate the transmitted light from background noise.

4.1.3 Current UV detection technologies and limitations

Most commonly utilized UV and UV-visible detectors fall into some class of photocathodes or enhanced silicon detectors and they suffer from multiple shortcomings [10]. While UV photocathode detectors such as Cs-Te and GaN achieve typical mid-UV quantum efficiencies of around 10-20%, they suffer from

mechanical fragility. Further hindering their employment, photocathodes often require coupling to a high voltage microchannel plate for signal amplification, increasing size, weight, and power consumption.

Alternatively, a range of methods have been used to improve silicon detectors including back-thinning and delta doping. While back-thinning improves the efficiency in the UV, it often comes at the cost of sensitivity in the visible [11]. Delta-doping, the inclusion of a very thin layer of highly doped material usually at the semiconductor's surface, results in a near unity internal quantum efficiency for the far-UV through visible [12]. Although technologically promising, both of these modifications come with increased production complexity and at a cost which can be prohibitively high for many applications.

The demand for alternatives in high quality UV detection has spurred research in wide-band gap detectors. Among the most promising class are group-III nitrides. Specifically, the solid solution series of $Al_xGa_{1-x}N$ has shown potential as solar-blind UV detectors [13]. Although research grade detectors show quantum efficiencies of up over 40% in the SBUV, there are significant challenges in the scaled growth of high quality $Al_xGa_{1-x}N$, which is a primary research arm of the SBUV detector development community.

4.1.4 Previous approaches to visible downshifting

Beginning in the 1970's, molecular dyes were utilized as a downshifting material due to the abundance of high QY fluorophores. One of the most notable examples is Lumogen Yellow S, an organic dye whose near-UV absorbance and visible emission was used to extend the sensitive range of silicon CCDs [6]. The

resulting detectors have been sold commercially by various companies and utilized on multiple space expeditions [14]. However, the dye has been shown to possess only moderate UV and vacuum stability, and as dye, can downshift only a limited range of UV light. Nevertheless, its commercial use despite both of these shortcomings serves to highlight the absence of quality UV detectors and the need for alternatives.

A number of research groups have explored downshifting as a means to extend the active wavelength range of a solar cell into the near-UV with QDs in a hydrocarbon polymer [15-17]. Generally, an EQE enhancement of no more than 15% absolute was measured, and due to polymer absorbance, the wavelength extension is limited to the near-UV. Others have also addressed the challenge of mid-through-near-UV downshifting via colloidal QDs with little success. Robinson *et al.* presented their attempt to extend the sensitivity of a CMOS detector with CdSe/ZnS core/shell QDs. Although they developed an aerosolization technique to create high quality neat-QD films, the resulting detector performed significantly worse in the UV, with decreases of up to 60% absolute observed [18].

Only recently have QD developments allowed for both high material quality and optimum film development to create efficient mid-UV-to-visible downshifting with the potential to extend into the far-UV. These attributes are harnessed in the work presented in this chapter to demonstrate the highest UV efficiency enhancements gained via QD downshifting.

4.2 Results and discussion

QDs are well suited to the task of extending the wavelength range of a visible detector due to their high quantum yield, broad absorption, narrow emission, and tunable optical properties. A downshifting QD film also adds marginal size and weight to a preexisting visible detector, which is particularly appealing for pay-load conscious applications such as deployment on soldiers, satellites and unmanned aerial vehicles. In the following sections, the design considerations and characterization of a QD-enhanced silicon detector are discussed.

4.2.1 Choice of downshifting material

In order to achieve a high efficiency downshifting film, four general requirements must be optimized: (1) high absorption cross section and broad absorption range, (2) high quantum yield, (3) high collection efficiency, and (4) emission which overlaps with a detector's sensitive range. Although molecular dyes exhibit high visible QYs at various emission wavelengths, they have a limited absorbance range, limiting the capabilities of wavelength extension via LDS. Additionally, they typically have poor UV stability. A broader spectral region can be captured utilizing a dye-based cascade approach. Here, multiple dyes are chosen such that energy transfer can occur between them and the resulting emission may be designed to align with the detector's sensitive region. However, this technique requires increased complexity and often results in a decreased efficiency [19]. Novel nontoxic materials are emerging, such as carbon dots, however high QYs and optical tunability have yet to be achieved in their development infancy [15].

In contrast, visibly emitting QDs, specifically CdSe/CdS core/shell particles, can address all of the desired traits of a downshifting medium. They exhibit near unity quantum yields, tunable and narrow emission, and have broad absorption and a high absorption cross section allowing them to downshift a wide spectral region. The CdSe/CdS system exhibits many promising LDS attributes; however, further investigation and optimization of integration requirements for a far- or mid-UV-to-visible downshifting medium will be explored in the following sections.

4.2.2 Considerations of QD ligand absorption in the UV

Although QDs show promise as a visible downshifting material, their far- and mid-UV optical properties are predominantly unexplored. To evaluate their applicability as a UV downshifting material, further considerations must be made including the potential influence of ligand absorption. CdSe/CdS QDs are post-synthetically capped with near-UV absorbing oleic acid ligands (figure 4.3a). As it is unlikely that the energy absorbed by these ligands is transferred to the emissive QD core, minimizing their absorption in a QD film is imperative to overall efficiency optimization.

To estimate the ligand contribution to UV absorption, the absorbance of twice-crashed CdSe/CdS QDs was measured in solution (figure 4.3). Two small IR features which align with the 1700-1800 nm oleic acid absorption are observed. The UV oleic acid contribution can be estimated by scaling the oleic acid absorbance to match that of the QD sample in the IR. For this sample, approximately 3% of the absorbance at 250 nm can be attributed to oleic acid. The CdSe/CdS sample used in the downshifting demonstration has been

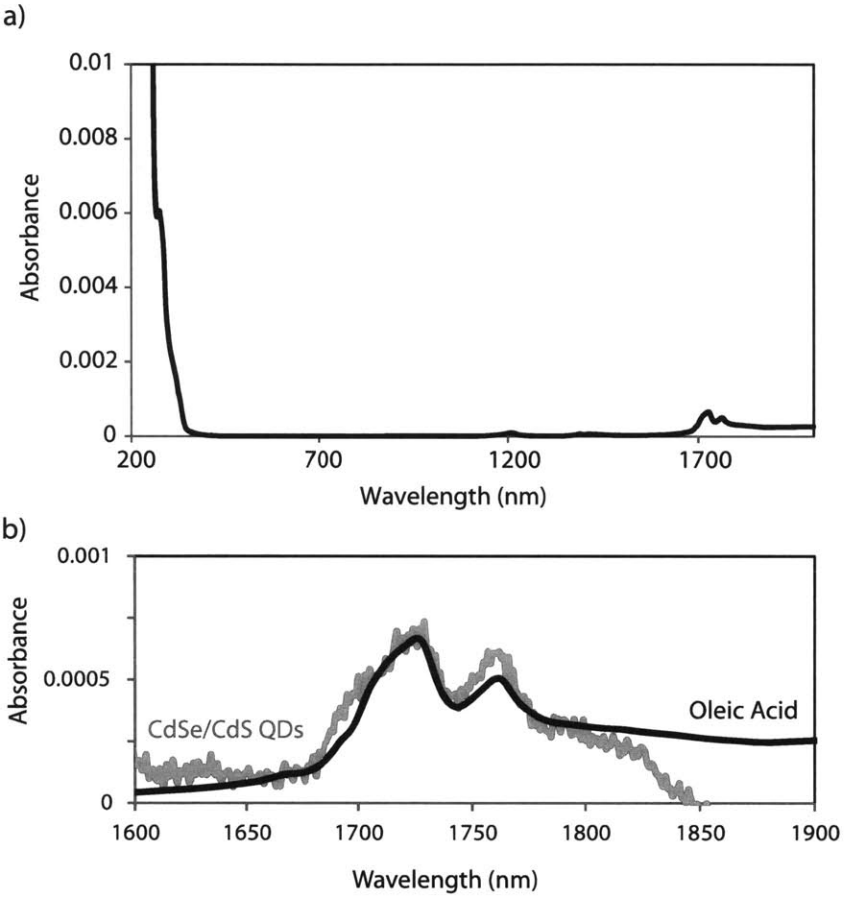

Figure 4.3 Influence of oleic acid ligands on parasitic UV absorption. a) Oleic acid absorbance. b) Scaled oleic acid absorption to trace oleic acid present in CdSe/CdS QD absorbance.

significantly further purified, likely resulting in fewer residual oleic acid molecules and thereby reducing the parasitic UV absorbance.

A simple Beers-Law approximation can be utilized to corroborate this result. Consider a 5 nm diameter CdSe/CdS particle. The surface density of

oleic acid ligands has been measured to be 1.1-4.2 ligands/nm^2 [20]. Taking into account the measured density of oleic acid ligands in films of QDs, the 1.5 nm interparticle distance [21], and assuming a randomly close packed 1 μm thick film, the amount of oleic acid in this film will transmit approximately 99% of 232 nm light [22].

From these approximations, it is unlikely that surface oleic acid will be detrimental to mid- or near-UV downshifting. Higher energy excitation behavior was not measureable due to experimental limitations. If parasitic ligand absorption is encountered, ligand exchange with alternative single atom or inorganic ligands, or thermal removal of ligands may mitigate the effect [23, 24]. For thin-shelled QDs, these approaches could result in a reduced QY; however, as will be discussed in the following section, the use of thick-shelled CdSe/CdS may sufficiently shield the exciton from surface states, allowing for the preservation of a high QY.

4.2.3 Minimization of FRET-induced in-film quantum yield reduction

An important consideration when designing high efficiency QD films is the maximization of their in-film QY. Although the visibly emitting class of CdSe/CdS core/shell QDs displays remarkably high QYs in-solution, placing QDs in close proximity allows for dot-to-dot Forster resonance energy transfer (FRET). FRET increases an exciton's probability of relaxing through a non-radiative decay pathway and consequently reduces the in-film QY. As FRET is dependent on the spatial donor and acceptor distance and the spectral overlap of

the acceptor absorption and donor emission, strategies to reduce FRET rely on tuning these quantities. Further details may be found in section 2.7.

This challenge was addressed in the near-UV-to-SWIR downshifting detailed in chapter 3 by dispersing QDs in a hydrocarbon polymer to increase interparticle spacing. The strong mid- to near-UV absorption onset of hydrocarbon polymers impairs application to mid- and far-UV downshifting. If downshifting from mid- or far-UV wavelengths is desired, either the polymer concentration must be significantly reduced or an alternative approach must be sought.

Suitable alternative matrices for the UV-through-visible are scarce. In addition to being transparent and stable, they must also meet the challenging requirement of effectively dispersing QDs. Three strategies were explored. High band gap salts and fluorinated materials were considered as transparent matrix alternatives and neat films of thick-shelled CdSe/CdS as a means to both physically separate QD cores and to effectively increase the Stokes shift. Each option and their technical challenges will be discussed.

Recent advances from the Eychmuller group have demonstrated the incorporation of CdTe QDs into sodium chloride (NaCl) crystals [25-27]. Not only does the wide 9 eV band gap of NaCl allow for a highly transparent matrix extending into the far-UV, QDs encapsulated by large band gap materials promote exciton localization as the barrier for tunneling is increased. Interestingly, the Eychmuller group also observed an increase in the QD's QY in the NaCl matrix as compared to water or silicone, an effect they attributed to

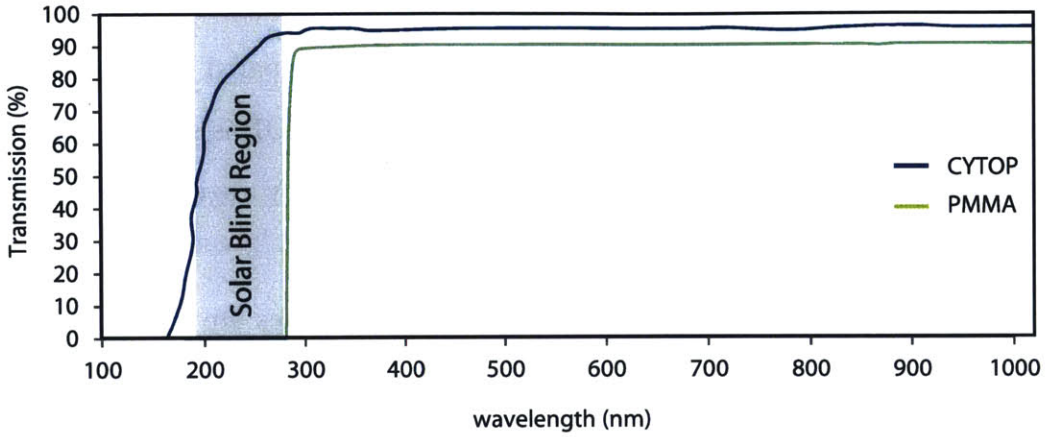

Figure 4.4 Comparison of polymer transmission spectra. Hydrocarbon polymers like PMMA exhibit significant absorbance in the UV region due to electronic transitions. Fluorinated polymers electronic transitions are shifted to higher energies resulting in a more transparent matrix in the UV.

the surface passivating effect of chloride ions. While this discovery is promising for QD downshifting technologies, the process to create QD-doped NaCl crystals requires weeks of slow evaporation and the resulting crystals must be ground and redispersed in a hydrocarbon polymer matrix for incorporation into film architectures. Although strategies to overcome these hurdles are being explored [28], this novel technique is not yet suitable for the production of transparent, low scattering, and scalable downshifting films.

A second class of potential UV-visible transparent matrices is fluorinated polymers. The electronic absorption features of hydrocarbons occur in the mid-UV, but fluorination of these bonds shifts these transitions to higher energies. Consequently, the UV-absorption onset of fluorinated polymers is typically in the mid- or far-UV rather than the near-UV generally seen for hydrocarbons. As an

example, figure 4.4 shows the transmission spectra of ~1 μm thick films of the commonly used poly(methyl methacrylate) (PMMA) compared to the highly fluorinated CYTOP polymer. The absorption onset of CYTOP is shifted roughly 2 eV higher in energy, allowing for an unobstructed mid-UV region particularly attractive for solar blind region applications.

Although fluorinated polymers' spectral characteristics are well suited for this application, they present another challenge: highly fluorinated materials are immiscible with hydrocarbon materials and the miscibility of QDs is dictated by their hydrocarbon ligand shell. QD dispersion into fluorinated polymers can be facilitated by a ligand exchange to sufficiently fluorinated molecules. While attractive in theory, a suitable ligand that can be exchanged in an energetically favorable means and that results in a stable QD can be challenging. Chapter 5 will discuss the use of perfluorotetradecanoic acid with PbS and PbSe QDs, however a suitably stable ligand was not found for the CdSe/CdS system.

As these alternative matrices present significant challenges, an approach to increase the effective QD Stokes shift to reduce dot-to-dot FRET is considered. One means to achieve this is through utilization of thick-shelled CdSe/CdS QDs [29]. For this material, the higher band gap CdS shell constitutes the bulk of the material's volume and is responsible for most of the high energy absorbance. After absorption, the exciton is funneled into the CdSe core where emission occurs, resulting in an effective Stokes shift (figure 4.5). Additionally, the thick shell increases the core-to-core distance, also contributing to FRET reduction (FRET efficiency $\propto 1/r^6$).

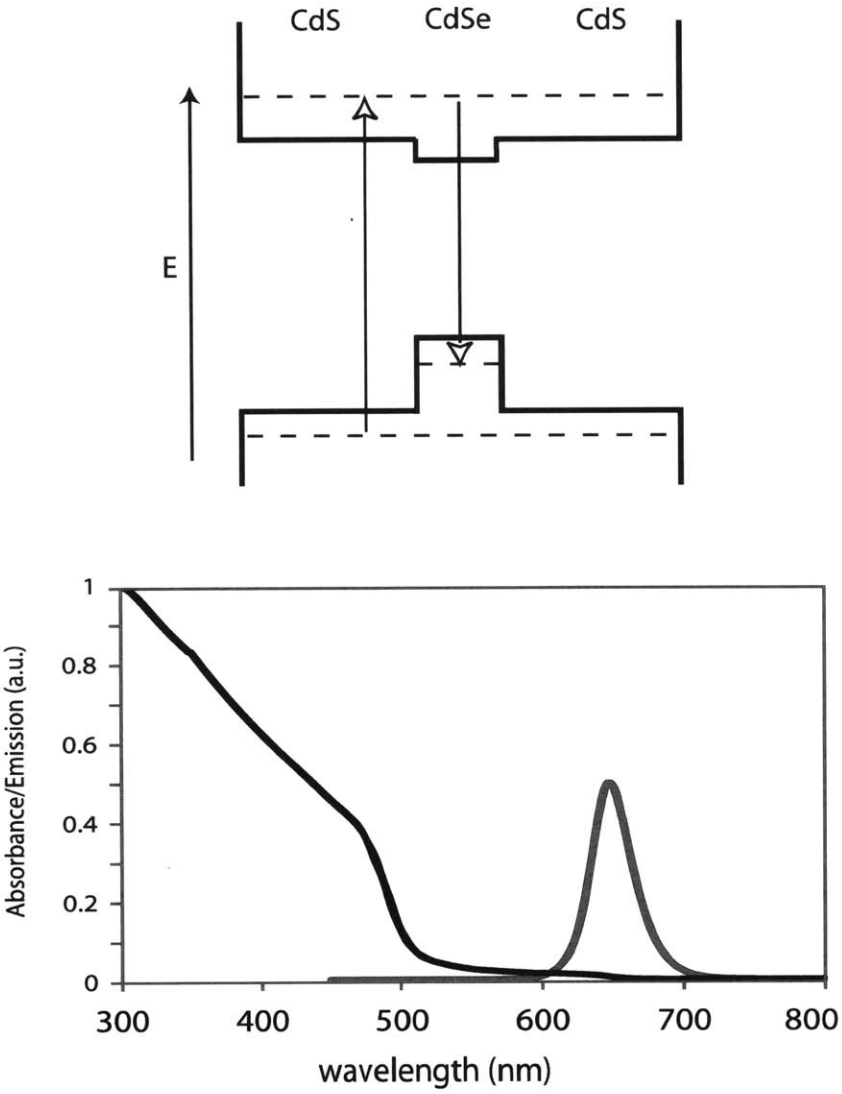

Figure 4.5 Measured absorbance and emission from sample of thick-shelled CdSe/CdS demonstrating large effective Stokes shift.

If FRET is sufficiently minimized, the QY of a QD neat-film should be comparable to its value in solution. Indeed, for the thick-shelled CdSe/CdS utilized in this work, both the in-film and in-solution QYs were measured to be 98%. For comparison, this sample's core-only counterpart exhibited a decrease in QY from 7% in solution to 0.5% in a neat film. Although this robustness partially originates from the initial near unity value, these values demonstrate the significant improvements obtainable through use of thick-shelled samples.

Having considered multiple options for creating a high quality downshifting film, the following work will utilize neat films of thick-shell CdSe/CdS and compare this to CdSe/CdS films in a hydrocarbon polymer.

4.2.4 LDS demonstration with neat CdSe/CdS core/thick-shell film

4.2.4.1. Film absorbance and emission

The emission and absorbance of thick-shelled CdSe/CdS in a neat film and in chlorobenzene are shown in figures 4.6-7. Spectral shifts between film and solution measurements are often observed in QD samples and attributed to interactions between the exciton and its modified dielectric environment [27]. Poorly isolated excitons generally exhibit a greater shift. This is reflected in the in-solution and in-film emission shifts of core-only CdSe and thick-shelled CdSe/CdS (figure 4.6). While the core-only particles shift by 41 meV, the thick-shelled QDs shift by only 6 meV. This result is consistent with a reduced interaction between the exciton and the QD's environment for the thick-shelled particles. A reduction in FRET is consequently expected, corroborating the previously noted robustness of the in-film QY of thick-shelled CdSe/CdS.

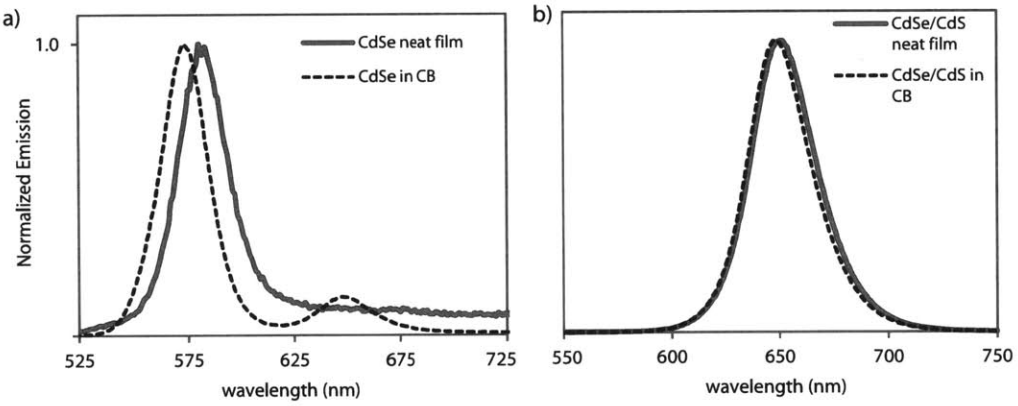

Figure 4.6 Emission change of QDs in-film and in-solution a) Normalized emission from a core-only CdSe QD sample in a neat film and a chlorobenzene solution b) Normalized emission from a thick-shelled CdSe/CdS QD sample in a neat film and a chlorobenzene solution. The observed shift between film and solution is greater for the core-only particles than the core/shell, suggesting a decreased interaction with the environment for core/shell particles.

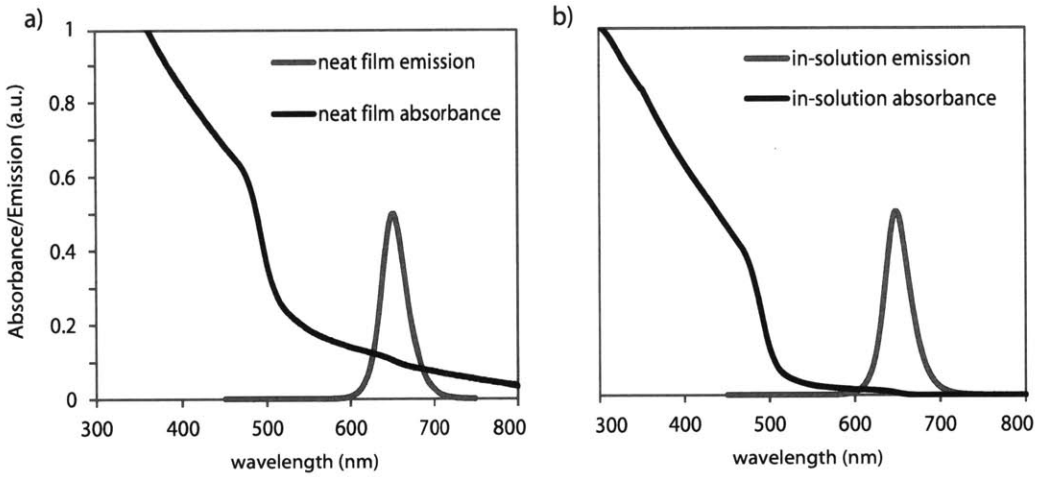

Figure 4.7 Absorbance and emission of thick-shelled CdSe/CdS in a a) neat film and b) chlorobenzene solution

4.2.4.2. Measuring and modeling film scatter

An important feature of the CdSe/CdS neat film absorbance spectra shown in figure 4.7 is the high baseline observed in the film absorption spectrum extending well past the QD band gap. This increased baseline is a most likely a result of scatter from surface structure and is detrimental to the downshifting efficiency of the film.

In order to approximate the degree of scatter, the transmission of a neat film was measured inside and outside of an integrating sphere. The integrating sphere allows for the collection of scattered light, and the difference of these measurements provides an estimation of scatter. It should be noted that in addition to collecting scattered light, the integrating sphere also collects QD emission and allows for more absorption events. Under the reasonable assumptions that the QY is near unity and the efficiency of the detector is relatively flat, the additional absorption negates the emission. A representative scatter measurement is shown in figure 4.8.

A simple model employing the Huygens-Fresnel principle can be constructed to fit this scatter. Light incident a rough film will reflect off of various height features or transmit through a range of thicknesses, resulting in a distribution of phase shifts. Each trough or valley can be modeled as a point emitter with a height specific phase relation to the incident beam which is then used to estimate the far-field light interference [30]. The measured data was fit to the black line shown in figure 4.8 by assuming a Gaussian distribution of surface feature heights with a roughness (R_a) of 15 nm. This roughness accounts for only 1-2 monolayers of the utilized QD. If the surface roughness (average) is reduced to the QD radius of 7 nm, the scatter is reduced by nearly 85% at 150

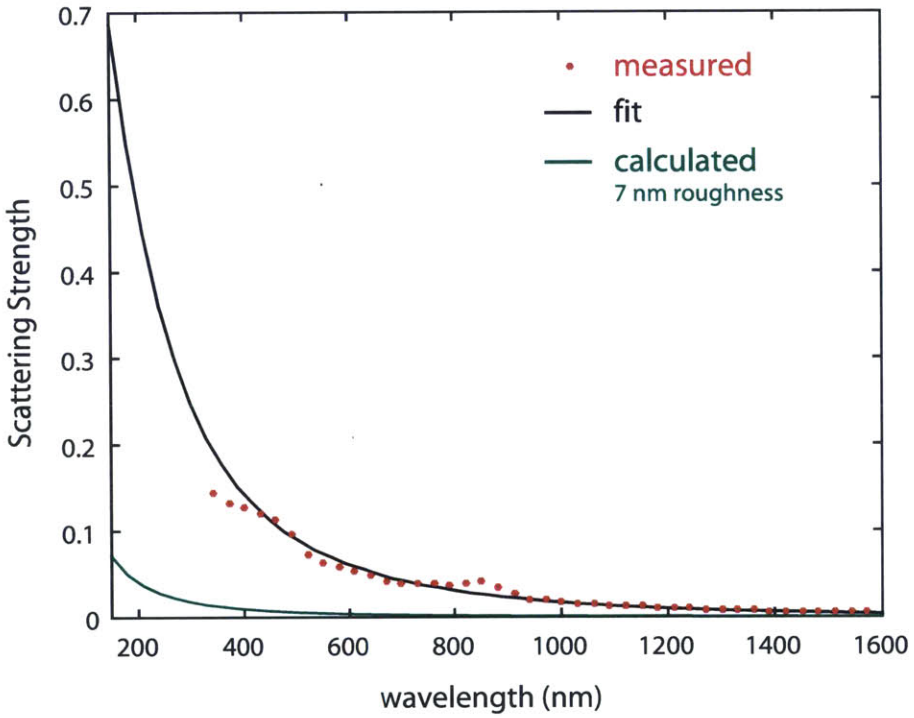

Figure 4.8 The measured scatter of a neat CdSe/CdS film is shown in red dots. These data are fit to a simple Huygens-Fresnel-based scattering model assuming a Gaussian distribution of heights at a roughness of 15 nm (black). If the roughness can be reduced to 5 nm, the expected scatter is shown in green.

nm. It should be noted that the model constructed here is well represented by the inverse energy relationship with structural scatter that is occasionally utilized in QD literature to approximately remove scatter from QD films.

4.2.4.3. Resulting EQE of neat-film CdSe/CdS LDS detector

To demonstrate far-UV-to-visible downshifting, a neat film of thick-shelled CdSe/CdS with absorption and emission spectra shown in figure 4.9 was deposited directly on to a silicon detector. The bare and QD-enhanced detector EQEs were measured from 172-1500 nm and are shown in figure 4.9. An over 2-fold increase is observed in the far- and mid-UV and a 3-fold improvement is measured in the near-UV. The model constructed in section 2.5 was insufficient to accurately represent the measured data. Generally, the model over-predicted the far- and mid-UV efficiencies and the detector band efficiency, and under-predicted the near-UV efficiency. Possible origins of these discrepancies include complicated scatter effects such as scatter-induced absorption and wavelength dependent QYs at high energies.

The field has presented contradictory evidence as to whether QDs exhibit excitation wavelength dependent QYs. Some photoluminescence emission (PLE) studies, suggest a wavelength dependent QY as evidenced by discrepancies measured between PLE and absorbance spectra. There, potential origins of this effect are hypothesized to result from coupling to ligands and other higher-energy non-radiative decay pathways only accessible at high excitation energies [31]. From similar types of data, others have concluded that the apparent dependence is actually a result of structural scattering from sample impurities. This

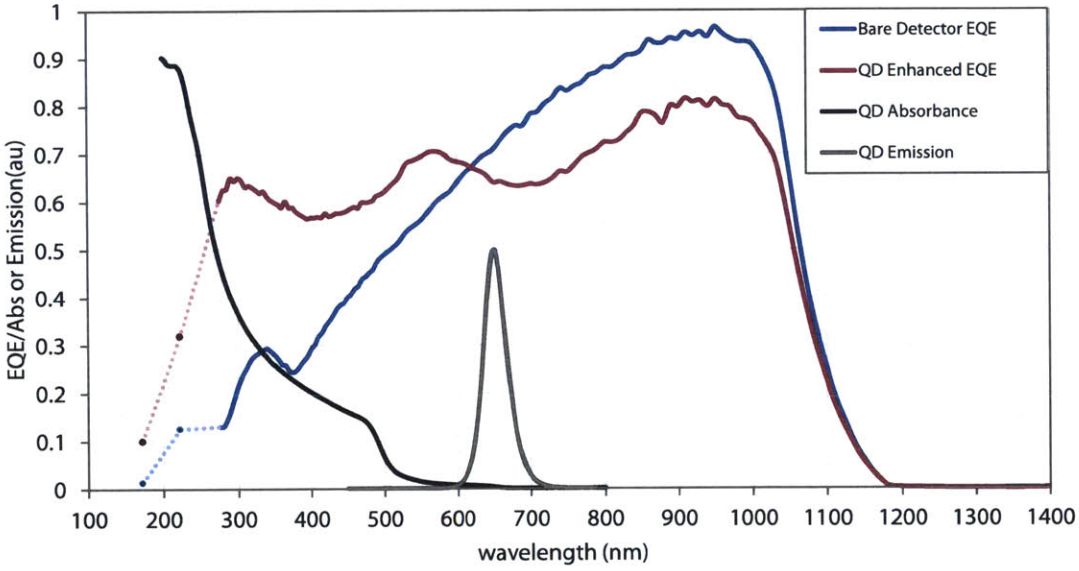

Figure 4.9 EQE enhancement via a QD-neat film. The EQE of a bare ThorLabs silicon photodiode is shown in blue. A neat film of CdSe/CdS, whose emission and absorption spectra are plotted in grey and black respectively was cast directly onto the silicon detector and the resulting enhanced detector EQE is shown in red. Single measurements were taken at 172 and 222 nm and the dotted line is a guide for the eye.

scattering artificially reduces the measured absorbance, and these authors state that in reality, high energy excitons rapidly thermalize to the band edge where emission occurs at a defined probability [32]. However, these experiments utilize sub-work-function light whereas some of the results shown here surpass the ~5.5 eV work function of CdSe QDs [33]. Consequently, there is a high likelihood that the film could be charging, which is an expected source of PL quenching [34, 35].

Above band gap luminescent stability and QY have been poorly studied. One study presented dye-comparison QYs of core-only CdSe neat films measured at 10-40 eV. Here, they report a wavelength independent QY of 20% for this range [36]. These results are questionable; however, as the dye comparison method used here is often inaccurate for films. Further, typical in-solution QYs for core-only CdSe are only 5-30%. As casting into a neat film is expected to result in significant FRET-induced reductions, a 20% neat film QY with a high energy excitation seems unreasonably high for CdSe. Although the means to safely acquire above-work function QY measurements were not available for this study, QY stability tests were performed that provide complementary insight into potential damage incurred by high energy light.

The above- and below-work function QY stability of neat CdSe/CdS films was measured by subjecting films to either 222 nm (5.6 eV) or 405 (3.1 eV) light at a photon flux of 1×10^{12} photons·mm^{-2}·s^{-1}. The irradiation time was varied and QYs were measured with a 405 nm excitation source in an integrating sphere. The resulting QYs and emission peaks are shown in figure 4.10. Due to experimental constraints, the QY of the 222 nm irradiated films were measured

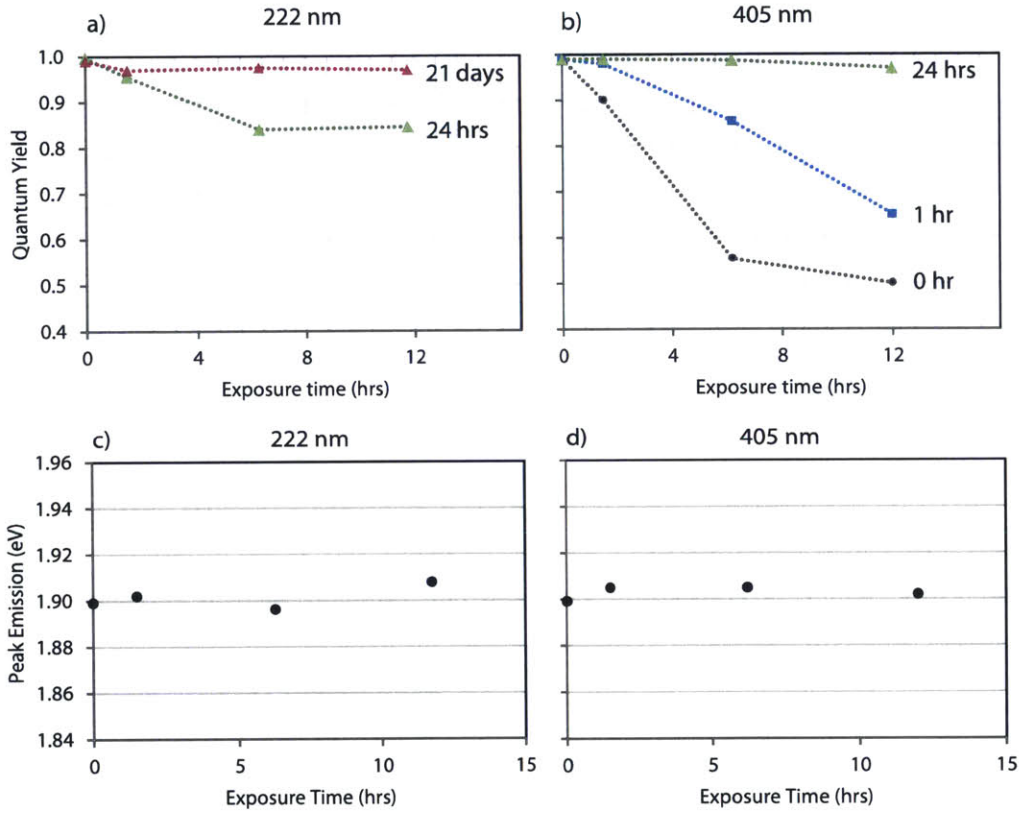

Figure 4.10 The QY stability of a neat film of thick-shelled CdSe/CdS is explored at (a) above-work function (222 nm) and (b) below-work function (405 nm) excitation energies. The samples were irradiated for various times, and their QYs measured at various times after irradiation in an integrating sphere, as designated to the right of each line. Although the below-work function irradiated sample recovered in less than a day, recovery of the above-work function samples occurred over the course of many days. The peak emission stability was found to be stable for both excitation wavelengths, as shown in (c) and (d).

24 hours after exposure. Data acquired at this time shows a decrease in the QY with increased irradiation time, potentially leveling off at ~85% after 6 hours. After 21 days, the samples were remeasured showing a near-complete recovery of the QY. The 405 nm irradiated samples were measured immediately, 1 hour, and 24 hours post irradiation. These films also displayed a decrease in QY with emission peak stability; however, recovery occurred more rapidly after less than 24 hr.

Multiple studies have explored the recoverable photodarkening of QD films at below-work function excitation energies [34, 37]. These studies generally reveal photo-induced population of dark or grey states. Some attribute the dark state origin to a charging process. Luminescent recovery can occur over the course of hours, which is consistent with the QY recovery of the sub-band gap stability measurements. It is feasible that the longer recovery time resulting from the above gap illumination also originates from dark states induced from significant film charging. The charging from above-work function excitation may be mechanistically different or to a greater degree than the below-work function excitation, potentially accounting for the longer recovery time. In order to explore and potentially mitigate this effect, a transparent conductive film could be deposited in contact with the QD film to facilitate discharging.

4.2.5 LDS demonstration with a QD-hydrocarbon polymer film

The system of QDs dispersed in hydrocarbon matrices has been optimized in the near-UV-to-SWIR for downshifting (Chapter 3). Although the spectral range of the UV-downshifted detector is limited by the absorption onset of the

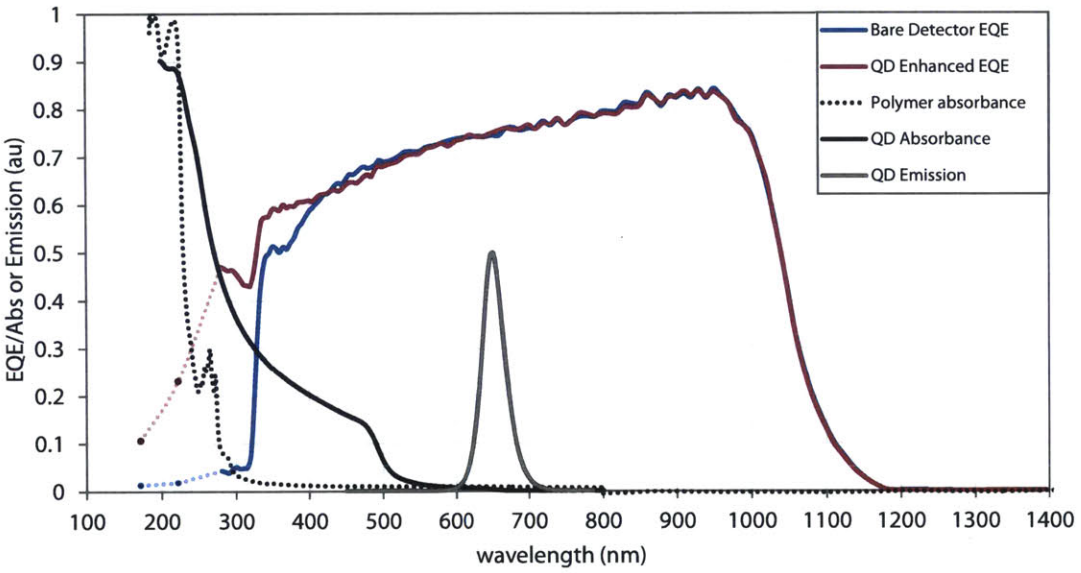

Figure 4.11 EQE enhancement via a QD-polymer film. The EQE of a bare Hamamtsu silicon photodiode is shown in blue. A layer of CdSe/CdS, whose emission and absorption spectra are plotted in grey and black respectively was deposited directly onto the detector in a PVBcoPBAcoPVAc polymer film. The resulting enhanced detector is shown in red. The polymer absorption, shown in dotted black, contributes to the downward trend of the efficiencies at shorter wavelengths.

polymer utilized, polymer films tend to greatly reduce scatter. Here the amount of polymer will be minimized to decrease polymer-induced efficiency reduction.

Filter-purified thick-shelled CdSe/CdS QDs were dispersed in polyvinyl butyral-co-vinyl alcohol-co-vinyl acetate (PVBcoPBAcoPVAc) and deposited directly onto a silicon photodetector. The initial bare detector and resulting QD-enhanced efficiencies are shown in figure 4.11. The QD-enhanced detector shows an 8-12 fold increase in efficiency throughout the near-UV. It is important to note that due to availability constraints, the bare detector used here and in the neat-film demonstration are different models and exhibit different EQEs.

In comparison to neat film downshifting, the LDS detector's efficiency has not been reduced in the bare detector band, most likely a result of minimized scatter from the QD-polymer composite film. Although scatter is mitigated, a decrease in the QD-enhanced detector's efficiency is still observed for shorter wavelengths rather than the expected increase. In this case, the decrease is attributed to the polymer's absorption onset in addition to the probable decrease in QD QY's at high energies. Despite the polymer absorption, this QD-enhanced detector still exhibits a promising 10% efficiency at 172 nm.

4.2.6 Low pressure and temperature QD-film behavior

A potential application for a QD-based UV-enhanced detector is satellite-based astronomy, which requires stability at low pressure and temperature. To evaluate this, a neat film of CdSe/CdS core/thin-shell QDs was evacuated in a cryostat to 1×10^{-5} mtorr and cooled to 77 K. The emission was monitored as a performance metric.

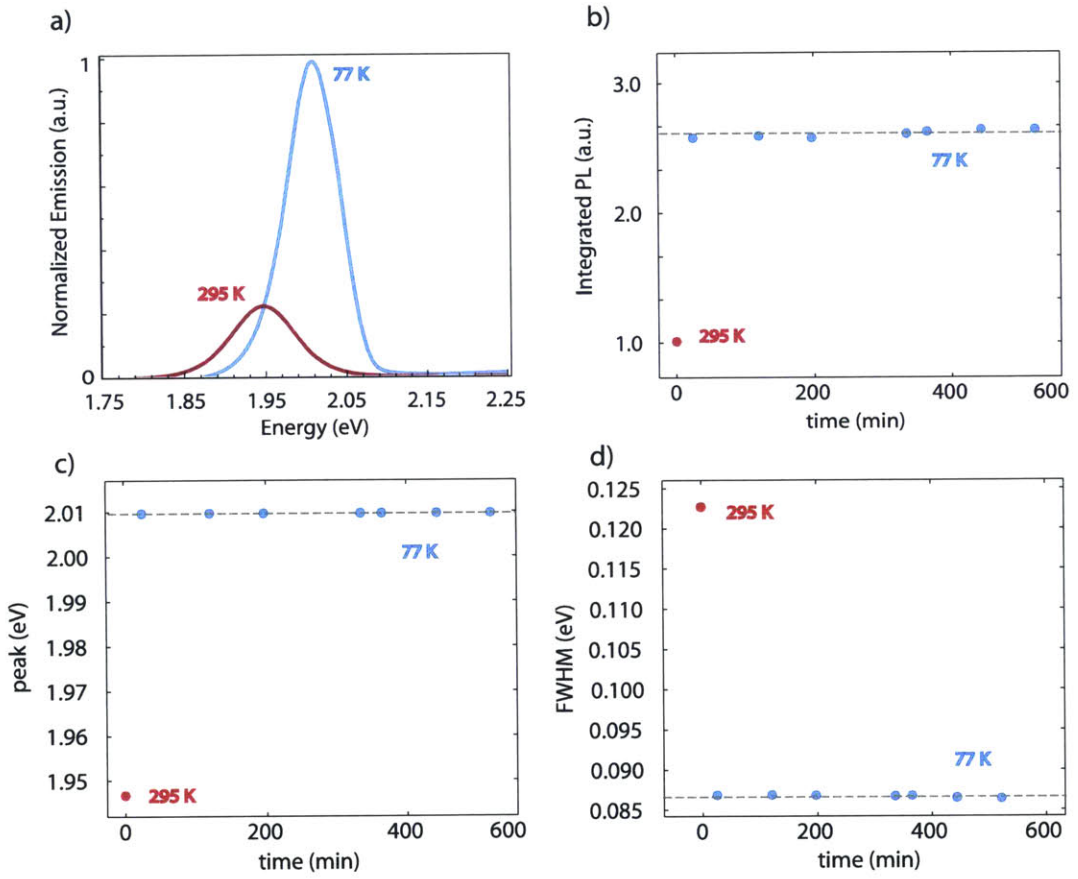

Figure 4.12 Low temperature PL stability of a CdSe/CdS neat film. a) The PL spectra of a neat film are plotted at room temperature and at 77 K. A 1.7-fold increase in emission was observed. The integrated PL, peak position, and peak FWHM were found to be stable as shown in (b), (c), and (d).

Figure 4.12 shows the relative emission at room temperature and 77 K. Upon cooling, a 65 meV blue-shift and a 1.7-fold increase in the integrated PL are observed. These metrics show stability for the several hour duration of the measurement. The PL blue-shift with reduced temperature has been documented in QD literature [38]. While this shift is not detrimental to the downshifting layer's performance, it is an important factor to consider when designing low temperature downshifting films, since maximizing the QD emission-detector EQE overlap is important for optimizing downshifting efficiency. An increase in integrated emission has also been previously observed as phonon mediated non-radiative recombination pathways are frozen out at low temperatures [38]. While these data suggest that QDs may exhibit long-term stability under extreme conditions, more strenuous tests should be performed at lower temperatures for longer times to confirm film stability before deployment.

4.2.7 Imaging with QD-based LDS camera

One of the primary benefits of a QD-based UV-enhanced photodetector is the feasibility for low-cost and modular UV imaging. Two primary methods for integrating downshifting with imaging schemes were detailed in Chapter 2. Briefly, QDs may be directly deposited on a focal plane array (FPA) or a LDS plate can be imaged through and relayed to a camera, as shown in figure 4.13. To avoid the challenge of the extensive packaging of many commercial visible cameras, this demonstration utilizes imaging through a LDS plate.

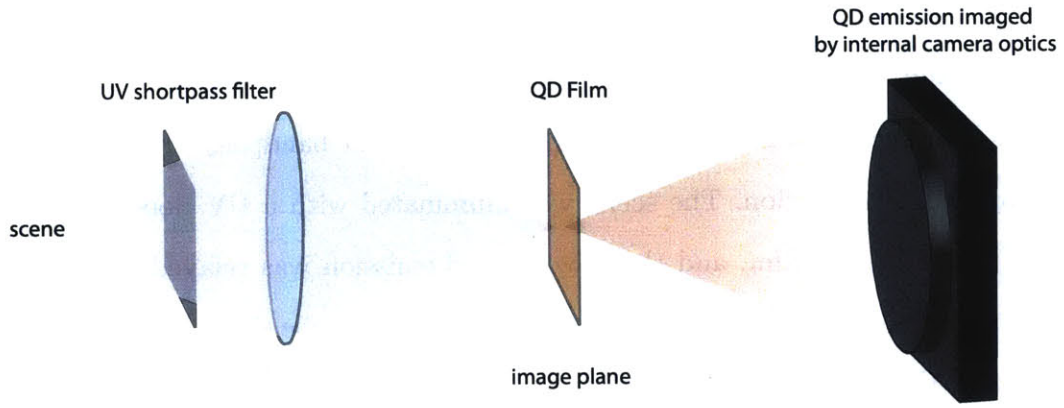

Figure 4.13 LDS imaging array scheme. UV light from a scene is imaged onto a QD LDS filter placed in the image plane. The resulting emission is then relayed to the visible camera.

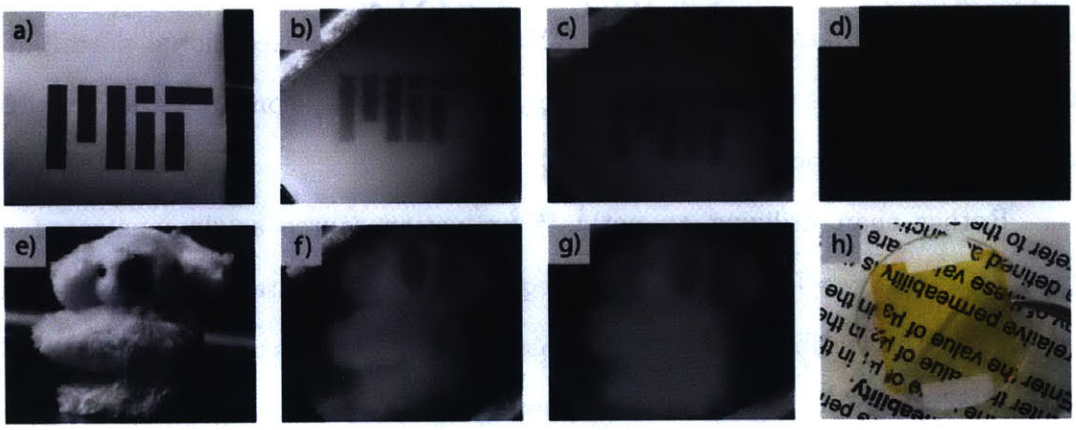

Figure 4.14 Gray scale visible scenes of two objects are shown in (a) and (e). The same objects were flood illuminated with UV light and imaged with the array shown in figure 4.13. Resulting images from a DSLR (b) and (f) and a smart phone camera (c) and (g) are shown. Image (d) illustrates the same scene without a QD LDS film and (h) shows the transparency and optical density of the downshifting film to illustrate the insignificant impact the QDs would have on a simultaneously obtained visible image.

A neat film of thick-shelled CdSe/CdS QDs was deposited on a sapphire substrate and placed at the image plane of a calcium fluoride lens imaging system. The system was equipped with a 275-375 nm bandpass filter to ensure isolation of UV-excitation. The scene was illuminated with a UV flood lamp and imaged onto the QD film, and the downshifted emission was relayed to a visible camera. The resulting images obtained with a Canon Rebel DSLR are shown in figure 4.14 (b) and (f). These images are compared to the same scenes imaged without QDs (figure 4.14d). Visible images are shown in figure 4.14 (a) and (e).

A smart phone camera can be readily utilized instead of a high-end DSLR. Shown in figures 4.14 (c) and (g) are the same scenes as viewed by a Samsung Galaxy S7 Edge camera phone. While the resolution is slightly reduced, the scenes are still easily discernable. This illustrates the exceptional portability and versatility of this technique to cheaply and compactly convert various visible cameras into UV devices.

Rather than utilizing an active illumination source as demonstrated in figure 4.14, many UV applications require passive excitation. In order to demonstrate the feasibility of sunlight-based passive illumination imaging despite the relatively low UV terrestrial solar photon flux (figure 4.15a), the optics array was equipped with a 400 nm short pass and a 275-375 nm band pass filter. Collectively, these exhibit the transmission spectra shown in figure 4.15b. Images of a scene without (figure 4.15d) and with the QD downshifting film (figure 4.15e) are compared to the visible scene (figure 4.15c). The QD-enhanced scene is significantly more apparent than the bare camera.

It is probable that most of the signal in the non-LDS image is due to the small amount of leakage through the filter set at ~710 nm. At 710nm, the solar

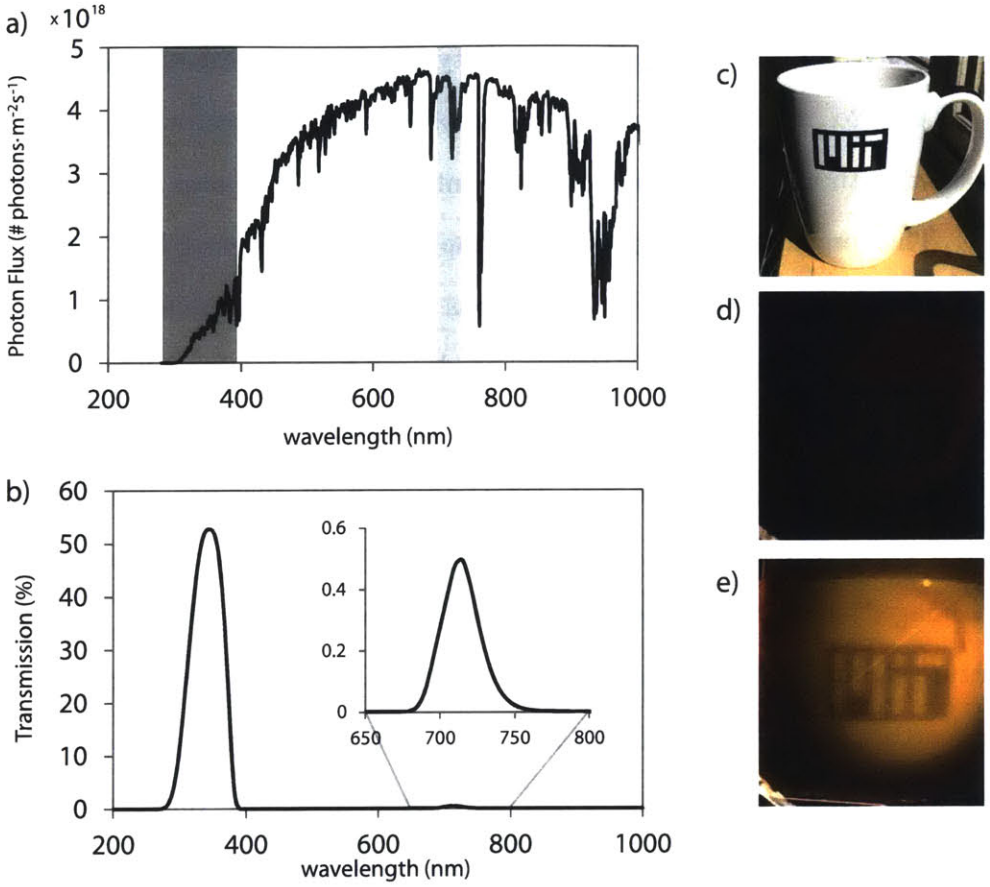

Figure 4.15 An example of passive solar UV illumination is shown. A visible image of an object is shown in (c). Using a series of band pass filters that exhibit the transmission shown in (b), an UV image of the object can be collected (e). The same image without the LDS film is shown in (d). The image here is still apparent, which may result from bare detector sensitivity to this region or a small amount of leakage around 710 nm. The solar spectrum is shown in (a) to illustrate the number of UV photons in the region of detection and leakage.

spectrum exhibits a significantly greater photon flux and the visible detector is more sensitive in this region. Higher quality UV filters or differential imaging can be utilized to remove the contribution of the bare detector from the image measured with a LDS-film to ensure the entire signal originates from the UV.

The previous UV imaging examples exploited near-UV light. While imaging with far- and mid-UV light was desired, safety concerns limited the exploration of this method. However, to demonstrate the possibility of 222 nm imaging, a CdSe/CdS neat film-coated sapphire disk was placed in an imaging array. Mid-UV 222 nm light was passed through an aperture and imaged onto the QD plate. The resulting excitation pattern was captured by a silicon camera. The imaged spots are shown in figure 4.16 where the red lines represent the aperture diameter as compared to the spot size. There is good agreement with the aperture size and the illuminated spot size, and good signal contrast. The films were heavily handled and had been unintentionally roughened, which is apparent in the images. Regardless, this demonstration illustrates the promise of imaging at higher energies.

4.2.8. Bandwidth approximation

The bandwidth of a photodetector dictates the maximum data transfer rate. As QDs require a finite amount of time to re-emit a photon, this lifetime must be taken into account when considering the effect of the QD film on the detector's performance. The PL lifetime measured by TCSPC is shown in figure 4.17, which fits well to a biexponential decay of the form $\sum_k a_k \exp\left(\frac{-t}{\tau_k}\right)$ consisting of a

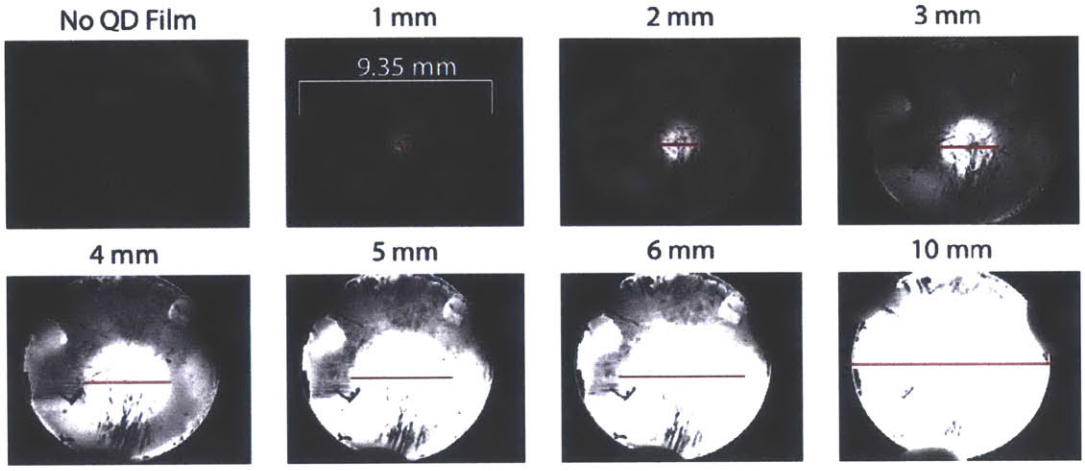

Figure 4.16 Relay detection with 222 nm light. Various spot sizes as indicated above each image were incident on a QD LDS neat film. The red line illustrates the actual spot size as a comparison to the measured size. Images were collected with a silicon visible camera.

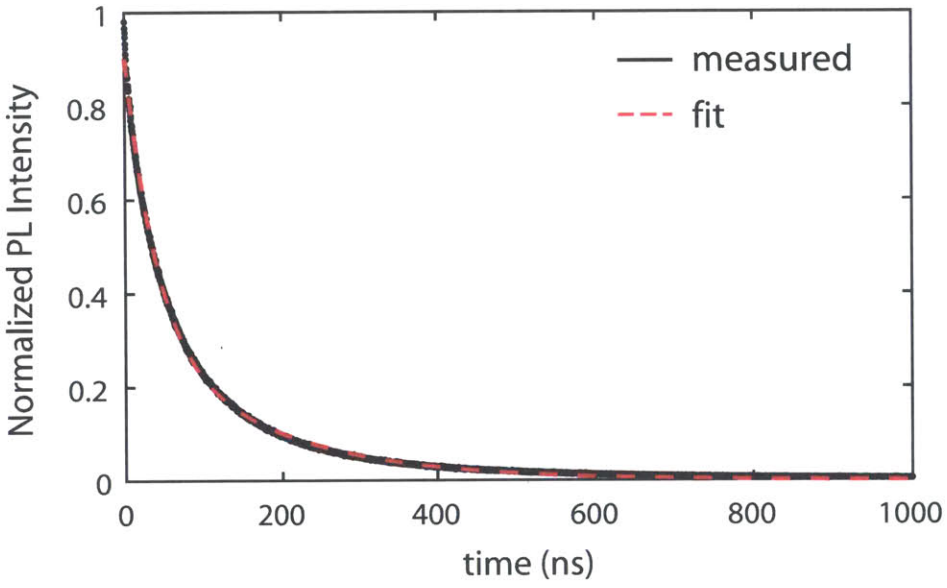

Figure 4.17 Photoluminescent lifetime of thick-shelled CdSe/CdS neat film. Measured data (black) and biexponential fit (red-dash) are shown.

fast, τ_1=36 ns, and a slow, τ_2=164 ns component with contributions of a_1=0.58 and a_2=0.32.

The expected bandwidth can be approximated by considering the relationship between a monoexponential signal decay and its frequency response as derived in section 2.8 and given by equation 2.13. A monoexponential fit can be approximated with a lifetime of τ=87.1 ns resulting in a LDS bandwidth of 5.3 MHz. The bandwidth in wavelengths above the band gap of the QDs should be largely unaffected and reflect the bare detector's bandwidth.

4.3 Conclusion and future scope

This chapter has demonstrated enhancements in the UV efficiency of visible detectors. Discrepancies in measured versus modeled UV efficiencies are attributed to scatter and reductions in QY at high excitation energies, which could be mitigated by improved film casting and design, allowing the promise for even larger increases in UV efficiency.

The versatility and simplicity of employment were demonstrated by imaging through LDS films with various cameras. The illustration that this technique could be easily employed in a compact, unobtrusive manner with cell phone cameras or in microscopes increases the feasibility for broad deployment.

4.4 Experimental details

4.4.1 QD synthesis and characterization

Thick-shelled CdSe/CdS QDs with an approximate core diameter of 5 nm and shell thickness of 5.5 nm were prepared following the protocol detailed in

Coropceanu *et al.* [39]. Absorption measurements were performed using a Cary 5000, emission spectra were measured with 400 nm excitation using a Fluoromax-3 equipped with a 490 nm long pass filter to remove the excitation signal. Quantum yield measurements were performed using an integrating sphere which has been detailed in section 2.9.1. Photoluminescent lifetime measurements were taken with a 532 nm 60 ps pulse length excitation and measured via TCSPC with a silicon APD.

4.4.2 QD purification

As organic impurities from synthesis would contribute to parasitic UV absorption and in-film scatter, their removal was imperative. To this end, the prepared solution was first crashed three times via the addition of acetone. The resulting QD pellet was redispersed in hexane and purified over the course of multiple days by flowing the solution through a Spectrum Labs MicroKros filter, which allowed impurities to be removed while retaining the QDs.

4.4.3 Film deposition

The QDs were redispersed in chlorobenzene at a concentration of 100 mg/ml. Neat films were drop cast on the detector's surface and evaporation was slowed by sealing the detectors in a chlorobenzene rich air tight container. QD-polymer composite films were prepared by previously dissolving PVBcoPVAcoPVAc in chlorobenzene at a 10% by weight concentration. Equal parts QD solution and polymer solution were combined and either drop-casted or spin-casted on the

detector's surface. Films for characterization were prepared in a similar manner on cleaned sapphire or quartz substrates.

4.4.4 Device characterization

For wavelengths between 290 and 1300 nm, the EQE experiment details in section 2.9.2 was employed. Higher energy wavelengths required the use of alternative light sources. USHIO excimer lamps emitting at 172 nm and 222 nm were utilized. The lamp specifications were confirmed with an UV ocean optics spectrometer. Due to significant light emitted from the 172 nm lamp, the setup was equipped with an Acton 176 nm (FWHM=45 nm) band pass filter which completely suppressed this artifact. UV-transparent calcium fluoride optics were used to collect lamp emission and direct it through an aperture, and scatter was minimized by containing optics in a lens tub array. The incident light was chopped at 213 Hz and the detector response was measured through a current-to-voltage preamp coupled to a lock-in amplifier. Incident light intensity was calibrated with a ThorLabs thermal power sensor and lamp emission. As these high energy wavelengths can readily create toxic ozone gas in the presence of oxygen, the system was sealed and purged with nitrogen.

4.5 Chapter-specific acknowledgments

Igor Coropceanu synthesized the thick shelled CdSe/CdS QDs and contributed to discussions. Jose Cordero provided advice for QD filter purification. Experimental assistance for measuring 172 and 222 nm EQE was provided by Chuck Wynn. High energy measurements were acquired in collaboration with

Harold Hwang who also contributed to fruitful discussions. Guidance for lifetime measurements was provided by Lea Neinhaus. Assistance with the film scattering model was provided by Sam Teitelbaum.

4.6 References

[1] C. Adams, R. Carabott and S. Evans. **Forensic Odontology: An Essential Guide**. Wiley (2013).

[2] A. Richards and R. Leintz. "Forensic Reflected Ultraviolet Imaging." *Journal of Forensic Identification*, **63**, (2013).

[3] N. Yosef, J. Almog, A. Frank, E. Springer and A. Cantu. "Short UV Luminescence for Forensic Applications: Design of a Real-Time Observation System for Detection of Latent Fingerprints and Body Fluids." *Journal of Forensic Sciences*, **43**, 299 (1998).

[4] Q. He, Z. Xu and B. M. Sadler. "Performance of short-range non-line-of-sight LED-based ultraviolet communication receivers." *Opt. Express*, **18**, 12226 (2010).

[5] Z. Xu and B. M. Sadler. "Ultraviolet Communications: Potential and State-Of-The-Art." *IEEE Communications Magazine*, **46**, 67 (2008).

[6] J. Holtzman, J. J. Hester, S. Casertano, J. T. Trauger, A. M. Watson, G. E. Ballester, C. J. Burrows, J. T. Clarke, D. Crisp, R. W. Evans, J. S. Gallagher, R. E. Griffiths, J. G. Hoessel, L. D. Matthews, J. R. Mould, P. A. Scowen, K. R. Stapelfeldt and J. A. Westphal. "The Performance and Calibration of WFPC2 on the Hubble Space Telescope." *Publications of the Astronomical Society of the Pacific*, **107**, 156 (1995).

[7] E. Trakhovsky, A. Ben-Shalom, U. P. Oppenheim, A. D. Devir, L. S. Balfour and M. Engel. "Contribution of oxygen to attenuation in the solar blind UV spectral region." *Appl. Opt.*, **28**, 1588 (1989).

[8] T. Dubroca, G. Brown and R. E. Hummel. "Detection of explosives by differential hyperspectral imaging." *OPTICE*, **53**, 021112 (2014).

[9] A. R. Naveen, C. S. Charles, P. Max, L. A. Kurt, E. S. Alice, K. E. Dawn and D. Mark. "Multiwavelength Constraints on the Cosmic Star Formation History from Spectroscopy: The Rest-Frame Ultraviolet, Hα, and Infrared Luminosity Functions at Redshifts 1.9 z 3.4." *The Astrophysical Journal Supplement Series*, **175**, 48 (2008).

[10] N. R. Council. **Seeing Photons: Progress and Limits of Visible and Infrared Sensor Arrays**. (Washington, DC: The National Academies Press) (2010).

[11] P. Jerram, D. Burt, N. Guyatt, V. Hibon, J. Vaillant and Y. Henrion. "Back-thinned CMOS sensor optimization." *in* (2010).

[12] M. E. Hoenk, T. J. Jones, M. R. Dickie, F. Greer, T. J. Cunningham, E. R. Blazejewski and S. Nikzad. "Delta-doped back-illuminated CMOS imaging arrays: progress and prospects." *in* (2009).

[13] L. Sang, M. Liao and M. Sumiya. "A comprehensive review of semiconductor ultraviolet photodetectors: from thin film to one-dimensional nanostructures." *Sensors*, **13**, 10482 (2013).

[14] W. Deslandes A, A B, Clark S R, Matisons J G, Quinton J S. "Characterisation of PVD Lumogenff films for wavelength conversion applications " *Smart Structures, Devices, and Systems II*, **5649**, (2005).

[15] H. Xugen, Z. Sihua, P. Wei and S. Wenzhong. "A simple strategy for synthesizing highly luminescent carbon nanodots and application as effective down-shifting layers." *Nanotechnology*, **26**, 065402 (2015).

[16] X. Sheng, C. J. Corcoran, J. He, L. Shen, S. Kim, J. Park, R. G. Nuzzo and J. A. Rogers. "Enhanced ultraviolet responses in thin-film InGaP solar cells by down-shifting." *Physical Chemistry Chemical Physics*, **15**, 20434 (2013).

[17] S. Kalytchuk, S. Gupta, O. Zhovtiuk, A. Vaneski, S. V. Kershaw, H. Fu, Z. Fan, E. C. H. Kwok, C.-F. Wang, W. Y. Teoh and A. L. Rogach. "Semiconductor Nanocrystals as Luminescent Down-Shifting Layers To Enhance the Efficiency of Thin-Film CdTe/CdS and Crystalline Si Solar Cells." *The Journal of Physical Chemistry C*, **118**, 16393 (2014).

[18] R. Robinson, Z. Ninkov, D. Cormier, A. Raisanen, S. Bhaskaran, C. Beam, H. Ziegler, U. Arp and R. Vest. "First report on quantum dot coated CMOS CID arrays for the UV and VUV." *SPIE Proceedings*, **8859**, 88590K (2013).

[19] D. Alonso-Œlvarez, D. Ross, E. Klampaftis, K. R. McIntosh, S. Jia, P. Storiz, T. Stolz and B. S. Richards. "Luminescent down-shifting experiment and modelling with multiple photovoltaic technologies." *Progress in Photovoltaics: Research and Applications*, **23**, 479 (2015).

[20] N. C. Anderson, M. P. Hendricks, J. J. Choi and J. S. Owen. "Ligand Exchange and the Stoichiometry of Metal Chalcogenide Nanocrystals: Spectroscopic Observation of Facile Metal-Carboxylate Displacement and Binding." *Journal of the American Chemical Society*, **135**, 18536 (2013).

[21] J. S. Steckel, S. Coe-Sullivan, V. Bulović and M. G. Bawendi. "1.3 μm to 1.55 μm Tunable Electroluminescence from PbSe Quantum Dots Embedded within an Organic Device." *Advanced Materials*, **15**, 1862 (2003).

[22] B. A. Brice and M. L. Swain. "Ultraviolet Absorption Method for the Determination of Polyunsaturated Constituents in Fatty Materials*." *J. Opt. Soc. Am.*, **35**, 532 (1945).

[23] A. Nag, M. V. Kovalenko, J.-S. Lee, W. Liu, B. Spokoyny and D. V. Talapin. "Metal-free Inorganic Ligands for Colloidal Nanocrystals: S^{2-}, HS^{-}, Se^{2-}, HSe^{-}, Te^{2-}, HTe^{-}, TeS_3^{2-}, OH^{-}, and NH^{2-} as Surface Ligands." *Journal of the American Chemical Society*, **133**, 10612 (2011).

[24] A. W. Wills, M. S. Kang, A. Khare, W. L. Gladfelter and D. J. Norris. "Thermally Degradable Ligands for Nanocrystals." *ACS Nano*, **4**, 4523 (2010).

[25] S. Kalytchuk, O. Zhovtiuk and A. L. Rogach. "Sodium chloride protected CdTe quantum dot based solid-state luminophores with high color quality and fluorescence efficiency." *Applied Physics Letters*, **103**, 103105 (2013).

[26] M. Müller, M. Kaiser, G. M. Stachowski, U. Resch-Genger, N. Gaponik and A. Eychmüller. "Photoluminescence Quantum Yield and Matrix-Induced Luminescence Enhancement of Colloidal Quantum Dots Embedded in Ionic Crystals." *Chemistry of Materials*, **26**, 3231 (2014).

[27] T. Otto, M. Müller, P. Mundra, V. Lesnyak, H. V. Demir, N. Gaponik and A. Eychmüller. "Colloidal Nanocrystals Embedded in Macrocrystals: Robustness, Photostability, and Color Purity." *Nano Letters*, **12**, 5348 (2012).

[28] M. Adam, Z. Wang, A. Dubavik, G. M. Stachowski, C. Meerbach, Z. Soran-Erdem, C. Rengers, H. V. Demir, N. Gaponik and A. Eychmüller. "Liquid–Liquid Diffusion-Assisted Crystallization: A Fast and Versatile Approach Toward High Quality Mixed Quantum Dot-Salt Crystals." *Advanced Functional Materials*, **25**, 2638 (2015).

[29] Y. Chen, J. Vela, H. Htoon, J. L. Casson, D. J. Werder, D. A. Bussian, V. I. Klimov and J. A. Hollingsworth. ""Giant" Multishell CdSe Nanocrystal Quantum Dots with Suppressed Blinking." *Journal of the American Chemical Society*, **130**, 5026 (2008).

[30] A. F. Fercher and C. K. Hitzenberger. "Chapter 4 - Optical coherence tomography." *in* Progress in Optics. edited by E. Wolf (Elsevier 2002).

[31] J. Hoy, P. J. Morrison, L. K. Steinberg, W. E. Buhro and R. A. Loomis. "Excitation Energy Dependence of the Photoluminescence Quantum Yields of Core and Core/Shell Quantum Dots." *The Journal of Physical Chemistry Letters*, **4**, 2053 (2013).

[32] D. Tonti, F. van Mourik and M. Chergui. "On the Excitation Wavelength Dependence of the Luminescence Yield of Colloidal CdSe Quantum Dots." *Nano Letters*, **4**, 2483 (2004).

[33] J. Jasieniak, M. Califano and S. E. Watkins. "Size-Dependent Valence and Conduction Band-Edge Energies of Semiconductor Nanocrystals." *ACS Nano*, **5**, 5888 (2011).

[34] C. Galland, Y. Ghosh, A. Steinbrück, J. A. Hollingsworth, H. Htoon and V. I. Klimov. "Lifetime blinking in nonblinking nanocrystal quantum dots." *Nat Commun*, **3**, 908 (2012).

[35] P. P. Jha and P. Guyot-Sionnest. "Trion Decay in Colloidal Quantum Dots." *ACS Nano*, **3**, 1011 (2009).

[36] A. Kaplan, A. Sajwani, Z. Y. Li, R. E. Palmer and J. P. Wilcoxon. "Efficient vacuum ultraviolet light frequency downconversion by thin films of CdSe quantum dots." *Applied Physics Letters*, **88**, 171105 (2006).

[37] R. A. Jensen, I. Coropceanu, Y. Chen and M. G. Bawendi. "Thermal Recovery of Colloidal Quantum Dot Ensembles Following Photoinduced Dimming." *The Journal of Physical Chemistry Letters*, **6**, 2933 (2015).

[38] S. Brovelli, R. D. Schaller, S. A. Crooker, F. García-Santamaría, Y. Chen, R. Viswanatha, J. A. Hollingsworth, H. Htoon and V. I. Klimov. "Nano-engineered electron–hole exchange interaction controls exciton dynamics in core–shell semiconductor nanocrystals." *Nat Commun*, **2**, 280 (2011).

[39] I. Coropceanu and M. G. Bawendi. "Core/Shell Quantum Dot Based Luminescent Solar Concentrators with Reduced Reabsorption and Enhanced Efficiency." *Nano Letters*, **14**, 4097 (2014).

Chapter 5

Prospects for the Extension of Luminescent Downshifting into the MWIR

5.1. Introduction

Chapters 3 and 4 discussed the implementation of QD-based downshifting to the visible and SWIR where QD quality has been progressing for multiple decades. In contrast, longer wavelength emitting QDs are still in their developmental infancy. Here we will discuss the prospects of creating very broad UV-through-MWIR detectors via luminescent downshifting (LDS).

Broadband detectors that span this wide wavelength range would have comparable benefits as the UV-Vis and UV-SWIR detectors previously discussed, but the increase in functionality can be even greater without a substantial increase in size, weight, or power requirements. UV-MWIR detectors would be of particular use on weight-sensitive employments such as satellites, aerial vehicles, or on-person applications that exploit a wide spectral range including

remote sensing and hyperspectral imaging. The extension of downshifting presents unique challenges that will be discussed.

5.2. Considerations of MWIR downshifting challenges

Two primary challenges that arise when considering downshifting to the MWIR include developing strategies to reduce FRET while avoiding parasitic matrix absorbance, and overcoming the low QY of longer wavelength IR emitting QDs. The origins of and strategies to address these issues are considered in the following sections.

5.2.1 FRET reduction

As has been discussed in previous chapters, the close proximity of QDs in neat films allows for Forster resonance energy transfer (FRET) from bright to dark QDs which reduces the effective in-film QY. FRET efficiency is strongly dependent on donor-acceptor distance and the spectral overlap of donor emission and accepter absorption. FRET was reduced in the near UV-SWIR downshifting system by the incorporation of QDs into a polymer to increase dot-to-dot distance. For the mid UV-visible system where the UV absorbance of the polymer is parasitic, a neat film of CdSe/CdS thick-shelled QDs was utilized to both increase dot-to-dot distance and effectively separate the donor emission and accepter absorbance. At the current state of the field, thick-shelled IR emitting QDs have yet to be developed and hydrocarbon polymers exhibit significant vibrational absorption in the SWIR-MWIR regions. Consequently, an alternate solution is required.

There have been some demonstrations of increased lead chalcogenide QD Stokes shift which could potentially be considered to reduce FRET. In an exploration of the temperature dependence of PbS optical properties, it was discovered that while the absorption feature is relatively temperature independent, the emission redshifts [1]. This observation was attributed to absorption and emission originating from different states, and results in an increase in Stokes shift of 50 meV at low temperatures for the sample studied. While this effect will reduce FRET, it is not expected to be substantial enough to maintain a high QY.

Alternatively, the stoichiometry can be utilized to modify the Stokes shift. Although the QD Stokes shift typically reduces as the particles grow, the addition of excess surface sulfur can result in a constant Stokes shift with red-shifting emission. Consequently, a sulfur-rich particle and an as-synthesized particle with identical emission energies can have Stokes shifts that vary by 40 meV. These results are further discussed in Appendix A. This shift, however, is again likely too small to mitigate FRET and is coupled to a decrease in QY, which is detrimental to the performance of the LDS film. As options to reduce FRET by increasing the Stokes shift are unviable, attention is turned to increasing inter-dot distance through embedding the QDs into a non-hydrocarbon matrix.

The primary challenge of utilizing a matrix for a UV-MWIR detector is the ensuring high transparency for a large spectral range. Two possible transparent matrices were explored, including high band gap inorganics and fluorinated polymers. While there has been some success with the incorporation of QDs into salt crystals such as NaCl, these films require weeks of drying times

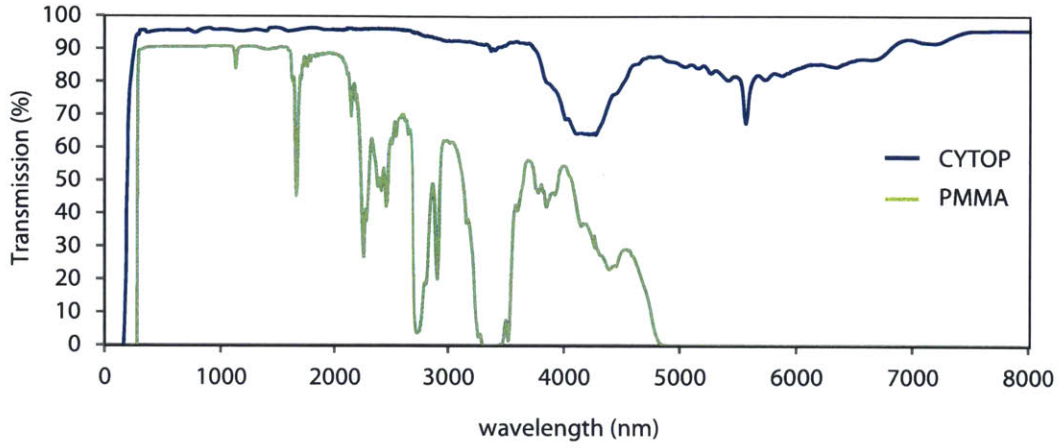

Figure 5.1 Transmission spectra of PMMA compared to the fluorinated polymer CYTOP. Hydrocarbon polymers like PMMA exhibit strong absorbance in the SWIR whereas halogenated polymers such as CYTOP tend to have high transmission in this region.

and exhibit substantial scatter, reducing the potential collection efficiency of the film [2-4].

Instead, fluorinated polymers were utilized. While hydrocarbon polymers exhibit significant vibrational absorbance in the infrared, fluorination results in a shift of these frequencies to lower wavelengths as expected from a simple Hooke's law consideration. For example, the transmission spectra of 1 μm thick films of poly(methyl methacrylate) (PMMA), a polymer commonly used to disperse QDs, and CYTOP, a fluorinated polymer, are shown in figure 5.1. While PMMA exhibits SWIR and MWIR absorbance, CYTOP is highly transparent from 190-3600 nm.

Although CYTOP displays superior transmission, the incorporation of QDs into this material presents a new challenge, namely that highly fluorinated materials are immiscible with hydrocarbons, and the native oleic acid ligands on

the QD surface dictate their solubility. The phase separation that results from poor miscibility creates a highly scattering film without mitigating FRET.

In order to improve the miscibility of QDs in the CYTOP matrix, a ligand exchange to a fluorinated ligand was performed. After an exploration of a variety of fluorinated ligands which led to the degradation of the QDs, perfluorotetradecanoic acid provided a stable solution of PbSe/CdSe QDs that could be incorporated into CYTOP [5]. Additionally the flexible durability of CYTOP allowed for delamination from the casting substrate, removing requirement of utilizing UV-SWIR transparent substrates.

5.2.2 Wavelength dependence of QY and low temperature improvement

Efforts to improve the QY of the visibly emitting CdSe/CdS class of QDs have spanned decades, resulting in the field's current capability to produce near unity, extremely monodispersed particles. The more juvenile class of lead chalcogenide IR emitting QDs has seen significant progress but still suffers from significantly lower QYs that originate from the absence of high quality shells and the generally observed downward trend of QY at longer wavelengths. Shell growth on lead chalcogenide QDs exhibits multiple challenges, which are further discussed in Appendix A.

Although small PbS and PbSe QDs may have QYs upwards of 70%, the QY trends toward zero for longer wavelength emitters. This effect has been observed in this work which has corroborated efforts from Semonin *et al.* They have proposed a number of potential explanations for this trend, including exciton coupling to ligand vibrational modes and increased multiphonon relaxation rates to in-gap and band-edge states[6].

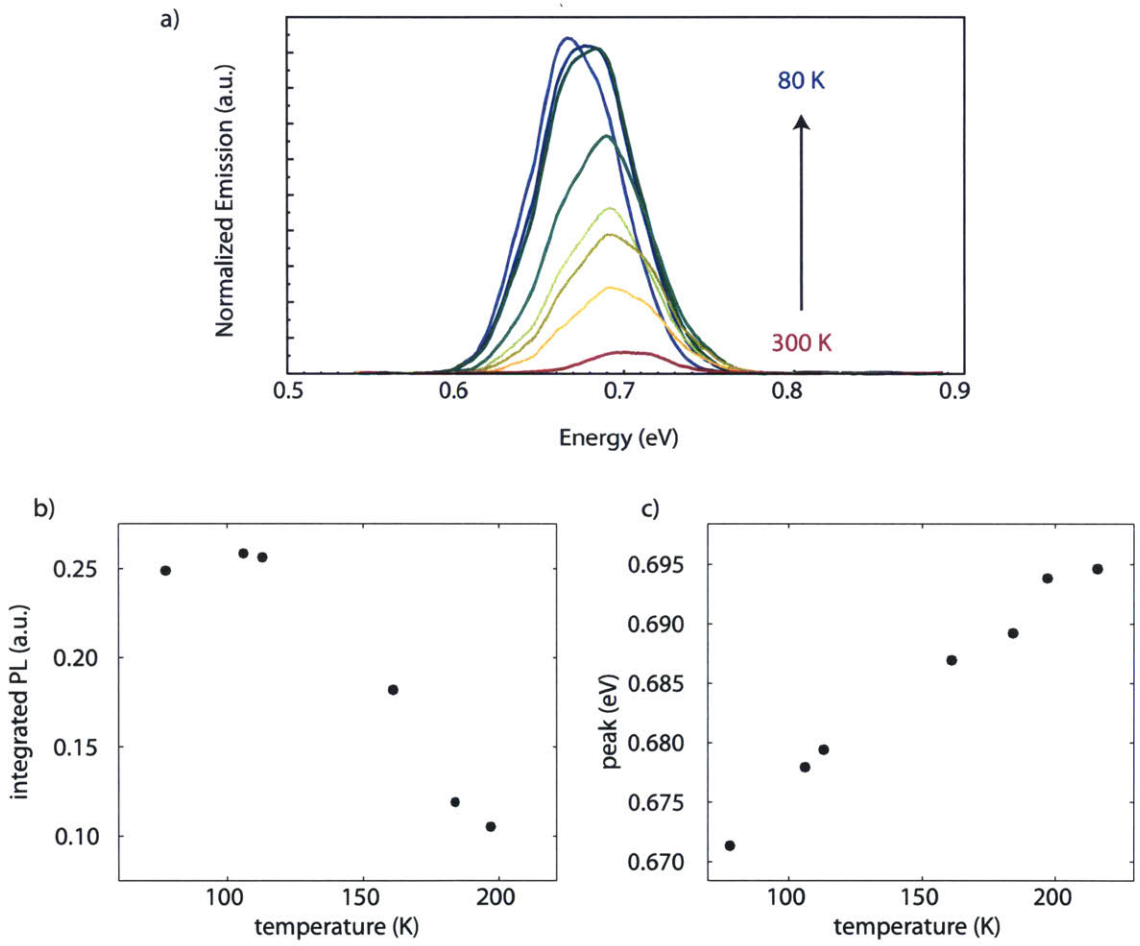

Figure 5.2 Low temperature PL characteristics of PbSe/CdSe-CYTOP films a) Low temperature emission of PbSe/CdSe-CYTOP film from 300 K to 80 K. An increase in integrated PL (b) and a red-shift of peak position (c) are observed as temperature is reduced.

Coupling to ligand vibrational modes can be mitigated by using fluorinated ligands, as was demonstrated by the Guyot-Sionnest group [5]. Here, they exchanged the native oleic acid ligands with fluorinated derivatives on PbSe QDs. An increase in transient PL lifetime was observed upon ligand exchange supporting an model accounting for energy transfer to the hydrocarbon ligands. However, this method did not result in an overall increase in the integrated PL, likely due to surface defects introduced during ligand exchange.

Parasitic multiphonon relaxation processes are expected to diminish with reduced temperature. Numerous past studies have explored the effects of low temperature on lead chalcogenide emission in various environments [1, 5]. While the effect is complex, temperatures lower than room temperature generally result in a higher integrated PL. The low temperature behavior of the LDS system utilized in this work is shown in figure 5.2a-c. As the temperature is reduced from 300 K to 80 K, a 2.5-fold increase in the integrated PL is observed. The substantial increase in PL intensity with cooling is currently the most reasonable means to achieve an effective long-wavelength LDS film, and the approach naturally dovetails into the required low temperature operation of many SWIR-MWIR detectors.

5.3 Predicted efficiency improvement of QD-based UV-MWIR detectors

This work has developed a potential LDS film strategy utilizing a cooled PbSe/CdSe-fluorinated polymer film. Additionally, instead of emitting into the MWIR region where QD QYs are less than 5%, a SWIR-MWIR detector will be considered such that high QY QDs can be utilized while still allowing extension into the UV and visible.

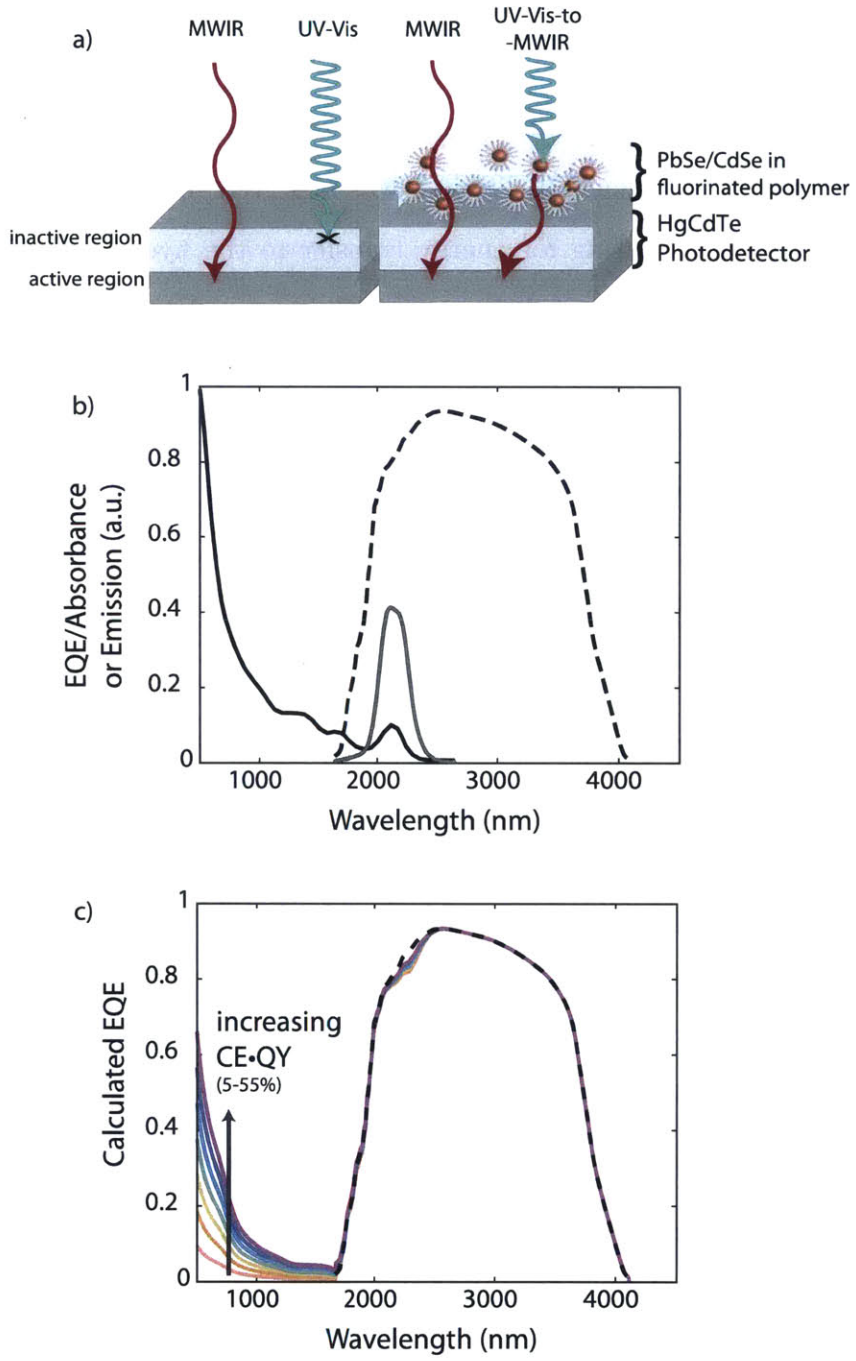

Figure 5.3 Estimated EQE of a QD-based LDS detector a) UV-Vis-to-MWIR downshifting scheme. b) Absorbance (black) and emission (grey) of a sample of PbSe/CdSe QDs compared to the EQE of a bare HgCdTe detector which extends into the MWIR. c) Calculated increase of EQE in the UV and visible as a function of increasing collection efficiency×quantum yield.

The EQE of a bare mercury cadmium telluride (HgCdTe) detector along with the absorbance and emission of a sample of PbSe/CdSe QDs is shown in figure 5.3a. The model constructed in section 2.5 can be used to estimate the expected efficiency enhancement of the downshifting film developed in this chapter. Provided an in-film low temperature QY of 5-7% which has been demonstrated here, a ~5-10% EQE is obtainable from the visible region down to the CYTOP's absorption band at 190 nm (Figure 5.3b). As the QY of infrared emitting particles improves, the efficiencies can reach upwards of 60% in the visible and UV.

5.4 Conclusions and future scope

A potentially viable LDS system has been created through the use of PbSe/CdS QDs in a transparent CYTOP matrix for the extension of a SWIR-MWIR detector to the UV and visible. Although the QY of the system can be improved through cooling, the resulting QY is only 5-7%. While an enhancement in the UV and visible of up to 5-10% is currently possible, improvements in the QY of these particles though shell growth or the reduction of phonon-electron coupling would be instrumental in creating a commercially viable system. Additional improvements are expected as the bare SWIR-MWIR detectors continue to see efficiency enhancements and reductions in cost.

5.5 Experimental methods

5.5.1 QD preparation

PbSe cores were produced via a modified previously published preparation[7]. Briefly, lead oxide (0.892 g, 4 mmol) oleic acid (2.83 g, 10 mmol), ODE (12 g, 27

mmol) were combined in a 3-neck round-bottom flask equipped with a stir bar and evacuated on a Schlenk line. While stirring, the flask was slowly heated to 100 °C under vacuum to degas the solution. The flask was returned to nitrogen and the temperature was increased to 160 °C at which point a solution of TOPSe (2 ml, 2 M) was rapidly injected to initiate nucleation. The heating mantle was removed and the solution was allowed to cool. Resulting particles were cannula transferred to an evacuated flask and transferred to a glovebox for purification. QDs were purified via the addition of isopropanol followed by centrifugation. The resulting pellet was redispersed in hexane and the process was repeated twice. The final pellet was redispersed in toluene.

In order to create a thin shell of CdSe on the surface of PbSe, a modified cation exchange was performed [8]. To a stir bar equipped vial, PbSe in toluene (1 ml, 25-50 mg/ml) was combined with previously prepared cadmium oleate (0.1 mL, 0.2 M in oleic acid). The solution was stirred for 30 min at 60-80 °C. The resulting QDs were crashed three times with isopropanol and redispersed in chloroform.

5.5.2 Ligand exchange and polymer incorporation

Ligand exchange from oleic acid to perfluorotetradecanoic acid was performed via a biphasic ligand exchange [5]. Perfluorotetradecanoic acid (20 mmol, 15 mg) dissolved in perfluoro-1,3-dimethylcyclohexane (1 ml) at 70°C to which A solution of once crashed PbSe/CdSe (1 ml, 25-50 mg/ml) in chloroform was added. The vial was shaken for roughly one minute to facilitate ligand exchange, evident by the transfer of QDs from the top chloroform layer to the bottom perfluoro-1,3-dimethylcyclohexane layer. The chloroform layer was

removed and the perfluoro-1,3-dimethylcyclohexane layer was washed three times with fresh chloroform.

The ligand exchanged QD solution was immediately combined with an equal quantity of CYTOP and drop cast onto a sapphire substrate. The evaporation of residual solvent required heating to 80 °C for at least 2 hours.

5.5.3 Low temperature measurements

Low temperature PL measurements were acquired in a cryostat. The QD-CYTOP film was affixed to a copper fixture with copper tape. Cryogenic N grease from Apiezon was applied to facilitate temperature equilibration. The cryostat was evacuated to 1×10^{-5} mbar through use of a roughing pump/turbo pump system, and liquid nitrogen was used to cool the sample from room temperature to 80K. A Lakeshore 330 temperature controller was used for the controlled temperature increase of the sample and adequate time was allowed between measurements for temperature equilibration.

PL spectra were measured by exciting samples with a 532 nm laser diode and scanning emission with a Princeton instruments monochromator equipped with an InAs single point detector.

5.6 Chapter-specific acknowledgements

The idea of UV-MWIR downshifting was synthesized in collaboration with Scott Geyer and Frank Jaworski. Eric Johlin provided assistance with long wavelength transmission measurements of polymer matrices.

5.7 References

[1] M. S. Gaponenko, N. A. Tolstik, A. A. Lutich, A. A. Onushchenko and K. V. Yumashev. "Temperature-dependent photoluminescence Stokes shift in PbS quantum dots." *Physica E: Low-dimensional Systems and Nanostructures*, **53**, 63 (2013).

[2] M. Adam, Z. Wang, A. Dubavik, G. M. Stachowski, C. Meerbach, Z. Soran-Erdem, C. Rengers, H. V. Demir, N. Gaponik and A. Eychmüller. "Liquid–Liquid Diffusion-Assisted Crystallization: A Fast and Versatile Approach Toward High Quality Mixed Quantum Dot-Salt Crystals." *Advanced Functional Materials*, **25**, 2638 (2015).

[3] M. Müller, M. Kaiser, G. M. Stachowski, U. Resch-Genger, N. Gaponik and A. Eychmüller. "Photoluminescence Quantum Yield and Matrix-Induced Luminescence Enhancement of Colloidal Quantum Dots Embedded in Ionic Crystals." *Chemistry of Materials*, **26**, 3231 (2014).

[4] T. Otto, M. Müller, P. Mundra, V. Lesnyak, H. V. Demir, N. Gaponik and A. Eychmüller. "Colloidal Nanocrystals Embedded in Macrocrystals: Robustness, Photostability, and Color Purity." *Nano Letters*, **12**, 5348 (2012).

[5] H. Liu and P. Guyot-Sionnest. "Photoluminescence Lifetime of Lead Selenide Colloidal Quantum Dots." *The Journal of Physical Chemistry C*, **114**, 14860 (2010).

[6] O. E. Semonin, J. C. Johnson, J. M. Luther, A. G. Midgett, A. J. Nozik and M. C. Beard. "Absolute Photoluminescence Quantum Yields of IR-26 Dye, PbS, and PbSe Quantum Dots." *The Journal of Physical Chemistry Letters*, **1**, 2445 (2010).

[7] W. W. Yu, J. C. Falkner, B. S. Shih and V. L. Colvin. "Preparation and Characterization of Monodisperse PbSe Semiconductor Nanocrystals in a Noncoordinating Solvent." *Chemistry of Materials*, **16**, 3318 (2004).

[8] J. M. Pietryga, D. J. Werder, D. J. Williams, J. L. Casson, R. D. Schaller, V. I. Klimov and J. A. Hollingsworth. "Utilizing the Lability of Lead Selenide to Produce Heterostructured Nanocrystals with Bright, Stable Infrared Emission." *Journal of the American Chemical Society*, **130**, 4879 (2008).

Appendix A

Considerations of Lead Chalcogenide Surface Modification: Challenges of Shell Growth and Effects of Stoichiometry

A.1 Introduction

Among the most important synthetic achievements in the field of QDs has been the growth of a high quality shell. QD radiative properties are largely dominated by surface states, which can be plagued by unpassivated bonds and unstoichiometry [1]. The growth of a type-I epitaxial shell can localize the exciton in the center of the QD and allow for reduced interaction between these surface states and the exciton, greatly improving the radiative probability [2]. For instance, CdSe cores generally exhibit QYs from 5-30%, but the growth of high quality shells has enabled near unity values. Type-II heterostructures, where one carrier is localized in the shell while the other is localized in the core, and interted type-I heterostructures, where both carriers are more localized

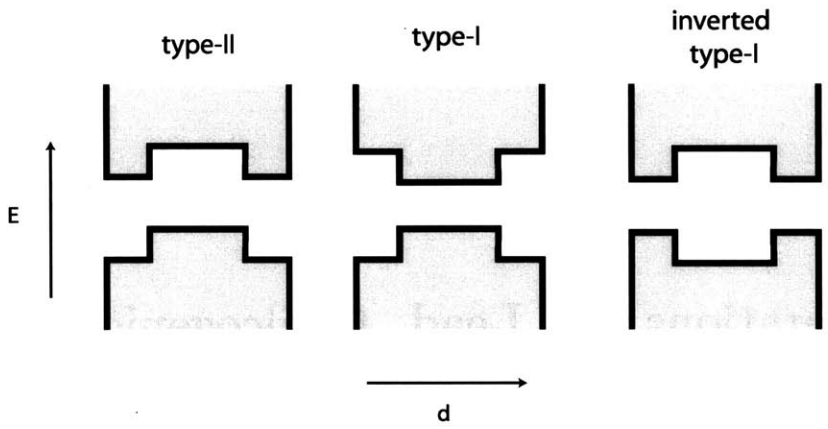

Figure A.1 Illustration of core-shell energetic heterostructures. Depending on the energetic alignment between the core and shell, the probability density of the excited species' wavefunctions can be modified. Type-I shells exhibit a higher energy than the core, allowing for a localization of both the hole and electron in the core. Conversely, the smaller shell bandgap of inverted type-I allows for both carriers to increase their in-shell probability density. Type-II heterostructures result in the electron and hole taking residence in opposite locations. In the cartoon illustrated here, the hole would be more localized in the core while the electron would be more localized in the shell.

in the shell, can also be utilized to facilite conduction or increase radiative lifetime by modifying the QD wavefuction probability density (Figure A.1).

Despite the wealth of obtainable functionality, the most utilized IR material set of lead chalcogenide QDs lacks options in shell growth. Importantly, the use of cation exchange was introduced as a route to PbS/CdS core/shell particles [3]. Here the anionic structure of a nanocrystal is maintained while the cations are exchanged. While this method allowed for significant improvements in air stability, the diversity of materials, thicknesses, and energy allignment types demonstrated with CdSe QDs is still inaccessible. This has often been attributed to the poor temperature stability of lead chalcogenide

particles and the absence of lattice-matched materials for epitaxial growth. Here, strategies to create novel core shell lead chalcogenide particles are explored; however, ulitmately, no means to achieve core/shell PbS was successful.

A.2 Cation exchange route to thick-shelled PbSe/PbS and PbSe/CdS QDs

Since its inception, the cation exchange approach to modifying QDs has greatly increased the versatility of synthetic routes [4]. Variations of this method have been used in situ to create monodispersed PbSe, post synthetically to obtain core/shell QDs, and as a means to obtain entirely new QDs. All of these materials have been inaccessible by traditional synthesis [3-7].

In its synthetic maturity, the CdSe/CdS system exhibits extremely high monodispersity and particle crystallinity and very thick shells are accessible. The goal of this work was to explore translating these attributes to the lead selenide system via cation exchange. Specifically, an initial complete cation exchange of high quality CdSe/CdS core/shell particles to PbSe/PbS would be followed by the optional partial cadmium cation exchange to create PbSe/CdS. The PbSe/CdS energy alignment would allow for a greater energetic barrier and the possibility of thick-shelled PbSe/CdS further enables applications in downshifting. Direct and intermediate-mediated cation exchange routes were explored.

A.2.1 Cation exchange via intermediate

Due to thermodynamic limitations, the low temperature cation exchange from cadmium chalcogenides to lead chalcogenides requires an intermediate transition, often through copper or silver [8]. A challenge of this technique, however, is the

residual intermediate impurities remain in the particles and act as unwanted quenching states [9, 10]. Methods to alleviate this problem included aging, which promotes self-exclusion, and the addition of phosphines, which more favorably bind to the impurities [10].

This technique was utilized to attempt to exchange CdSe/CdS to PbSe/PbS. The resulting emission is shown in figure A.2. While the initial CdSe/CdS emission showed a FWHM of 90 meV and a quantum yield above 85%, the resulting infrared emitting particles exhibited a broader FWHM of 120 meV and a QY of 8%. No visible emission was evident in the infrared particles, suggesting a complete transformation of CdSe/CdS. The moderate increase in the FWHM could be attributed to either a larger polydispersity or a broader PbSe/PbS homogenous linewidth compared to CdSe/CdS. The QY of the resulting particles is less than what is typically observed in the literature [11]. This is potentially a result of residual silver particles however the addition of tributylphosphine only provided a QY increase up to 10%. It is feasible that impurities remain, or that the crystallographic structure was negatively impacted during cation exchange resulting in non-radiative decay pathway formation. This route is potentially promising provide a non-parasitic intermediate can be utilized or a means to completely exclude the resulting dopants is found; however, for the purposes of this demonstration, it was not successful.

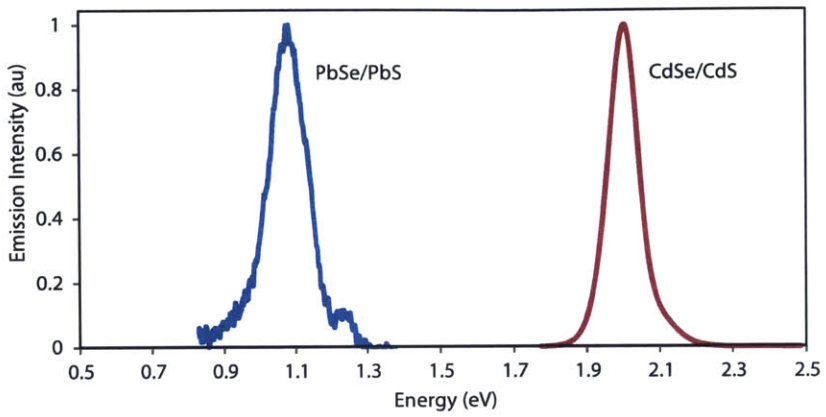

Figure A.2 The initial CdSe/CdS emission spectrum is compared to the resulting infrared emitting particles. An increase in the FWHM from 90 to 120 meV is observed. The resulting IR particles exhibited a relatively low 8% quantum yield, despite the initial QY above 85% for CdSe/CdS.

A.2.2 Direct cation exchange

A secondary means to create PbSe/PbS and PbSe/CdS particles via cation exchange utilized a direct exchange method published by Zhang *et al.* [12]. Here, a solution of lead chloride in oleylamine is heated to 80-190 °C at which point a solution of CdSe/CdS QDs in octadecene is rapidly injected. Performance of this cation exchange resulted in infrared emitting particles with QYs ranging from 30-40%. TEM micrographs are shown in figure A.3. The initial CdSe/CdS particles shown in (a) are angular in appearance however the resulting particles shown in (b) are highly spherical. This structural transition suggests instability in the anionic structure. To further explore this, the cation exchange reaction was performed on CdSe/CdS dot-in-rod nanoparticles. Here, although the rods are clearly visible in the initial TEM (c), they collapse into spheres during the

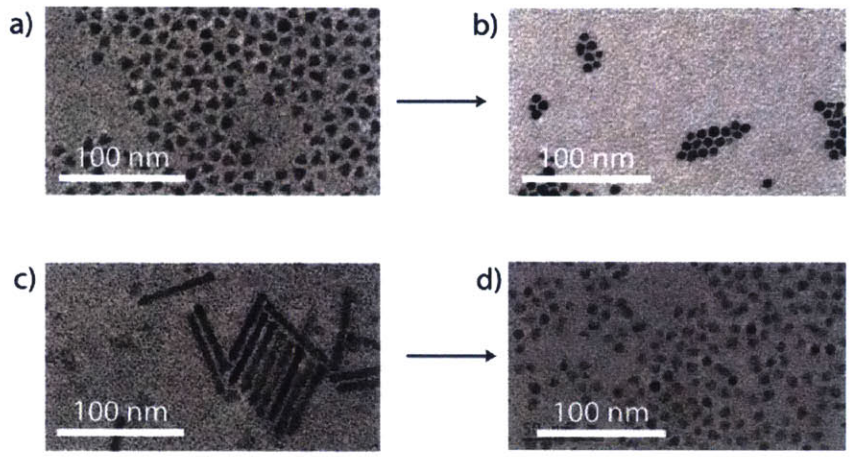

Figure A.3 The TEM of initial CdSe/CdS QDs (a) and dot-in-rod (c) are compared to their post-lead cation exchange counterparts. The original structure is not maintained during the cation exchange process.

.

cation exchange (d). Consequently, it is likely that a $PbSe_xS_{1-x}$ alloy rather than a discrete core-shell structure is being produced.

In an attempt to stabilize the anion structure during cation exchange, various concentrations of the anionic surfactants dodecyltrimethylammonium bromide, didodecyldimethylammonium bromide, and cetyl trimethylammonium bromide were explored, however their utilization failed to maintain the original shape [13]. As neither of these cation exchange routes allowed for the production of high quality PbSe/CdS, attention was turned toward epitaxial shell growth.

A.3 Exploration of epitaxial growth for shell growth

A.3.1 Challenge of PbS thermal stability

High quality shell growth often necessitates high temperature synthesis. Unfortunately, due to the lability of the lead-sulfur bond, an increase in temperature results in QD dissolution or Oswalt ripening. To evaluate the

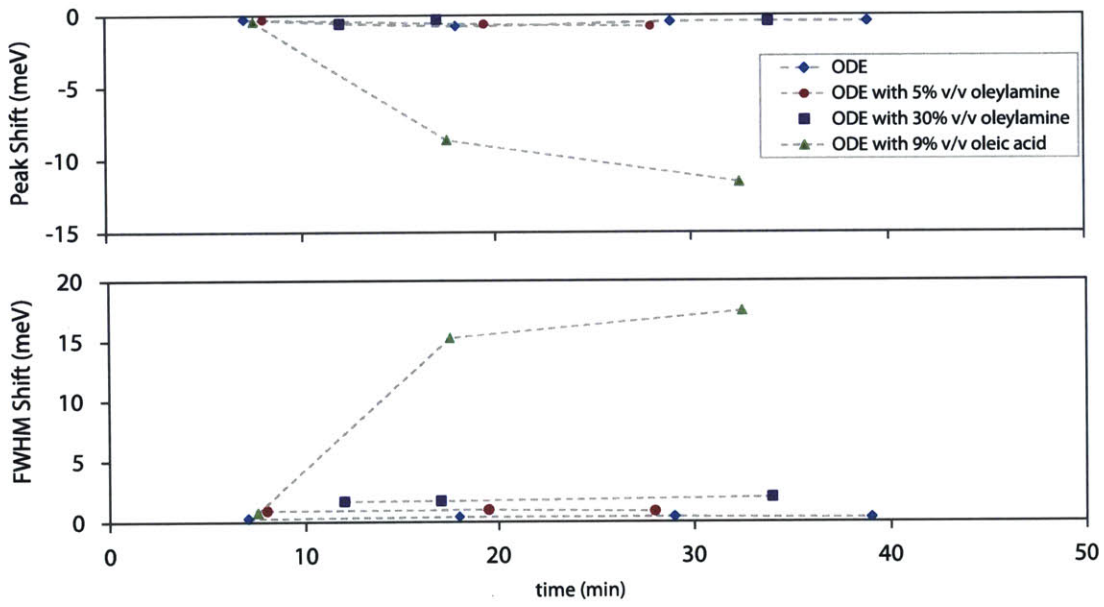

Figure A.4 PbS temperature stability was evaluated by monitoring emission peak position and FWHM at various temperatures over time. Shown here are example data taken at 100°C over the course of 40 min with various coordinating and non-coordinating solvent systems. While oleylamine and ODE solvent systems show little change, oleic acid facilitates ripening as indicated by the emission redshift and broadening.

thermal limits, a thermal stability study was performed on PbS. The sample emission was monitored for red-shifting and broadening as signs of particle ripening. Both the non-coordinating such of octadecene (ODE) and coordinating solvents of oleic acid (OA) and oleylamine (OlA) were explored in order to mimic shell growth conditions.

The solvent systems of pure ODE and ODE-OlA mixtures exhibited comparable thermal stability, showing signs of ripening at approximately 80-100 °C. In contrast, oleic acid promoted significant ripening, likely due to the strong Pb-OA bond facilitating atomic rearrangement (Figure A.4). From these data, it is apparent that synthetic attempts at epitaxial shell growth should not exceed 80-100 °C and oleic acid should be avoided or minimized.

A.3.2 Shell material considerations

In order to grow a high quality epitaxial shell, a well latticed-matched system is desired. Ideally a shell material with a similar crystallographic structure and lattice constant will be utilized to minimize strain. Multiple potential options were found for PbS by searching the International Crystallographic Database (ICSD). Of these options, tin sulfide was chosen as the most promising shell material to pursue due to lattice matching and availability of colloidally compatible precursors.

PbS QDs adopt a rock salt (*Fm-3m)* with a Pb-S distance of 2.96 Å. An ideal shell material would be well matched to these parameters. Tin sulfide frequently adopts a distorted rock salt (*Pnma*) structure with a Sn-S distance of 2.93 Å, and it has also been shown to adopt a rock salt structure under pressure, Sn-S distance=2.90 Å [14]. These values are particularly well matched, exhibiting

a less than 2% difference. For comparison, the high quality system of CdSe/CdS has a 3-4% difference in lattice constants.

In addition to demonstrating ideal lattice matching, SnS QDs (*Pnma*) have been produced, signifying the viability of colloidal tin and sulfur precursors. Finally, Soriano *et al.* demonstrated the production of a solid solution $Pb_xSn_{1-x}S$ particles, which not only showcases their material compatibility, but opens up possibilities for creating gradient shells, which have been predicted to decrease lattice strain and dislocations [15, 16].

Before proceeding with shell growth, it is important to consider the possible core-shell heterostructures. It is likely that the shell would likely adopt a *Pnma* or *Fm-3m* structure. Band gaps and work functions for *Pnma* SnS vary greatly in the literature, suggesting that either type-I or type-II structures are possible [17-19]. The *Fm-3m* SnS is far less studied, and neither the band gap nor work function has been published. In order to estimate the relative band gaps of *Fm-3m* SnS and *Fm-3m* PbS, the density of states were calculated with a tight binding LMTO program to determine the relative band gap of SnS and PbS in a rock salt structure (Figure A.5)[20, 21]. From these calculations, the band gap of bulk *Fm-3m* PbS was found to be 0.45 eV, in reasonable agreement with the literature value of 0.37 eV [19]. The *Fm-3m* SnS band gap was calculated as 0.15 eV. While no knowledge of the work function is obtained from these calculations, it can be expected that rock-salt SnS will have a smaller band gap than rock-salt PbS, allowing for the possibility of an inverted type-I or an type-II core/shell heterostructure.

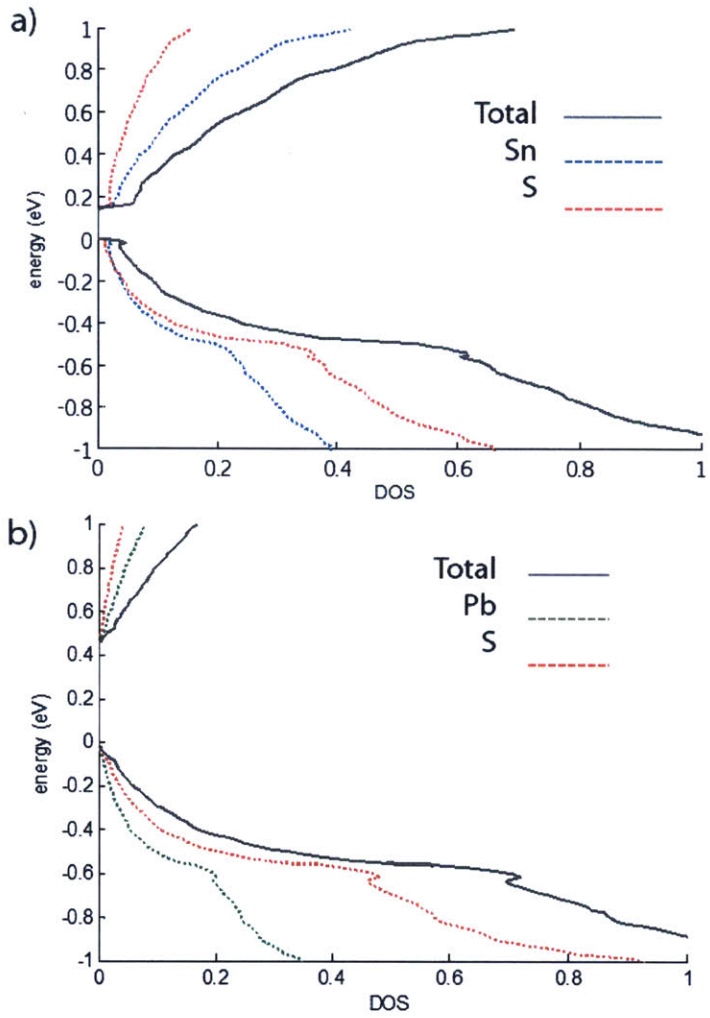

Figure A.5 TB-LMTO DOS calculations of SnS and PbS in the Fm-3m structure

A.3.3 Precursor considerations

The maximum temperature to prevent PbS ripening of 80-100 °C is significantly lower than the typical shell growth temperature of CdS on CdSe, which can typically range from 150-350 °C. To overcome the requirement of low temperature shell growth, high reactivity precursors can be utilized. One of the most reactive colloidal QD sulfur precursors is tris(trimethylsilyl)silane $(TMS)_2S$. This material is readily available, frequently used in PbS core synthesis, and has been utilized for room temperature QD synthesis [22].

Cation precursors are far more diverse. A variety of precursors, including tin chloride, tin acetylacetonate, tin oleate ($Sn(OA)_2$) and tin oxide were explored as possibilities. As a measure of their ability to react at the PbS thermal stability limit, equivalent quantities of the tin precursor and $(TMS)_2S$ were combined and heated to 80 °C while stirring. Of these options, $Sn(OA)_2$ allowed for nucleation.

The method used to prepare $Sn(OA)_2$ required a large excess of oleic acid to be added to SnO to facilitate a complete reaction. This excess oleic acid is difficult to remove and as was demonstrated in the thermal stability testing, is severely detrimental to particle stability. Consequently, prior to use in shell growth, tin myristate ($Sn(My)_2$) was synthesized by comparable means. Unlike the $Sn(OA)_2$ synthesis which results in a difficult-to-purify solution of $Sn(OA)_2$ in oleic acid, the synthesis of $Sn(My)_2$ results in a solid that can be purified via recrystallization with toluene.

A.3.4 Attempted shell growth

To attempt SnS shell growth, a sample of three-times purified PbS QDs was redispersed in previously degassed ODE at approximately 20 mM in a three-neck flask. The solution was heated to 80 °C under nitrogen at which point solutions of $Sn(My)_2$ in trioctylphosphine (TOP, 0.2 mM) and $(TMS)_2S$ in ODE (0.2 mM) were slowly introduced via syringe pump at a rate of 2.3 ml/min. Aliquots were taken at various time points and emission spectra measured.

Regardless of the heterostructure of the core/shell system, a red-shift is expected as a shell is grown. Figure A.6 shows the gradually shifting emission peak with added precursors compared to a control where only TOP and ODE were injected. During a shell growth, the emission FWHM can provide indirect evidence for the homogeneity of the shell growth. Here, small changes in the FWHM are observed with a slight narrowing followed by a slight broadening.

These data can be also result from coalescence of particles. To evaluate this, TEM were taken to ensure particles were still independent and no SnS seed particles were evident (Figure A.7). The particles appear stable at 60 min into the process, however aggregation is observed at 90 min. It is important to note that no growth is apparent from the TEM.

Additional controls were performed to evaluate the changes resulting from only tin or sulfur addition. The same quantity of tin, sulfur or both tin and sulfur were added to a reaction flask containing PbS via a syringe pump at 80 °C. Figure A.8 shows the resulting peak shift and quantum yield change of the

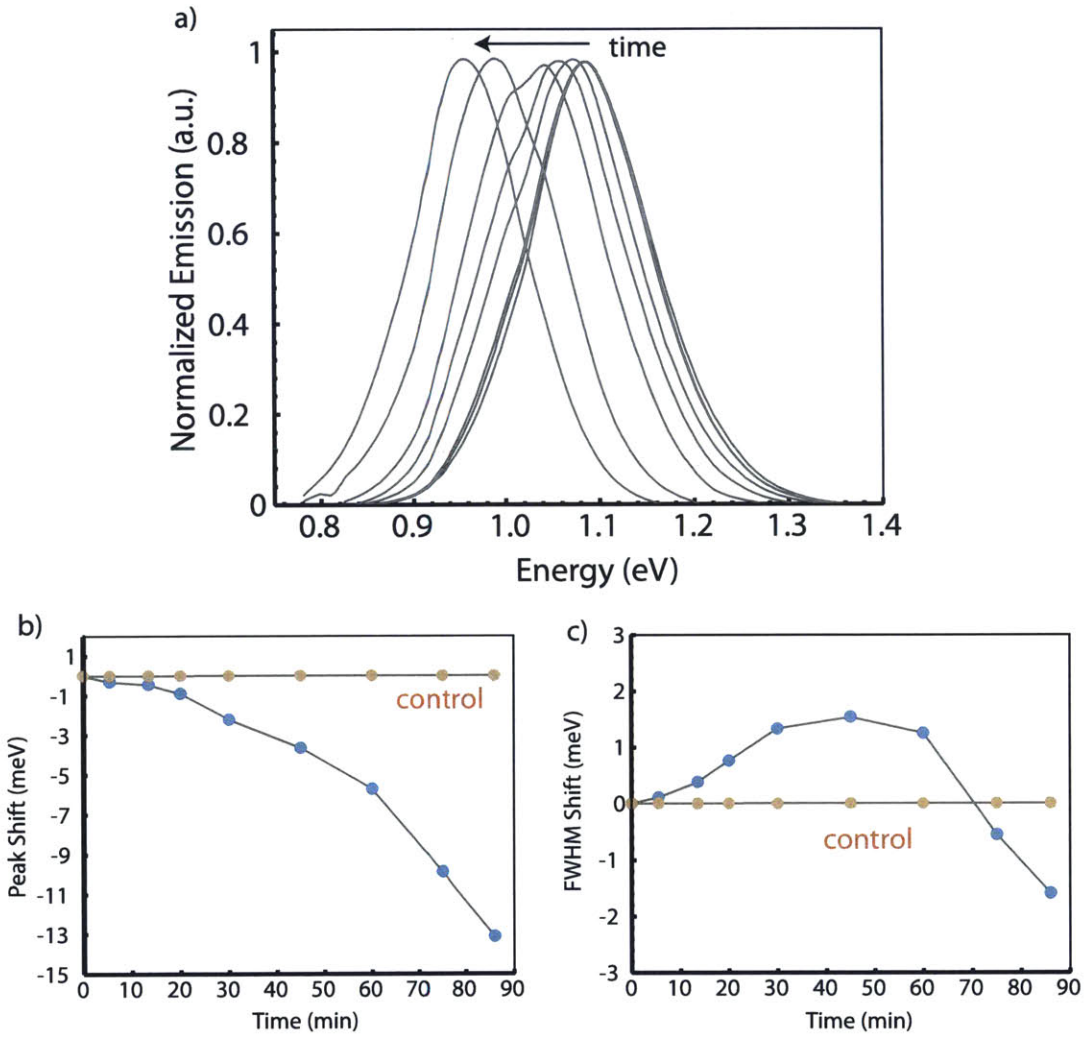

Figure A.6 a) Resulting spectra from attempted SnS shell growth on PbS. The emission designated by blue markers exhibits a redshift (b) and changes in its emission FWHM that are not exhibited by the control shown in orange. The control entailed a slow addition of solvents only at the temperature of synthesis.

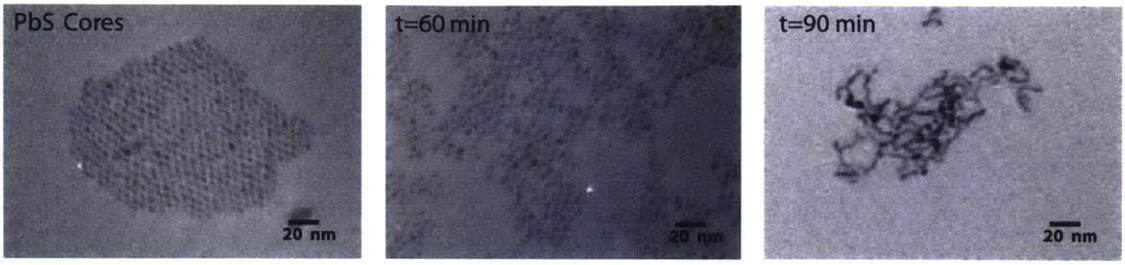

Figure A.7 TEM of various aliquots taken during attempted shell growth. The particles remain discrete and no signs of SnS nuclei are evident at 60 min, however aggregation is apparent at 90 min.

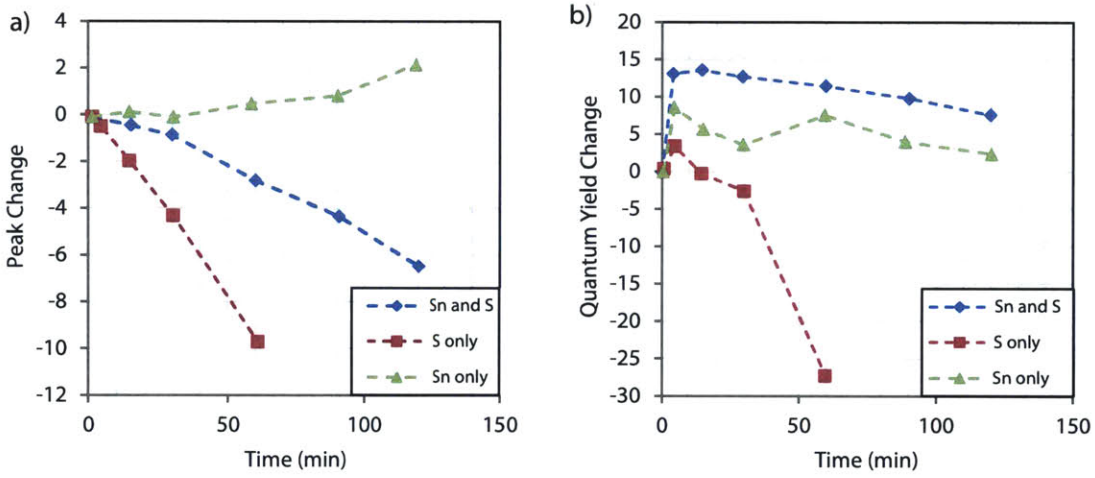

Figure A.8 Individual addition of sulfur or tin controls. The peak change (a) and change in QY (b) are shown as a 0.2 mM solution of tin, sulfur, or both is introduced to a solution of PbS QDs under the same synthetic conditions.

PbS QDs as sulfur, tin, or both were introduced to the synthesis. While the additional sulfur results in large red-shift, the introduction of tin results in a blue-shift. The red-shift has been attributed in the literature to unpassivated sulfur and it is possible that the blue-shift is a result of lead-tin cation exchange. Further, the quantum yield dramatically decreases with the addition of sulfur; however, a slight increase is observed with only the addition of tin and the largest increase is seen with the addition of both.

This process was repeated for various core sizes and the emission, Stokes shift, QY and PL are reported in figure A.9. In each subplot, the native-PbS properties are designated by a black "x" and a series of different temporal aliquots originating from the same core size are shown in the same color. Dashed black lines provide a guide for the eye of native-PbS particle properties. For all samples explored, the emission shifts toward lower energies as the synthesis progresses. While both emission and absorption features shift, the first absorbance feature shifts to a lesser degree than what is observed in core-only particles (Figure A.8a). Consequently, although the Stokes shift of native-PbS particles tends to decrease at shorter energies, the Stokes shift observed in a synthetic series is relatively flat (Figure A.9b). Additionally, all samples exhibit an increase in FWHM throughout the synthesis (Figure A.9 c). The QY displays interesting trends. For most series, the QY monotonically decreases as more precursors are added. However for the smallest band gap particles, the QY exhibits an initial increase followed by a decrease (Figure A.9 d).

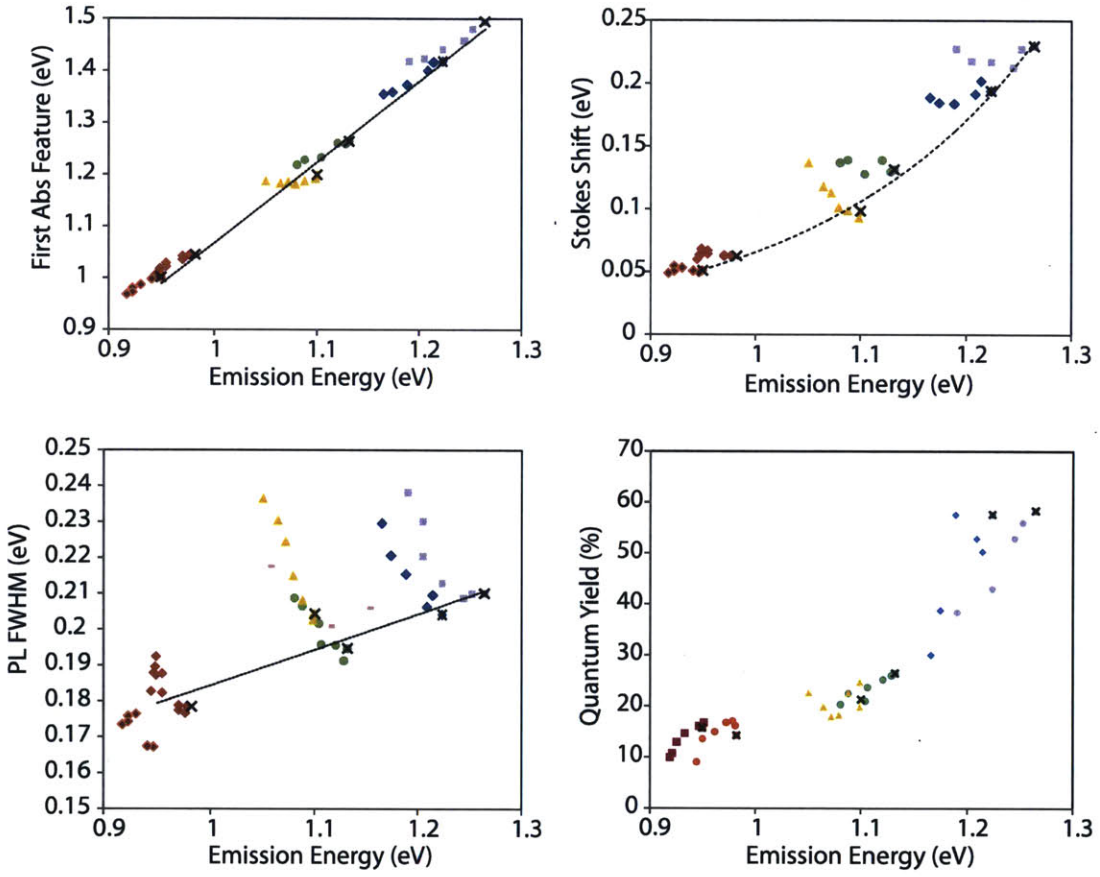

Figure A.9 Various optical properties of PbS particles as additional tin and sulfur is added. Native-PbS properties are represented by a black "x" and black dotted lines provide a guide for the eye of native-PbS properties. Sequential aliquots taken from a synthetic series are shown in the same color.

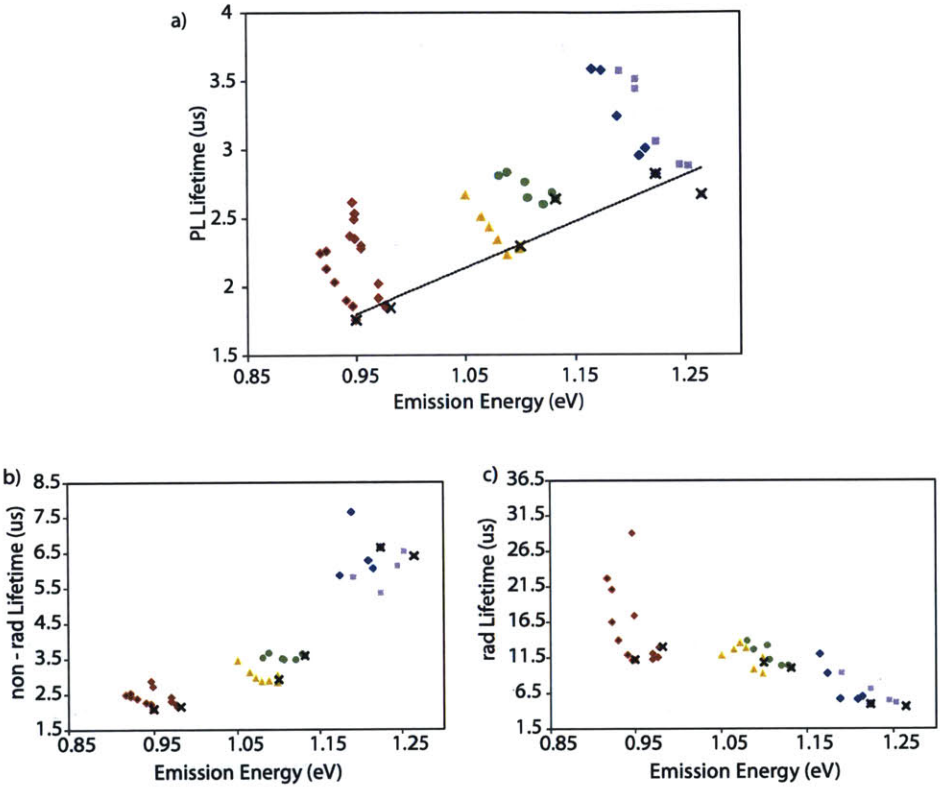

Figure A.10 a) The measured PL lifetime for various native-PbS (black x) and aliquots in various synthetic series (series are shown in the same color). The black line is a guide for the eye. Estimated non-radiative and radiative lifetimes are shown in b) and c)

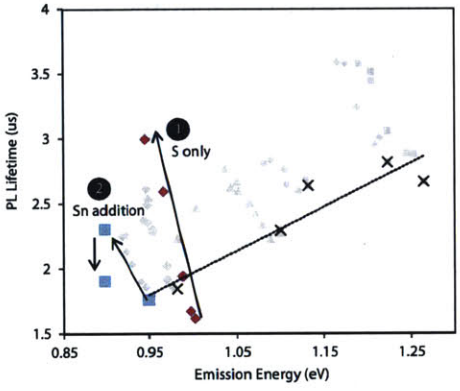

Figure A.11 PL lifetime controls by addition of only sulfur (1) or excess tin post synthetically (2)

The PL lifetimes were measured for these series and are shown in figure A.10. Using the measured QY and lifetime, the radiative and non-radiative contributions were estimated and shown in figure A.10b and c using the expressions derived in equations A.1-5 and assuming a single non-radiative rate.

$$QY = \frac{k_r}{k_{PL}} = \frac{k_r}{k_r + \sum k_{nr}} \tag{A.1}$$

$$k_r = QY \times k_{PL} \tag{A.2}$$

$$\tau_r = \frac{\tau_{PL}}{QY} \tag{A.3}$$

$$k_{nr} = k_{PL} - k_r = k_{PL} - QY \times k_{PL} \tag{A.4}$$

$$\tau_{nr} = \tau_{PL} - \frac{\tau_{PL}}{QY} \tag{A.5}$$

A monotonic increase in the measured lifetime is observed for all series. Although both exhibit an increase with increased precursor injection, the radiative lifetime appears to increase at a faster rate than the non-radiative lifetime. Controls were performed and shown in figure A.11 and compared to the figure A.10 data which has been greyed out for clarity. Although the lifetime was not impacted by the sole addition of tin (data not shown) the lifetime increased with the sole addition of sulfur, shown in red and designated with the number 1. This may indicate that the lifetime increase is primarily due to an increase in sulfur even when both precursors are added. As a means to interrogate the role of stoichiometry this further, additional $Sn(My)_2$ was added to the final aliquot of one synthetic series, which resulted in a significant reduction in the PL lifetime, almost to its original value. These results are consistent a stoichiometry impact rather than a shell effect, however further investigation of these effects is necessary.

Using bottom gate FETs with gold interdigitated electrodes, the mobilities of various aliquots were measured. Figure A.12 shows the change in electron (μ_e) and hole (μ_h) mobilities as various quantities of precursor were added. Initial core values are shown as an "x" for each series. Although the electron mobility decreases by up to an order of magnitude, an increase of comparable degree is observed in the hole mobility. In general, both of these quantities increase with increasing core size which has been attributed to a reduced number of required hopping events; however, this does not appear to account for the increase in hole mobility as the size increase in these particles is small and too insignificant to confidently measure via TEM. Controls of tin or sulfur addition only were explored (Figure A.13). Results show that while the addition of sulfur appears to increase both the hole and electron mobility, additional tin results in a reduction in electron mobility and a minor change in hole mobility. Consequently, one dominating surface ion cannot fully explain the observed results obtained.

In summary, through addition of tin and sulfur precursors numerous effects are observed which include a red-shift in emission, decrease of QY, increase in radiative lifetime, increase in hole mobility with a decrease in electron mobility. All of the changes observed in optical properties shown here can be described by a type-II heterojunction, however the following sections will discuss why this is not likely the case. In a type-II heterojunction, one carrier is more localized in the shell and the other is localized in the core. This could result in emission from the shell to the core, manifesting itself as a emission red-shift. The wavefunction overlap between the shell localized carrier and surface states is

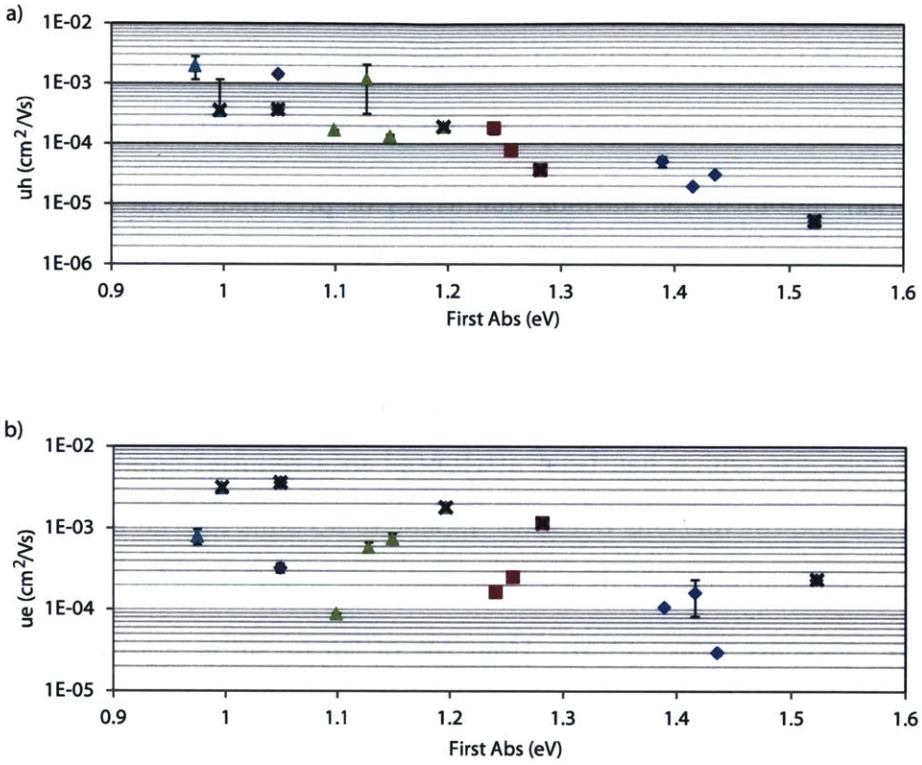

Figure A.12 Hole and electron mobilities for various series where tin and sulfur were added to PbS core particles. Error bars show the standard deviation of multiple measurements

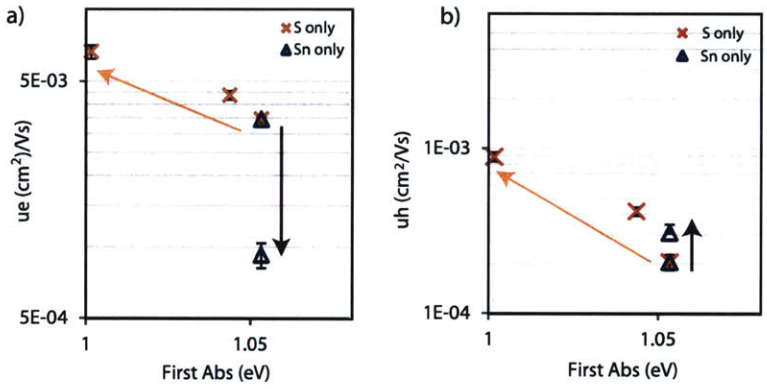

Figure A.13 Control of change in electron and hole mobility with sole addition of tin or sulfur. Error bars show the standard deviation of multiple measurements.

increased, which can result in increased non-radiative decay and a reduction of QY. Finally, it is feasible that when considering the mobility of type-II heterostructure particles, the shell-localized carrier would increase mobility while the core-localized carrier would decrease. Although this line of rational appears to support the results, further experiments indicate that it is unlikely that a SnS shell has been grown on the QDs. Instead it is probable that the modified stoichiometry accounts for many of the observed properties.

A.3.5 Impact of stoichiometry

From the controls explored in this work, it is impossible to exclude the potential impact of stoichiometry on the resulting photophysical effects. Particularly, the emission red-shift, lengthening of the PL lifetime and increase in hole mobility can all potentially result from an increase in sulfur according to the controls. However, not all effects were replicatable by the sole addition of sulfur. This could be a result of some cationic passivation from the concurrent tin addition or it could be a result of electronic changes resulting from both of these species growing on the surface of the QDs.

A similar effect in QY and the PL lifetime was obtained in a study of the stoichiometry variation of cadmium telluride QDs [23]. Here they also observed a decrease in QY with increasing anion content, a drastic increase in the radiative lifetime, and a smaller decrease in the nonradioactive lifetime. They attribute this lifetime change with increasing anion content to an increase in the number of telluride band edge states which open up a new pathway for both radiative and non-radiative recombination.

This theory could also be used to explain the optical changes observed. The emissive red-shift could occur due to an increased population of optically active sulfur states. The absorbance could remain fairly constant as band to band absorption may still be occurring. These two occurrences would results in the Stokes shift trends observed. The addition of excess sulfur states would have less predictable effects on the mobilities, however a recent report has illustrated the potential for charge conduction through defect states in PbS [24].

A.4 Conclusions and future scope

The results of these studies suggest that the optical properties are tunable by post synthetically modifying the surface atoms. As these effects are also dependent on the particle's stoichiometry, it may be possible to use simple spectroscopic measurements to estimate the cation:anion ratio of a QD sample. These effects have important implications in many QD applications that utilize the emission or conductive properties of QDs, however without further efforts; it is not possible to definitively discern their origin.

A.5 Experimental details

A.5.1 Synthesis

All controls and syntheses were performed under similar conditions. A stir-bar and septum-equipped round bottom flask was evacuated on a schlenk line and previously degassed and prepared PbS QDs dispersed in octadecene (20 ml, 0.73 mM) was transferred out of a glovebox in a syringe and added to the flask under nitrogen. The reaction vessel was heated to 80 °C and 0.2 mM solution of $(TMS)_2S$ in trioctylphosphine oxide and $Sn(My)_2$ in octadecene injected at a rate

of 2.3 ml/min. Aliquots were taken with a glass syringe and transferred to an nitrogen-flushed septum capped vial or the resulting material was cannula transferred to a evacuated flask to be transferred and processed inside a glovebox. The particles are crashed with acetone or isopropanol.

A.5.2 Materials characterization

Absorption measurements were performed using a Cary 5000, emission spectra were measured with a home-built spectrometer equipped with a Roper Instruments InGaAs array detector and an 532 nm diode excitation source. Quantum yield measurements were performed using an integrating sphere which has been detailed in section 2.9.1. Photoluminescent lifetime measurements were taken with a 532 nm 5 ns Nd:YAG laser excitation and measured with a biased 10 ns InGaAs detector.

A.5 Chapter specific acknowledgements

Useful conversations were held with Ou Chen and Dan Harris. Ou Chen and Igor Coropceanu provided CdSe/CdS material.

A.4.8 References

[1] M. A. Boles, D. Ling, T. Hyeon and D. V. Talapin. "The surface science of nanocrystals." *Nat Mater*, **15**, 141 (2016).

[2] P. Reiss, M. Protière and L. Li. "Core/Shell Semiconductor Nanocrystals." *Small*, **5**, 154 (2009).

[3] J. M. Pietryga, D. J. Werder, D. J. Williams, J. L. Casson, R. D. Schaller, V. I. Klimov and J. A. Hollingsworth. "Utilizing the Lability of Lead Selenide to Produce Heterostructured Nanocrystals with Bright, Stable

Infrared Emission." *Journal of the American Chemical Society*, **130**, 4879 (2008).

[4] B. J. Beberwyck, Y. Surendranath and A. P. Alivisatos. "Cation Exchange: A Versatile Tool for Nanomaterials Synthesis." *The Journal of Physical Chemistry C*, **117**, 19759 (2013).

[5] M. V. Kovalenko, D. V. Talapin, M. A. Loi, F. Cordella, G. Hesser, M. I. Bodnarchuk and W. Heiss. "Quasi-Seeded Growth of Ligand-Tailored PbSe Nanocrystals through Cation-Exchange-Mediated Nucleation." *Angewandte Chemie International Edition*, **47**, 3029 (2008).

[6] B. J. Beberwyck and A. P. Alivisatos. "Ion Exchange Synthesis of III–V Nanocrystals." *Journal of the American Chemical Society*, **134**, 19977 (2012).

[7] H. Li, R. Brescia, R. Krahne, G. Bertoni, M. J. P. Alcocer, C. D'Andrea, F. Scotognella, F. Tassone, M. Zanella, M. De Giorgi and L. Manna. "Blue-UV-Emitting ZnSe(Dot)/ZnS(Rod) Core/Shell Nanocrystals Prepared from CdSe/CdS Nanocrystals by Sequential Cation Exchange." *ACS Nano*, **6**, 1637 (2012).

[8] D. H. Son, S. M. Hughes, Y. Yin and A. Paul Alivisatos. "Cation Exchange Reactions in Ionic Nanocrystals." *Science*, **306**, 1009 (2004).

[9] A. Sahu, M. S. Kang, A. Kompch, C. Notthoff, A. W. Wills, D. Deng, M. Winterer, C. D. Frisbie and D. J. Norris. "Electronic Impurity Doping in CdSe Nanocrystals." *Nano Letters*, **12**, 2587 (2012).

[10] P. K. Jain, B. J. Beberwyck, L.-K. Fong, M. J. Polking and A. P. Alivisatos. "Highly Luminescent Nanocrystals From Removal of Impurity Atoms Residual From Ion-Exchange Synthesis." *Angewandte Chemie International Edition*, **51**, 2387 (2012).

[11] O. E. Semonin, J. C. Johnson, J. M. Luther, A. G. Midgett, A. J. Nozik and M. C. Beard. "Absolute Photoluminescence Quantum Yields of IR-26 Dye, PbS, and PbSe Quantum Dots." *The Journal of Physical Chemistry Letters*, **1**, 2445 (2010).

[12] J. Zhang, J. Gao, C. P. Church, E. M. Miller, J. M. Luther, V. I. Klimov and M. C. Beard. "PbSe Quantum Dot Solar Cells with More than 6%

Efficiency Fabricated in Ambient Atmosphere." *Nano Letters*, **14**, 6010 (2014).

[13] S. Ithurria and D. V. Talapin. "Colloidal Atomic Layer Deposition (c-ALD) using Self-Limiting Reactions at Nanocrystal Surface Coupled to Phase Transfer between Polar and Nonpolar Media." *Journal of the American Chemical Society*, **134**, 18585 (2012).

[14] A. Mariano and K. Chopra. "Polymorphism in some IV-VI compounds induced by high pressure and thin-film epitaxial growth." *Applied Physics Letters*, **10**, 282 (1967).

[15] R. B. Soriano, C. D. Malliakas, J. Wu and M. G. Kanatzidis. "Cubic Form of Pb2–xSnxS2 Stabilized through Size Reduction to the Nanoscale." *Journal of the American Chemical Society*, **134**, 3228 (2012).

[16] J. Lim, W. K. Bae, D. Lee, M. K. Nam, J. Jung, C. Lee, K. Char and S. Lee. "InP@ZnSeS, Core@Composition Gradient Shell Quantum Dots with Enhanced Stability." *Chemistry of Materials*, **23**, 4459 (2011).

[17] L. A. Burton and A. Walsh. "Band alignment in SnS thin-film solar cells: Possible origin of the low conversion efficiency." *Applied Physics Letters*, **102**, 132111 (2013).

[18] N. Koteeswara Reddy, M. Devika and E. S. R. Gopal. "Review on Tin (II) Sulfide (SnS) Material: Synthesis, Properties, and Applications." *Critical Reviews in Solid State and Materials Sciences*, **40**, 359 (2015).

[19] O. Madelung. "IVx-VIy compounds." *in* Semiconductors: Data Handbook. edited by (Springer Berlin Heidelberg 2004).

[20] O. K. Andersen. "Linear methods in band theory." *Physical Review B*, **12**, 3060 (1975).

[21] T.-Y. Liu, M. Li, J. Ouyang, M. B. Zaman, R. Wang, X. Wu, C.-S. Yeh, Q. Lin, B. Yang and K. Yu. "Non-Injection and Low-Temperature Approach to Colloidal Photoluminescent PbS Nanocrystals with Narrow Bandwidth." *The Journal of Physical Chemistry C*, **113**, 2301 (2009).

[22] B. Omogo, J. F. Aldana and C. D. Heyes. "Radiative and Non-Radiative Lifetime Engineering of Quantum Dots in Multiple Solvents by Surface

Atom Stoichiometry and Ligands." *The journal of physical chemistry. C, Nanomaterials and interfaces*, **117**, 2317 (2013).

[23] Y. Zhang, D. Zherebetskyy, N. D. Bronstein, S. Barja, L. Lichtenstein, D. Schuppisser, L.-W. Wang, A. P. Alivisatos and M. Salmeron. "Charge Percolation Pathways Guided by Defects in Quantum Dot Solids." *Nano Letters*, **15**, 3249 (2015).